Catalyst-assisted and catalyst-free growth of III-V semiconductor nanowires

PhD thesis

Umesh Prasad Gomes

Scuola Normale Superiore

National Enterprise for Nanoscience and Nanotechnology

Supervisor

Prof. Lucia Sorba

ACKNOWLEDGEMENTS

First, I would like to express my gratitude to Prof. Lucia Sorba and Prof. Fabio Beltram for the opportunity and the confidence that they provided me to pursue my Ph.D at NEST, Scuola Normale Superiore. I would like to thank Prof. Lucia Sorba for her valuable suggestions and guidance throughout my Ph.D tenure at NEST.

I would like to express my thanks to Dr. Daniele Ercolani for providing me both scientific and technical training in nanowire growth and characterization. His creative ideas have helped me tremendously to design well-planned experiments, analyse the data accordingly and write articles in a clear and concise way that completely changed and increased the impact of the publication.

I would also like to thank Dr. Valentina Zannier, Dr. Sergio Battiato and Dr. Elena Husanu who have helped me continuously with my experiments and there was always something new to learn from them.

Thanks to our collaborators Prof. Vladimir G. Dubrovskii and Dr. Nickolai V. Sibirev for the fruitful discussions on the modelling of the nanowire growth.

Thanks to Dr Jeremy David, Dr Mauro Gemmi, Dr. E. Ubyivovk, and Dr. Francesca Rossi for the wonderful TEM images and analysis of our nanowires.

I would also like to thank Dr. Stefan Heun, Yuya Murata and Abhishek Kumar for their help in sputtering and Auger electron spectroscopy experiments.

Thanks to all my friends at Scuola Normale Superiore for their continuous support throughout my stay at Pisa. I will always remember the times we shared in the SNS Mensa, table tennis and hiking events.

Finally, I would like to express gratitude to my wife who has always supported me and helped me in the most difficult periods.

ABSTRACT

The aim of this thesis is to understand the dynamics of the nucleation and growth of III-V semiconductor nanowires and associated heterostructures grown by chemical beam epitaxy. These nanowires represent well-controlled and high quality materials suitable for both fundamental physics and applications in optical and electronic devices.

The first part of the thesis investigates growth recipes to obtain Au-catalyzed InAs NWs with controlled morphology. Good control of NW length and diameter distributions has been achieved by a systematic study of two different Au deposition techniques: Au thin film deposition and colloidal dispersion.

Triggered by the issues of Au contamination and CMOS compatibility, the second part of the thesis is dedicated to the investigation of the nucleation and growth mechanisms of Au-free InAs NWs on Si (111) substrates. A thorough analysis of the silicon substrate preparation is conducted and an optimized silicon surface for the nucleation of Au-free nanowires is identified. We show that the silicon surface can be modified by *in situ* and *ex situ* parameters allowing us to control the density of NWs. Growth conditions were established for growing InAs NWs either by catalyst-free or self-catalyzed mechanisms on Si (111). The catalyst-free growth proceeds in the vapor-solid growth mechanism without the use of any catalyst particle while the self-catalyzed growth proceeds in the vapor-liquid-solid mechanism involving a liquid In droplet. Growth models are proposed in order to interpret the experimental findings.

The third part of the thesis concerns the growth of axial and radial (core-shell) heterostructured NWs. Nanowire heterostructures combining either highly lattice mismatched materials (GaAs and InAs) or almost lattice matched materials (InAs and GaSb) are investigated. GaAs/InAs and InAs/GaAs axial heterostructures are grown by Au-catalyzed method. Here, it is demonstrated that the catalyst composition, rather than other growth parameters, as postulated so far, controls the growth mode and the resulting NW morphology. We have also explored the growth of core-shell InAs/GaSb heterostructures by catalyst-free mechanism. The morphology and structural properties of InAs/GaSb core-shell heterostructures are optimized to fabricate Esaki tunnel diodes exploiting their broken-gap band alignment.

CONTENTS

Acknowledgements 1
Abstract 2
Contents 3
Acronyms 6
Introduction 7
1 Nanowire Growth Mechanisms 10

1.1 Au-catalyzed vapour-liquid-solid growth mechanism 10
1.2 Au-free growth mechanisms 14

1.2.1 Catalyst-free NW growth mechanism 14
1.2.2 Self-catalyzed (SC) growth mechanism 17

1.3 III-V and silicon integration 18

2 Experimental Techniques 21

2.1 Chemical beam epitaxy 21

2.1.1 Vacuum chambers and pump systems 22
2.1.2 Gas handling system and injectors 23

2.2 Au-catalyst preparation 24
2.3 Silicon substrate preparation 25
2.4 Electron microscopy 28
2.5 Statistical analysis 29

2.5.1 Software overview 29
2.5.2 NW diameter measurement 31
2.5.3 NW length measurement 32

3 Au-catalyzed InAs NWs 34

3.1 Growth protocol of Au-catalyzed InAs NWs 34
3.2 Diameter distribution and density of Au-catalyzed InAs NWs 35

3.2.1 Au film thickness dependence 36
3.2.2 Annealing temperature dependence 37
3.2.3 Annealing time dependence 38
3.2.4 Au colloidal dependence 40
3.2.5 Comparison of diameter distribution and density between the two NP preparation methods 42

3.3 Length distribution of Au-catalyzed InAs NWs *44*

3.3.1 Experimental results 44
3.3.2 Rate equation model 48
3.3.3 Modelling results and discussion 52
3.3.4 Comparison of LDs between the two NP preparation methods 53

3.4 Chapter summary *54*

4 Catalyst-free InAs NWs 55

4.1 CF InAs NW growth *55*

4.1.1 Two-stage NW growth protocol 55
4.1.2 Length-radius dependence 59
4.1.3 Influence of MO precursors 62
4.1.4 Influence of growth temperature 64
4.1.5 Aspect ratio control 65
4.1.6 Crystal structure 66

4.2 Density and yield control of CF InAs NWs *67*

4.2.1 NW growth process 67
4.2.2 Dependence of *N* and *Y* on annealing conditions 69
4.2.3 Dependence of *N* and *Y* on growth temperature 71
4.2.4 Dependence of *N* and *Y* on sputtering parameters 73
4.2.5 Dependence of *N* on growth time 75

4.3 Chapter summary *76*

5 Self-catalyzed InAs NWs 77

5.1 Nucleation and growth mechanism *77*
5.2 Length-radius dependence *79*
5.3 SC NW growth model *81*
5.4 Modelling results and discussion *84*
5.5 Influence of MO precursors *85*
5.6 Influence of growth temperature *88*
5.7 Influence of predeposited In droplets *89*
5.8 SC InAs NW length distribution (LD) *91*
5.9 Crystal structure *93*
5.10 Comparison between CF and SC NW growth mechanisms *94*

5.10.1 Requirement of different growth parameters 94

5.10.2 Different growth rates for CF and SC NWs 94

5.11 Chapter summary *95*

6 InAs-GaAs NW heterostructures 96

6.1 GaAs/InAs heterostructured NWs *96*
6.2 InAs/GaAs/InAs double-heterostructured NWs *101*
6.3 InAs/GaAs heterostructured NWs *103*
6.4 Comparison of growth modes *106*
6.5 Chapter summary *110*

7 InAs/GaSb NW heterostructures 111

7.1 InAs/GaSb heterostructured NW growth protocol *111*
7.2 Influence of different precursors on GaSb shell growth *112*
7.3 Influence of growth time on GaSb shell growth *114*
7.4 Compositional and structural characterization *115*
7.5 Performance of InAs/GaSb Esaki diode *117*
7.6 Chapter summary *119*

8 Conclusions and perspectives 121
9 Bibliography 124
List of publications 140

ACRONYMS

CBE Chemical Beam Epitaxy

CF Catalyst-free

EBL Electron Beam Lithography

EDX Energy dispersive X-ray

MBE Molecular Beam Epitaxy

MOVPE Metalorganic Vapour Phase Epitaxy

MO Metalorganic

NP Nanoparticle

NW Nanowire

SC Self-catalyzed

SEM Scanning Electron Microscope

TBAs Tertiarybutylarsine

TBP Tertiarybutylphosphine

TDMASb Tert-dimethylaminoantimony

TEGa Triethylgallium

TEM Transmission Electron Microscopy

TMIn Trimethylindium

TMSb Trimethylantimony

VLS Vapor-Liquid-Solid

WZ Wurtzite

ZB Zinc Blende

INTRODUCTION

Gordon Moore, one of the founders of Intel, observed in an article in the April 19, 1965 issue of Electronics Magazine that the number of components in an integrated circuit (IC) had doubled every year from the invention of the IC and predicted that this trend would continue for at least ten years [1]. Moore adjusted the rate to every two years in 1975 and accordingly the most popular formulation is of the doubling of the number of transistors on ICs every two years. The implications of this law were the reduction of the relative manufacturing cost and increased computing speed that has driven the semiconductor industry till date. It has been speculated that Moore's trend cannot continue indefinitely due to the physical limit of down scaling the dimension of transistors. Therefore in order to keep the Moore's trend on the roadmap, new device architectures and materials are being exploited which are usually termed as the Emerging Research Devices (ERD) and Emerging Research materials (ERM) according to the ITRS (International Technology Roadmap for Semiconductors). Amongst several of the ERMs, one-dimensional (1D) compound semiconductor nanowires (NWs) have shown to be potential candidates while nanowire field-effect transistor (FET), which is also known as a "gate-all-around" transistor, is a potential ERD. Figure 1.1 shows the CMOS technology nodes and the predicted end of CMOS downscaling with possible alternatives (nanotubes and nanowires) for post-2015 nanotechnology.

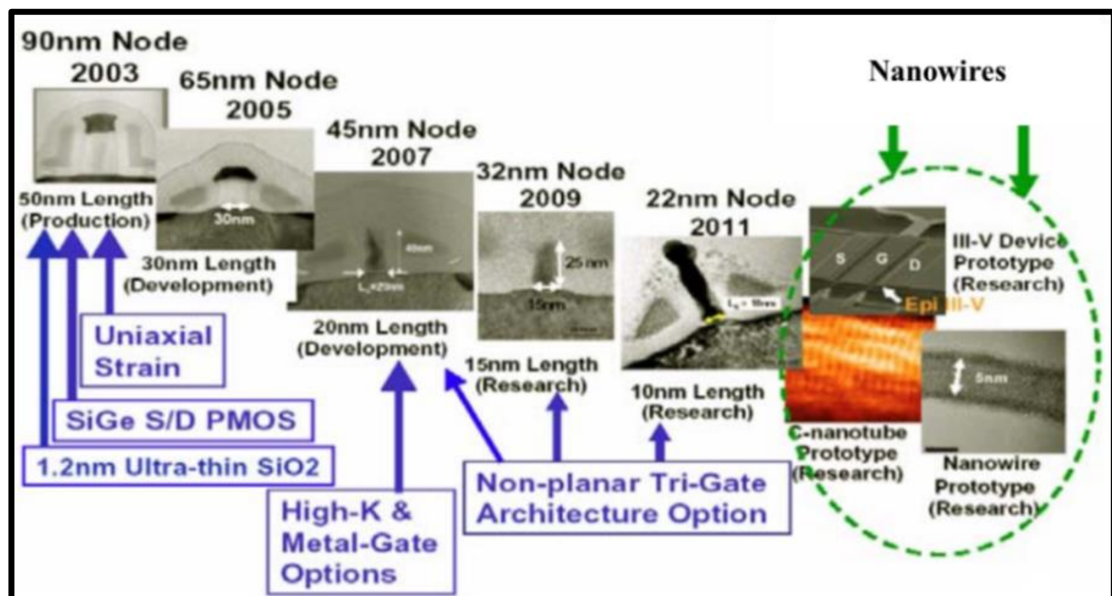

Figure 1.1. CMOS technology nodes and predicted end of CMOS down-scaling with possible alternatives (nanotubes and nanowires) for post-2015 nanotechnology (Source: R. Chau, Intel, presentation at ICSICT, 2004)

Semiconductor nanowires (NWs) are crystals with an extremely high aspect ratio with a diameter typically smaller than 100 nm and length of several microns that can be created in a bottom-up and top-down approach. The growth of NWs was first described by Wagner and Ellis by a 1D bottom-up growth mechanism termed as vapour-liquid-solid mechanism (VLS) [2]. From then onwards, NWs have been intensively studied and various other growth mechanisms have also been identified. Figure 1.2 shows a typical SEM micrograph of Au catalyzed InAs NWs grown by VLS mechanism by chemical beam epitaxy (CBE) technique.

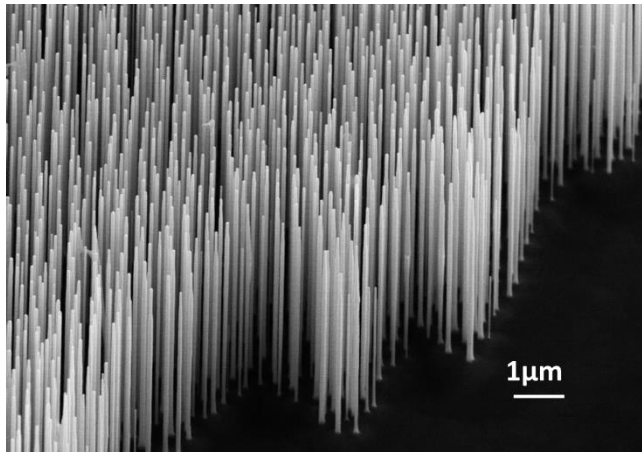

Figure 1.2. Au-catalyzed InAs nanowires grown by VLS chemical beam epitaxy technique

One of the primary reasons for the interest in NWs as an ERM is the flexibility in manipulating the electronic and optical properties by changing the NW composition and diameter. Changing the NW diameter can be accompanied by a change in crystal structure [3,4]. In this way, it is possible to modulate energy gap, carrier confinement and mobility which are important parameters for electronic and optical properties [5–7]. Another important advantage of the NW geometry is the ability to form heterostructures with sharp interfaces. The morphology of NWs makes it possible to grow heterostructures with different material combination without defect formation for lattice mismatch much larger than can be accommodated in bulk systems, thanks to the lateral strain relaxation. The advantages of combining materials and the ability to manipulate different properties have led to the realization of various applications. These are not limited to FETs [8–12] but extend over several applications in various fileds like plasma-wave THz detectors [13], light emitting diodes (LEDs) [14], lasers [15], solar cells [16] and quantum devices like single electron transistors [17] and nano-scale spin rectifiers [18].

Both for applications and fundamental studies it is highly desirable to manipulate the

morphological, structural and compositional features of NWs which requires appropriate choice of growth procedures. In order to do so in a rational way, an in-depth understanding of the mechanisms that govern NW nucleation and growth is indispensable. In this thesis, we will address NW nucleation and growth mechanisms of Au-catalyzed, self-catalyzed and catalyst-free III-V NWs. These mechanisms are probed in details using several experimental techniques, statistical data analysis and theoretical modelling. Based on the understanding of the nucleation and the growth mechanisms we were able to grow InAs NWs and associated axial and radial heterostructures proposed for various device applications.

The thesis is outlined as follows:

Chapter 1: This chapter reviews the different bottom-up growth mechanisms of NWs relevant to the thesis.

Chapter 2: The growth chamber, sample preparation and the characterization techniques used for the experiments within this thesis are introduced in this chapter. This chapter also provides details of in-house developed image analysis software for statistical analysis of the grown samples.

Chapter 3: This chapter investigates the correlation between Au-catalyst preparation and InAs NW diameter and length distributions.

Chapter 4. The objective of this chapter is to explore the catalyst-free InAs NW growth mechanism on silicon substrate. Furthermore, this chapter discusses about the strategies to control the density and yield of catalyst-free InAs NWs.

Chapter 5. The objective of this chapter is to explore the self-catalyzed InAs NW growth mechanism on silicon substrate.

Chapter 6. In this chapter, the successful growth of InAs/GaAs, InAs/GaAs/InAs, and GaAs/InAs axial heterostructured NWs is demonstrated. A careful investigation of the NW morphology as a function of the growth parameters and of the catalyst nanoparticle chemical composition has been performed by means of SEM, TEM and EDX.

Chapter 7. Experimental results on the growth of catalyst-free InAs/GaSb core-shell NWs are shown. Esaki tunnel devices are fabricated and negative differential resistance is demonstrated in core-shell device configuration.

Chapter 8.This chapter provides a summary of the achieved results together with an outlook for future work.

1 Nanowire Growth Mechanisms

The most popular growth mechanism of NWs is the vapour-liquid-solid (VLS) method reported initially by Wagner and Ellis back in the 1960s for the growth of Silicon NWs [2]. Later, several groups [19–21], demonstrated the growth of III-V semiconductor NWs using the VLS method. The potential applications of III-V NWs in technological and scientific domains sparked the interest in NW research and over the years different growth mechanisms of III-V NWs have been identified. In this chapter, various NW growth mechanisms within the scope of the thesis have been briefly reviewed.

1.1 Au-catalyzed vapour-liquid-solid growth mechanism

In a typical VLS growth process, metal nanoparticles (NPs) are deposited on the substrate that serves as a physical and chemical catalyst. The NPs provide a physical site for the incoming semiconductor reactants and also facilitate their activation/decomposition. The most widely used metal catalyst for VLS growth of NWs is gold because of its chemical inertness and its capability of forming eutectic alloys with major semiconductor materials. A schematic illustration of the VLS growth of germanium NWs for the Au/Ge system [22] is schematically illustrated in Figure 1.1(a). The three major steps involved in a VLS growth are I: metal alloying, II: nucleation, and III: NW growth. The growth process is projected in the conventional Au-Ge binary phase diagram in Figure 1.1(b) and Figure 1.1(c) shows the *in situ* TEM images of the different phases of Ge NW growth [22].

The Au catalyst forms a liquid eutectic Au-Ge alloy when the temperature is raised

above the eutectic point (361 °C) which is marked by a phase transition from solid Au and liquid Au-Ge alloy (L) state to a single phase liquid Au-Ge alloy (L) state. This is the alloying process (stage I) as depicted in Figure 1.1(b) and Figure 1.1(c) (iii). By further supplying the Ge precursors; the alloy composition goes beyond the second liquidus line (red solid curve) towards a biphasic region, i.e. solid Ge and liquid Au-Ge alloy (L) state. As the Au-Ge particle reaches a thermodynamically non-equilibrium supersaturation state (Ge weight percentage of 50-60%), the first precipitation of the solid Ge crystal occurs at the solid-liquid interface until an equilibrium state is reached. The precipitated Ge crystal at the solid-liquid interface serves as a nucleation step. This is the nucleation stage of the VLS growth process stage II as depicted in Figure 1.1(b) and Figure 1.1(c) (iv). Once nucleation takes place, a monolayer rapidly grows to cover the whole liquid/solid interface forming one layer of the NW. Continuous supply of Ge precursors causes the composition of the alloy to go beyond the equilibrium composition again creating a new nucleation step driving the NW growth (stage III) as depicted in Figure 1.1(b) and Figure 1.1(c) (v-vi).

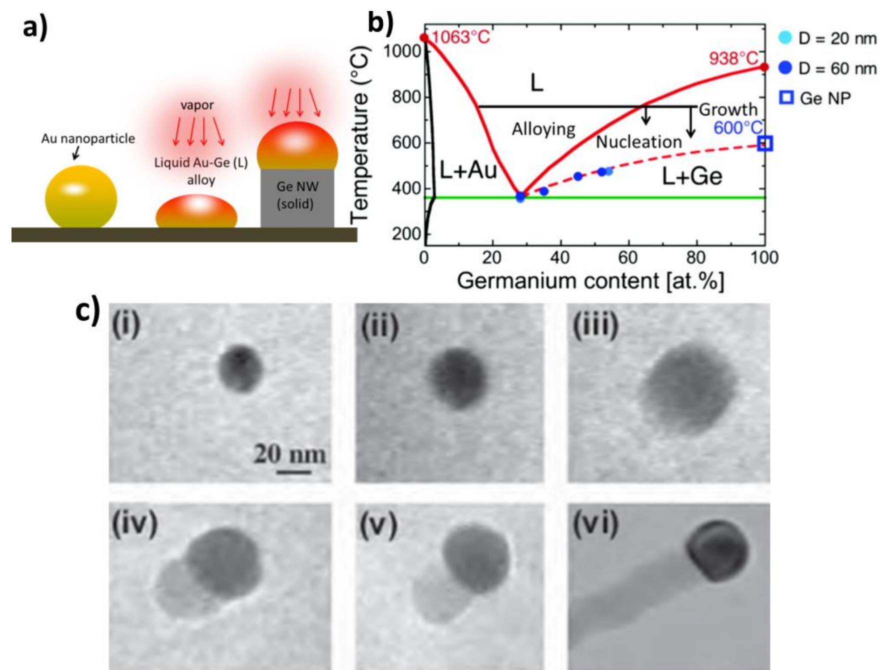

Figure 1.1. (a) Schematic of VLS growth mechanism (b) Au-Ge binary phase diagram. The solid red curve depicts bulk phase liquidus curve and the dashed red curve shows the nanoscale phase curve. Figure is adapted from Ref. [23,24] (c). In situ TEM images recorded during the process of Ge NW growth. (i) Au NPs in solid state at 500 °C; (ii) alloying initiates at 800 °C, at this stage Au exists in mostly solid state; (iii) liquid Au/Ge alloy; (iv) the nucleation of Ge nanocrystal on the alloy surface; (v) Ge nanocrystal elongates with further Ge condensation and eventually a NW forms (vi).Figures are adapted from Ref. [22].

It should be noted that the Au-Ge phase diagrams used to explain VLS mechanism is constructed from bulk systems and could be different for NPs due to melting point depression at the nanoscale [23,24]. Indeed, the nanoscale phase diagram deviates from the bulk phase diagram as depicted by the dashed red curve (Figure 1.1(b)). A comparison between the bulk phase diagram (solid red curve) and nanoscale phase curve (dashed red curve) shows that the nanoscale eutectic temperature is close to the bulk eutectic temperature. Beyond the eutectic temperature, the Au-Ge NPs have higher Ge content than bulk Au-Ge alloy. The lowering of the liquidus line signifies the melting point depression of NPs. Hence, VLS mode with a liquid NP can be maintained down to a hundred degrees below the bulk Au-Ge eutectic temperature (361°C). However, the catalyst may also exist in solid state depending on temperature, precursor fluxes and thermal history [25]. Although the VLS mechanism is inhibited, the NWs continue to grow in a vapour-solid-solid (VSS) mode.

The dynamics of VLS growth of III–V NWs is significantly more complex than that of Si and Ge NWs as three different elements are involved (Au, Group III, and V elements). During the annealing and growth processes, the Au NPs can interact significantly with the substrate and the precursor species to form a ternary (Au-III-V) alloy. For InAs NW growth on InAs (111)B substrates, the inter-diffusion of In into Au occurs extremely fast and the Au NP with a stable In composition is formed during the annealing stage before the growth begins [26]. The alloying process leads to severe decomposition of the InAs substrate [27–29].

On the other hand, the GaAs substrates are much stable and do not interact with Au during the annealing stage; hence, the Au-Ga alloy is formed when the growth begins. Since Arsenic has very low solid solubility in Au, the Au-In and Au-Ga [30] binary phase diagrams can be used to understand the NW growth mechanisms. The binary phase diagrams of bulk Au–In and Au–Ga show eutectic behaviour with eutectic temperatures of 454 °C and 334 °C, respectively such that InAs and GaAs NWs grow by VLS mechanism when the eutectic conditions are met [31].

Once the NW growth has begun, there are two surfaces exposed to the growth precursors: that of the alloyed Au NP at the NW tip and the semiconductor sidewalls. Two families of heterostructured NWs can be achieved by growing a second material on the exposed surfaces by changing the growth parameters: axial and core-shell (radial) heterostructured NWs as shown in Figure 1.2.

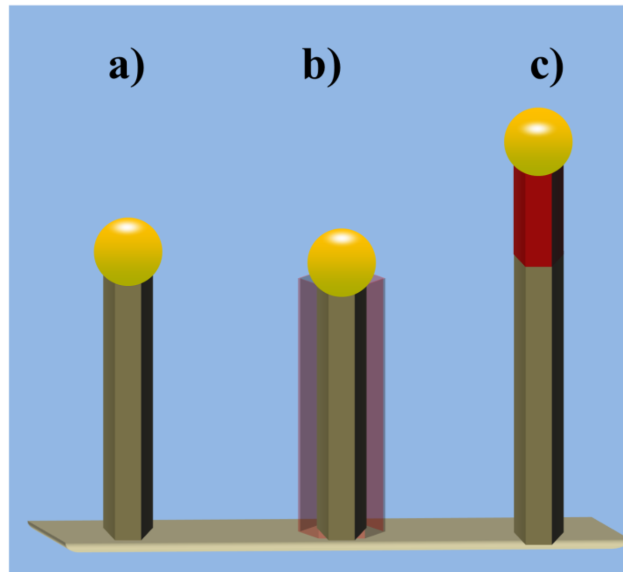

Figure 1.2. Schematic illustration of (a) Au catalyzed NW, (b) core-shell heterostructured NW and (c) axial heterostructured NW. The different colours represent different materials.

The possibility of growing axial heterostructures without forming defects between two different materials with very high lattice mismatch is one of the main advantages of NWs. The axial NW heterostructures can be of particular interest in various applications like single electron transistors [17,32], resonant tunneling diodes [33], optical devices [34], etc. In order to do so, the axial heterostructures must be grown with straight morphology without radial growth and kinking, sharp interfaces and compositional homogeneity.

Considering Au-assisted III-V NWs, straight and abrupt axial heterointerface are easier produced based on the group V interchange in comparison to the group III interchange. Much higher solubility of group III elements in liquid Au increases the reservoir effect, where the group III atoms accumulate in the droplet at the time when the group III interchange occurs and broadens the interface [35]. Another, challenge in growing Au catalyzed axial heterostructures is the kinking of NWs in unwanted directions. In the specific case of InAs-GaAs NW heterostructures, straight axial growth has been reported for GaAs on top of InAs, whereas the other growth sequence i.e. InAs on top of GaAs, usually yields kinked geometries [36,37]. Kinking occurs when interface energies between GaAs, InAs and Au alloy promote island nucleation rather than layer growth at the interface [19]. Kinking can be inhibited by using graded interfaces [38] but to obtain heterostructures with sharp interfaces other strategies must be utilized. A solution to prevent kinked growth is to use conditions that yield high group III content (binary or ternary combinations) in the Au NPs as will be discussed in Chapter 6.

Core-shell NWs can be realized when the surface diffusion length of the adatoms is strongly reduced. This can be achieved by decreasing the growth temperature or growing with a high group-V flux. This condition ensures that not enough material is fed to the alloy particle inhibiting supersaturation. The reduced growth temperature or high group V fluxes enables nucleation of new layers on the NW side facets and sidewall growth occurs by 2D mechanism. Core-shell NW geometry is particularly important for surface passivation and novel NW based devices.

1.2 Au-free growth mechanisms

The Au-assisted approach is the most well-known technique for growing semiconductor NWs. It offers good control over NW morphology, density, position, and crystal structures. Various axial and radial heterostructures have already been realized using Au-assisted NW growth technique [39–41].

Despite the success of Au-catalyzed VLS growth of NWs, the use of Au has many drawbacks. VLS mechanism using Au catalyst introduces the potential for unintentional incorporation of impurities degrading electronic and optical properties of the grown semiconductor [42–45]. Moreover, the use of Au is not compatible with current CMOS technology [42]. Another problem of the VLS mechanism is to grow axial heterostructures with abrupt interfaces especially when there is an interchange of group III material due to the so called reservoir effect. The presence of Au catalyst also makes the growth of core-shell heterostructures challenging due to unwanted axial growth, kinking, and lateral shift of the Au catalyst droplet during the heterostructure formation [37]. To avoid the complexity associated with Au NP, several NW growers etch away the Au NPs from the cores by *ex situ* chemical processing and subsequently grow a shell. Such additional processes may lead to further contamination. Consequently, Au-free techniques, namely catalyst-free (CF) and self-catalyzed (SC) growth of NWs have been addressed to overcome these challenges.

1.2.1 Catalyst-free NW growth mechanism

The catalyst-free (CF) technique is usually preferred in order to grow NWs of high material purity, since no foreign catalyst material is required. The CF growth mechanism is also known as self-induced vapour-solid (VS) growth mechanism and is generally reported for the heteroepitaxial growth of III-V NWs on substrates with high lattice mismatch. For instance, catalyst-free GaN [46], GaAs [47] and InAs [48] NWs

have been grown on silicon substrate that has a lattice mismatch of 16.9%, 4.1% and 11.6% , respectively.

The initial nucleation stage of growth is governed by the formation of islands composed of high-index atomic planes (high surface energy) according to the Volmer-Weber growth mechanism [49]. The islands undergo several shape transitions to form islands with NW morphology under favourable choices of substrate orientation as well as growth conditions [50]. The NW side and top facets correspond generally to the plane of families with the lowest surface energy. The nucleation energy on the NW side facets is generally larger than on their top facet accounting for higher axial growth rate than radial [51]. As an example, TEM micrographs in Figure 1.3(a-d) show the nucleation mechanism of self-induced GaN NWs where spherically capped islands transform into NWs after 17 min deposition at 800 °C with N/Ga fluxes ratio =10.

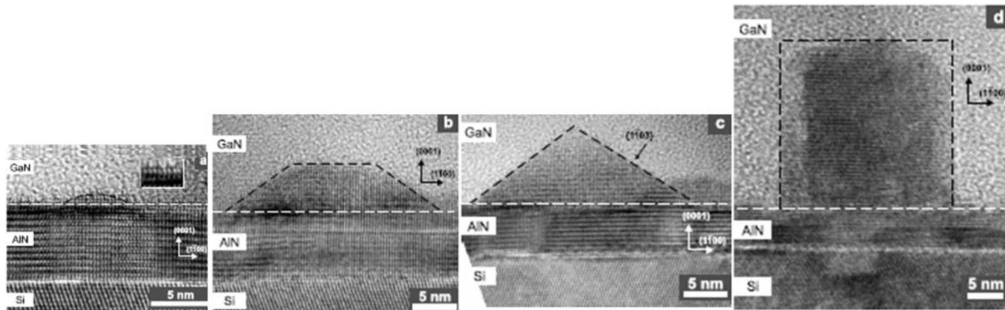

Figure 1.3. (a-d) HRTEM images showing island to NW transition of GaN grown on lattice mismatched AlN layer /Si (111) substrate.Figures are adapted from Ref. [49].

Even though, the initial stage of nucleation is dominated by thermodynamics, the growth phase is instead expected to be dominated by kinetics. Much faster growth on the NW top with respect to the side facets also requires diffusion transport of group III adatoms to the top. Group III adatoms will migrate to the top only if the chemical potential at the top facet is lower than at the NW sidewalls [52]. This property is ensured simply by the fact that the top facet is a more efficient sink of III adatoms relative to the side facets and therefore the III concentration on the NW top is the lowest. The concentration gradient gives rise to a diffusion flux to the top. Therefore, under V-rich conditions and high growth temperature, CF growth of III-V NWs is expected to be limited by surface diffusion of group III adatoms [51].

Analogous to Au-catalyzed NW growth where position and diameter can be controlled, CF NWs with controlled size distribution and position can be obtained by selective-area epitaxy (SAE) [53–55]. Basically, in SAE, the substrate is masked with a patterned SiO_2

layer and growth conditions are appropriately chosen to restrict the growth inside the patterned holes. The fact that growth continues one-dimensionally also above the mask layer, in contrast to lateral overgrowth, is again attributed to the formation of slowly growing side facets with low surface energies [54,55]. Figure 1.4(a) is an SEM micrograph of InAs NWs grown by SAE and Figure 1.4(b) shows a schematic diagram of low index planes around (1 1 1)B on the top facet of an InAs NW [54,55].

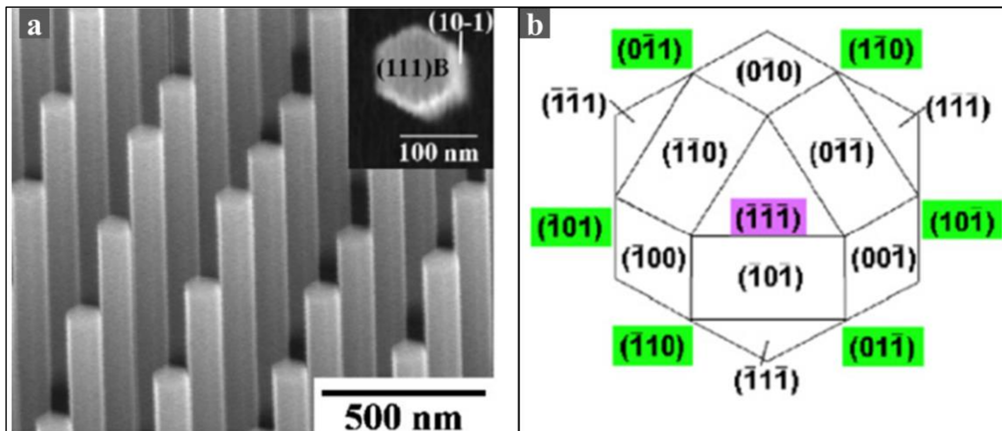

Figure 1.4. (a) SEM image of CF InAs NWs grown by SAE with a top view image of a NW in the inset. (b) Diagram of low index planes around (1 1 1)B plane. Figures are adapted from Ref.[54].

Apart from the advantage of reduced contamination, the CF NWs provide an ideal geometry for growing core-shell heterostructures [56–59]. For efficient growth of core-shell heterostructures, the growth parameters must be such that the ratio between radial and axial growth is maximized. As the axial growth of CF NWs is diffusion-driven, the growth temperatures can be modulated to freeze the adatoms on the sidewalls thereby promoting shell growth and suppressing axial growth. Figure 1.5 shows examples of growing GaSb shell using Au catalyzed and CF InAs core.

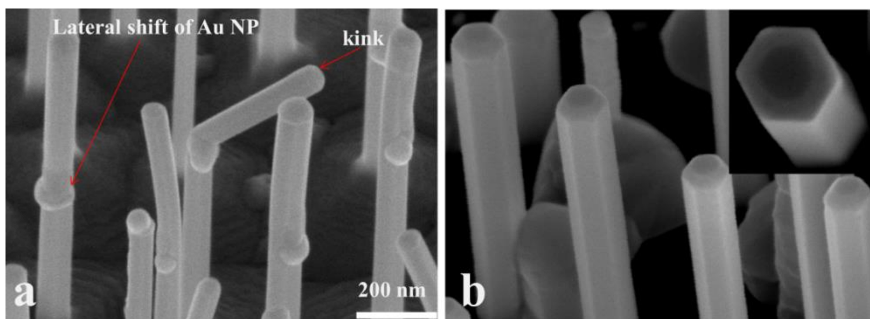

Figure 1.5. (a)Au-catalyzed InAs/GaSb NWs, (b) CF InAs/GaSb NWs grown by chemical beam epitaxy technique.

As seen in Figure 1.5(a), the Au-catalyzed InAs/GaSb NWs feature poor morphology due to kinking and lateral shift of the Au NPs while CF InAs/GaSb NWs shown in Figure 1.5(b) have uniform morphology. The growth of InAs/GaSb core-shell NWs will be discussed in details in chapter 7.

1.2.2 Self-catalyzed (SC) growth mechanism

Alternative to the CF NWs, III-V NWs can also be grown by self-catalyzed (SC) VLS growth mechanism. With this technique, the catalyst is obtained by *in situ* deposition of group III droplets on the substrate (or by initiating the growth in III-rich conditions) instead of the conventionally used foreign metal NPs [60]. Figure 1.6(a) is an example of SC GaAs NWs grown from *in situ* deposited Ga droplets on GaAs/SiO_x substrates and Figure 1.6 (b) shows In-catalyzed NWs grown in In-rich conditions on silicon substrate. Ga and In NPs are clearly visible on the NW tips in Figure 1.6(a) and Figure 1.6(b), respectively.

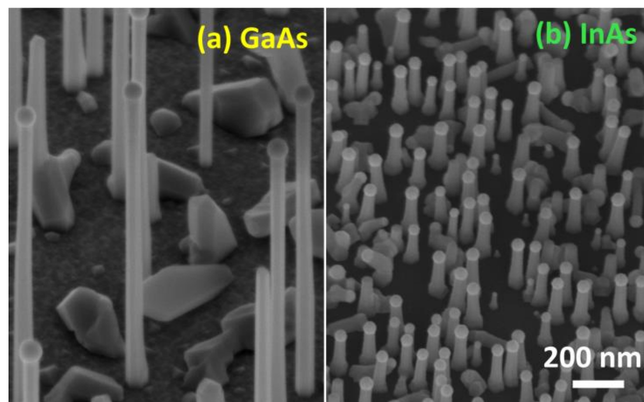

Figure 1.6. Self-catalyzed (a) GaAs and (b) InAs NWs grown by CBE technique.

Similar to the case of Au-catalyzed NW growth, the presence of the NP at the NW tip provides additional degrees of freedom in controlling the structural, compositional and morphological properties of the grown NWs. WZ-ZB superlattice NWs can be grown with good control since the droplet geometry can be changed at will during the growth process [61]. Unlike using Au as a catalyst, the droplet size can be adjusted within the growth chamber [62], which could be exploited to grow NWs with controlled axial and radial heterostructures. In fact, the droplet can be consumed completely and droplets of a different group III element can be selectively placed at the NW tip [63]. Such a control of SC growth mechanism offers very attractive possibilities to grow axial heterostructures with different group III and V elements (such as GaAs/InAs [63],

GaAs/AlGaAs [64], InAs/GaSb [57]) which is challenging in Au-catalyzed NWs due to reservoir and grading effects.

1.3 III-V and silicon integration

The advantages of III-V semiconductors for device applications are well known [65,66]. III-V semiconductors provide high electron mobility and tunable bandgaps that are necessary for electronic and optical applications. In spite of the several advantages, they must be compatible with the present day CMOS technology and therefore needs to be integrated with silicon. III-Vs on silicon render cost effective manufacturing, flexible wafer size, high thermal conductivity and use of matured technology. There has been a considerable effort by academy and industry to epitaxially grow 2D III-V epilayers on silicon substrate. The challenge here lies in reducing lattice mismatch, antiphase domains and thermal coefficient mismatch to produce high quality, dislocation-free and crack-free active layers beyond the critical thickness. Since integration of III-V materials with silicon via a conventional planar epitaxy is challenging, III-V NWs on silicon have been extensively investigated due to their unique 1D geometry. The miniaturized footprint of NW geometry can relieve strain energy by lateral elastic relaxation. Therefore NW can be, in theory, grown infinitely long without generating any dislocations. However, this is true as long as its footprint is smaller than the critical diameter (CD) [67,68]. The CD of NWs is analogous the critical thickness for planar growth, although CD for NWs can be considerably lower than the critical thickness due to its small footprint. When the NW diameter is less than CD, the NW will be coherent solely via lateral relaxation and well-aligned defect-free NWs can grow. When the diameter is larger than CD, NWs either do not grow or grow with dislocations. Figure 1.7 shows the experimental variation of NW CD as a function of lattice mismatch where NWs grow coherently within the diameter range marked by green arrows while NWs do not grow or grow with dislocations in diameter range shown by red arrows due to the inability of the larger diameter NWs to accommodate the strain [68]. In the case of the growth of InAs NWs grown on silicon substrate, which has a lattice mismatch of 11.6%, coherent NWs can be grown up to several micrometres in length with a maximum CD of 24 nm [68]. Although these experimental value was obtained for NWs seeded from Au catalysts, it is presumed that Au-free epitaxial NWs also follow the CD behaviour [69,70].

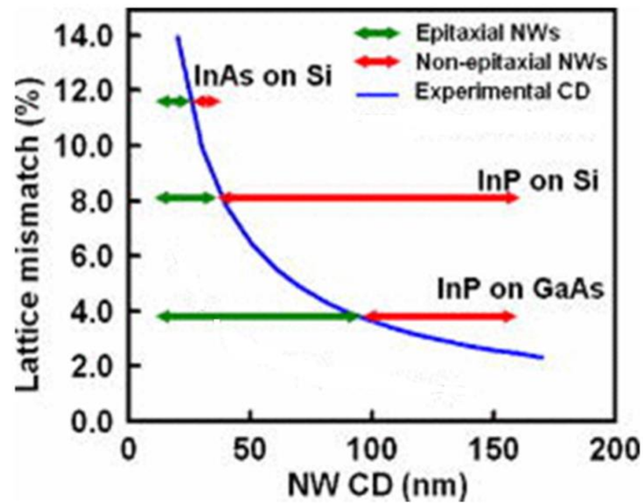

Figure 1.7. Experimental NW CD (solid blue line) as function of lattice mismatch. Green arrows denote that coherent NWs grow within this diameter while red arrows denote NWs that grow with dislocations (or do not grow) Figure is adapted from Ref.[68].

Apart from the limitation of growing superior quality NWs below the CD, there are still many other challenges that are encountered to grow III-V NWs on silicon and must be dealt accordingly. First, III–V NWs on silicon not only grow along vertical <111> but also along three equivalent tilted 19.5° <111> directions azimuthally separated by 120° from each other [71]. Therefore, in order to achieve vertical III-V NWs, the silicon substrates must be prepared accordingly such that the surface reconstruction mimics the III-V(111)B surface as this is the lower energy plane [53,69]. As an example, although various surface reconstructions are possible during annealing [53], the Si (111):As 1×1 is found to mimic InAs(111)B surface ideal for growing vertical NWs as shown in Figure 1.8.

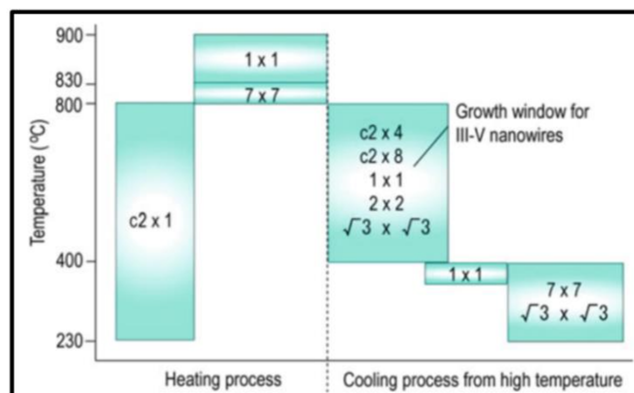

Figure 1.8. Surface reconstruction of Si (111) during annealing and cooling under UHV conditions. Figure is adapted from Ref. [53].

Secondly, CF growth requires high temperature by which the silicon atoms may diffuse into NWs and unintentionally dope the NWs near the heterointerface. Unintentional doping is unfavourable for device applications and proper growth parameters must be chosen to prevent it. Lastly, III-V NWs grown directly on silicon are usually accompanied by unwanted parasitic island growth [72] and islands and NWs continue to nucleate even after long growth times [72,73]. The islands cover substantial fraction of the silicon surface which is further decreased by additional nucleation leading to coalescence of NWs and islands [74,75]. Coalescence not only reduce the density of free-standing NWs, but also results in the deterioration of the NW morphological, structural, and optical properties [74,76]. For most practical purposes, it is desirable to suppress the coalescence process by reducing density or inhibiting new nucleation.

2 Experimental Techniques

Semiconductor NW growth involves the use of sophisticated epitaxy and characterization techniques. Epitaxial technique should be capable of growing high quality NWs both in terms of morphological and structural features. The morphology of NWs can be investigated by using Scanning Electron Microscope (SEM) while the crystal structure can be probed using Transmission Electron Microscope (TEM). Advanced TEM and SEM equipment have added facilities like Energy Dispersive X-ray Analysis (EDX) that can be helpful to know the chemical composition of the grown materials and further understand the NW morphology. Since huge volume of data is generated through growth and characterization experiments, they need to be analysed accordingly to obtain a rationale understanding of the growth mechanisms and to obtain reproducible recipes to control the NW growth. Analysis of NW morphology can be cumbersome and therefore proper statistical analysis tools are necessary. In this chapter, the growth, characterization, substrate preparation, and statistical analysis tools are briefly discussed.

2.1 Chemical beam epitaxy

The Chemical Beam Epitaxy (CBE) is an UHV growth technique [77]. This technique was first realized at the Bell labs in the early 80s to obtain the epitaxial growth of InAs and GaAs films [78,79]. CBE combines the advantages of both MBE [80] and MOCVD [81] along with its own unique and versatile features. All the sources used for growth are metal-organic (MO) compounds, as in MOCVD, but the epitaxial growth is conducted in ultra-high vacuum (UHV) growth chamber, like in MBE, ensuring ballistic flow of precursors. The CBE set-up employed in this thesis for the growth of NWs is a

Riber Compact-21 system located in the Laboratory NEST of Scuola Normale Superiore in Pisa (Italy). A picture of the CBE is shown in Figure 2.1.

2.1.1 Vacuum chambers and pump systems

The CBE system consists of three separate vacuum chambers: the introduction, preparation and growth chambers with its associated pumps. After Indium-bonding the sample on a molybdenum platen inside a glove box, it is placed on a cassette and transferred to the CBE system via an introduction chamber or load-lock. The load-lock is pumped by a turbo-molecular pump with pumping speed of 68 l/s with a membrane backing pump. A pressure of 10^{-8} Torr can be achieved in few hours (1-2 hours) of pumping. The cassette is then transferred to the preparation chamber which is separated from the load-lock by a gate valve. The preparation chamber is pumped by an ion pump which keeps it at a pressure of 10^{-10} Torr. It is also equipped with degassing facility where the substrates can be degassed to remove moisture. The sample is transferred from the preparation chamber to the growth chamber using a magnetic transfer rod. The growth chamber is a stainless steel chamber. The inside walls of the growth chamber are shielded by a cryopanel with circulating liquid nitrogen which allows to reduce the background pressure. Turbo and ion pumps with a pumping speed of 2650 l /s and 550 l/s, respectively, pump the growth chamber. The pressure achieved in the growth chamber is around 10^{-10} Torr. During growth, the gate valve of the ion pump is closed and the chamber is pumped only by the turbo pump. The pressure is in the range of 10^{-5} to 10^{-6} Torr during growth. Such an increase in the pressure in the chamber is mainly due to the presence of group V precursors and MO byproducts (hydrogen and hydrocarbons). Whatever is pumped away, from the growth chamber is lead to a dry scrubber to eliminate the hazardous gases. The growth chamber is equipped with reflection high-energy electron diffraction (RHEED) for *in situ* diagnosis of surface reconstruction, and residual gas analyser (RGA) for measuring the gaseous species. The substrate temperature is measured by a thermocouple that is located at the rear of the substrate holder. Although, the thermocouple provides a reasonable feed-back of the substrate temperature, it does not essentially measure the temperature of the substrate surface. Therefore, for accurate measurement of the substrate temperature, an optical pyrometer is used. The temperature for all experiments in this thesis always refers to the measurement via pyrometer with a ±10°C.

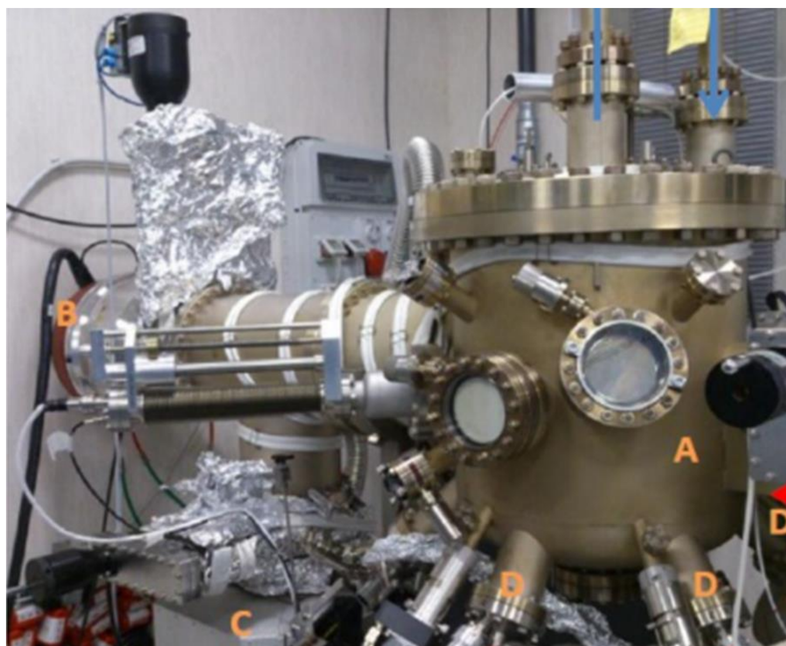

Figure 2.1. (a) Picture of Riber Compact 21 CBE system. A: Growth chamber, B: Turbo pump,C: Ion pump, and D: Injectors.

2.1.2 Gas handling system and injectors

The MOs used as group III precursors are trimethylindium (TMIn), triethylgallium (TEGa) and trimethylaluminum (TMAl). The group V precursors are tertiarybutylarsine (TBAs), tertiarybutylphosphine (TBP), trimethylantimony (TMSb), and tris(dimethylamino)antimony (TDMASb). Ditertiarybutyl selenide (DtBSe) is used a selenium source for n-type doping. The MO sources are stored in a stainless steel bottles with individual heater attached. The bottles are placed in a gas cabinet whose temperature is maintained at around 30 °C. The precursors from the bottles can either be switched to the growth chamber or to the vent chamber by means of run/vent configuration. Figure 2.2 shows a schematic of the gas lines with the run/vent configuration.

In this configuration, the source gas flows are first stabilized in a vent line and then switched into the run line into the growth chamber. For the growth of heterostructures, the run/vent configuration can be utilized to change the materials during the growth. Before the gases are switched to either the growth chamber or the vent chamber, they pass a needle valve and a baratron manometer. The measured pressure is used as a feedback for the pressure control unit which adjusts the needle valve. The precursor fluxes are directly proportional to these regulated pressures. The MO precursors are fed to the growth chamber via three line injectors. The group III MOs is introduced into the

growth chamber via low temperature injectors maintained at 50 °C during growth. They are pyrolyzed at the heated substrate. On the other hand, group V precursors (except TDMASb) are pre-cracked in the high temperature injector maintained at 1000 °C as the substrate temperature is not sufficient to decompose these precursors. TDMASb is decomposed directly on the heated substrate. The gas lines are pumped by a turbo molecular pump backed by a rotary pump. Whatever is pumped away, from the vent chamber is lead to a dry scrubber to eliminate the hazardous gases.

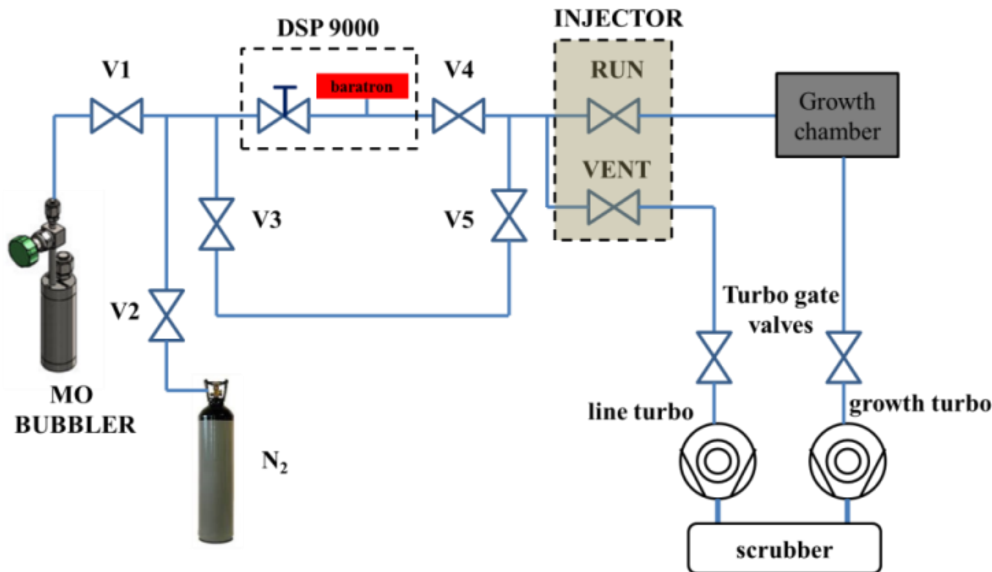

Figure 2.2. Schematic drawing of the precursor gas lines showing the RUN and VENT system.

2.2 Au-catalyst preparation

Au NPs for the growth of Au-catalyzed InAs NWs are obtained through annealing of thermally evaporated Au films or colloidal dispersion.

Au thermal evaporation is a simple method for Au thin film deposition. For the thermal evaporation of Au film, the Kurt J. Lesker thermal evaporator was employed. A small amount of 99.9% pure Au metal wire was placed on a conductive tungsten resistive boat located in an UHV chamber. The substrate was mounted in the vacuum chamber of a thermal evaporator equipped with quartz crystal thickness monitor for evaporation rate and film thickness feedback. Upon reaching a pressure of 5 x 10^{-5} mbar,the tungsten joule-heated boat containing Au was heated until the target 0.01 nm/s rate was reached; then the sample shutter was open until the desired thickness of Au was deposited. With the high precision mass measurement provided by the quartz balance, the Au mass per unit area is controllable to much more than a monolayer average thickness, providing

good control for the amount of gold evaporated on the samples. Most of the substrates were prepared with nominal 0.1, 0.5 or 1.0 nm Au film, although it is possible to prepare substrates with smaller or larger thicknesses for specific purposes.

Concerning the other catalyst preparation method, i.e. colloidal dispersion, InAs substrates are dip for 30 s in a 0.1% Poly-l-lysine solution, rinsed in DI water and blown dry. A drop of colloidal solution was casted on the surface and left there for few minute, then rinsed in DI water and blown dry. Failure to pre-treat the substrate surface with poly-l-lysine leads to extremely low densities and inconsistent results. This is most likely due to positive tails of the poly-l-lysine molecules bonding to the net negative charge on the surface of the colloidal NPs (necessary to avoid agglomeration due to Van der Waals forces and other surface interactions while in solution).

After Au film deposition or Au colloidal deposition, the substrate is mounted in the CBE chamber, and annealed in As flux. The annealing step ensures the removal of the surface oxide, thermal dewetting of Au film and formation of Au-In NPs as shown schematically in Figure 2.3.

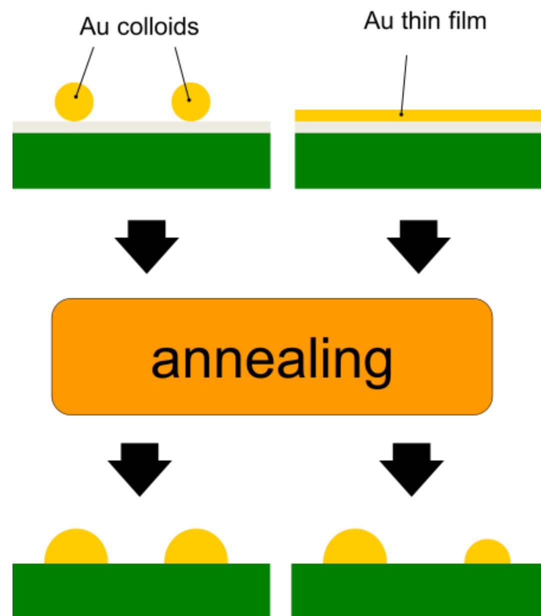

Figure 2.3. (a) Schematic of Au-In NPs formed after thermal annealing of Au colloids and Au film deposited on InAs(111)B wafer.

2.3 Silicon substrate preparation

The substrate preparation protocol for the growth of Au-free InAs is schematized in Figure 2.4. Commercially available Si (111) substrates covered with native oxide layer were used (Figure 2.4(a)). Auger spectra of this substrate displayed in Figure 2.5 (black

curve) shows a peak at ~92 eV which is the elemental silicon peak. A distinct peak at ~76 eV is attributed to the chemically shifted silicon peak from SiO_2 [82,83]. The peak at ~515 eV is generally assigned to oxygen, and stems not only from the oxides but also from adsorbed water and OH groups [84].

Since no NW growth occurred on oxide-covered substrates,the oxide was completely etched away by buffered oxide etch (BOE) having an etch rate of ~90 nm/min for 2 min, rinsed in deionized water and blown dry with nitrogen to obtain hydrogen terminated Si (111) surface. Auger spectra of hydrogen terminated Si (111) (green curve in Figure 2.5) shows that the ~76 eV peak is almost completely suppressed confirming the complete removal of the native oxide. The oxygen peak at ~515 eV is also much smaller than that of Si (111) with native oxide. The residual oxygen detected is mainly due to residual water and OH groups [84].These substrates are termed as "non-sputtered" silicon substrates (Figure 2.4(b)). No NW growth occurred on such a substrate and was therefore subject to further surface treatments (Figure 2.4(c)).

Subsequent surface treatment involved sputtering the silicon surface by controlled Argon or SiO_2 particles (Figure 2.4(d)). Energetic Argon particles are obtained by inductively coupled plasma (ICP) sputtering system (chamber pressure= 1.5×10^{-4} Torr, Ar flow=15 sccm) while SiO_2 particles are obtained by Radio-frequency (RF) magnetron sputtering system (chamber pressure= 1×10^{-4} Torr). The sputtering is controlled by two parameters: the sputtering bias (V_{sputter}) and the sputtering time (t_{sputter}).

Prior to NW growth, the sputtered substrates are etched for 2 min in BOE to remove any form of residuals and deposited oxide. The substrates are rinsed in deionized water and blown dry with nitrogen. These substrates are termed as "sputtered" silicon substrates (Figure 2.4(e)) and used for successful NW growth (Figure 2.4(f)).

Immediately after etching, all substrates are indium-bonded on a molybdenum platen in air by keeping them on a hot plate at 250 °C for less than a minute, transferred to the load lock of the CBE chamber and pumped to 10^{-7} Torr in few minutes. Auger electron spectroscopy of "as mounted" substrates reveals that some silicon oxides are present on the silicon surface (red curve in Figure 2.5), due to the indium bonding procedure. The amount of oxide is, however, very small, but indicates that substrate handling before mounting requires particular care.

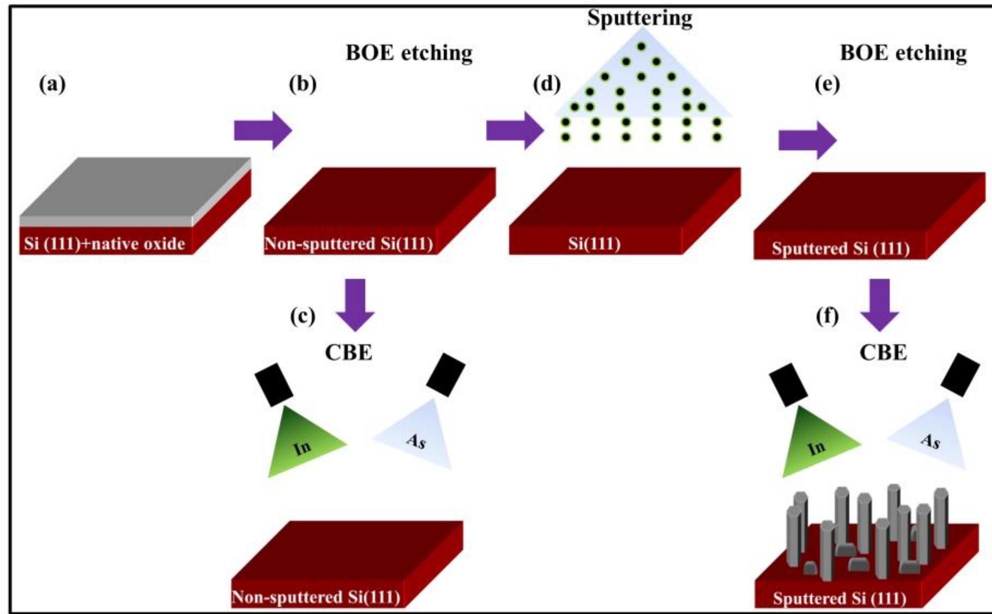

Figure 2.4. (a) Schematic of the process used for substrate preparation for Au-free InAs NW growth on non-sputtered silicon (a-c) and on sputtered silicon (a-f). Figure is adapted from Ref. [85].

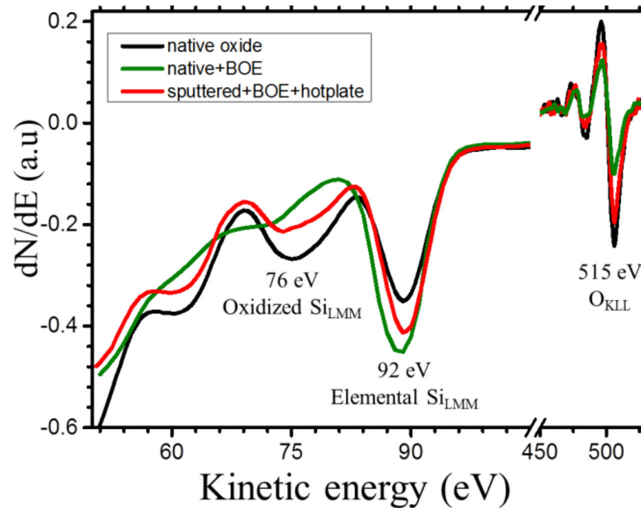

Figure 2.5. Auger spectra acquired from Si (111) with native oxide (black curve), after BOE etching (green curve), and from a SiO_2 sputtered Si (111) surface after etching and placing it on a hotplate for 1 min (red curve). Figure is adapted from Ref. [85].

Figure 2.6(a) and (b) show atomic force microscopy (AFM) images of a non-sputtered silicon and sputtered silicon surface, respectively along with their height profiles in Figure 2.6 (c) and (d). SiO_2 RF magnetron sputtering with parameters $t_{sputter}$ =60 s and $V_{sputter}$=520 V was employed to sputter the silicon substrate. Prior to AFM measurements, the substrates were etched in BOE for 2 min, rinsed in deionized water and blown dry.

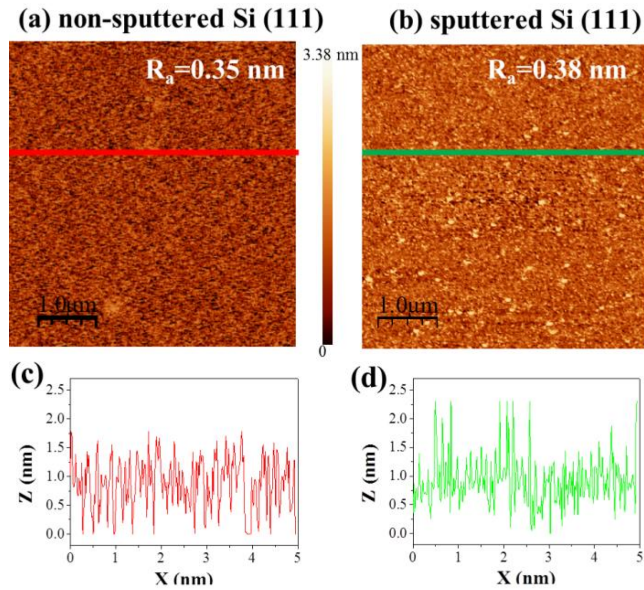

Figure 2.6.AFM image of (a) a non-sputtered silicon surface and (b) a sputtered silicon surface. Line profile across the (c) non-sputtered (red) and (d) sputtered (green) silicon surface. Figures are adapted from Ref. [85].

The non-sputtered surface has an average roughness of 0.35 nm (Figure 2.6(a)) while the sputtered surface (Figure 2.6(b)) has a comparable average roughness of 0.38 nm. Height profiles across the non-sputtered (Figure 2.6(c)) and sputtered (Figure 2.6(d)) silicon surface also shows comparable height variation.

2.4 Electron microscopy

Scanning electron microscope (SEM) is the measurement technique for morphological characterization that is most widely used in the field of physics, chemistry, and semiconductor science. The SEM produces images by probing the specimen with a focused electron beam that is scanned across a rectangular area of the specimen (raster scanning). The SEM has several unique advantages such as simple sample preparation, ability of providing rapid feedback of morphology of as-grown samples, and reduced sample damage. Two different SEMs are used in this thesis: Zeiss MERLIN and Zeiss ULTRA Plus. The Zeiss MERLIN is a field emission gun SEM (FE-SEM) and it can be operated at a maximum acceleration voltage of 30 kV (see Figure 2.7(a)). The core of the MERLIN is the enhanced GEMINI II column which, with its double condenser system, achieves an image resolution of 0.8 nm (see schematic drawing in Figure 2.7(b)). Apart from such high resolution, the MERLIN has also attached Angle selective Backscatter (AsB) and Energy Selective Backscatter (EsB) detectors which offer better

material contrast during imaging. Furthermore, the air-lock mounted on the MERLIN allows a fast mounting and dismounting of the sample within few minutes. The ULTRA Plus is another high resolution FE-SEM having AsB and EsB detectors.

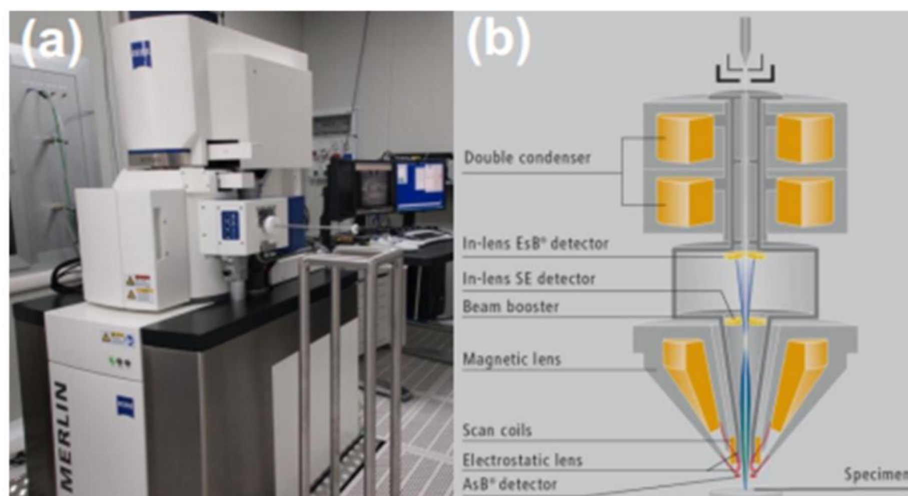

Figure 2.7. (a) MERLIN FE-SEM installed in the cleanroom of Laboratory NEST (b) Schematic drawing of the GEMINI II column.

Structural characterization of the NWs has been conducted by Zeiss Libra 120 TEM. Even though this TEM cannot offer atomic resolution with a 120 kV accelerating voltage, the Libra can offer a fast feedback on both crystal structure and chemical composition of the NWs using the selected area electron diffraction (SAED) imaging and energy dispersive X-ray spectroscopy (EDX). The TEM employed to perform high resolution TEM (HRTEM) images in this thesis is a JEOL 2200FS Field-Emission TEM operated at 200 kV. Furthermore, two Annual Dark Field (ADF) and one Bright Field (BF) STEM detectors are attached to the system and allow to perform high angle annular dark field (HAADF) imaging.

2.5 Statistical analysis

Statistical analysis of diameter and length measurement of the individual Au-catalyzed NWs presented in Chapter 3 has been performed using an in-house developed image analysis software package. Another open source software (ImageJ) has been used concurrently to measure length, diameter, and density of the grown NWs.

2.5.1 Software overview

The software code has been written in Wolfram Mathematica taking advantage of its

extensive library of functions for image and particle analysis. The analysis of each SEM image is divided into four steps: (a) binarization of the greyscale image, (b) recognition of connected areas, (c) elimination of the non-NW areas, and (d) measurement of the quantity of interest. Image binarization is the operation of transforming the 8 bit greyscale SEM intensity image into a binary image. In a binary image, each pixel is assigned a value of either 0 or 1 whether the original images 8-bit value lies above or below a threshold value. The resulting "1" pixels correspond to foreground objects while the "0"s correspond to the background. For most samples the threshold has been chosen automatically using Otsu's threshold selection method [86]. In a few cases of extremely difficult samples, the threshold has been manually chosen to maximize the yield and obtain a statistically relevant ensemble of NW measurements. Figure 2.8(b) is the result of binarization of Figure 2.8(a), where black pixels are 0's, and non-black ones are 1's.

The second phase basically groups connected 1's in individual separate objects that are the basis for NW recognition. This operation is performed by a Mathematica function and takes care of filling holes within the connected areas (ensuring, for example, that darker part of the catalyst NPs at the tip of the NWs are counted as part of the object). For each object, the dimensions of its bounding box (BB, the smallest rectangle with sides parallel to the image sides that contains the whole object) are recorded (see Figure 2.10(a-b).

Recognizing which objects are individual vertically aligned NWs and which are substrate features, kinked NWs or multiple overlapping NWs requires the use of a number of "filters" on the objects obtained so far. First, all objects overlapping the image boundaries are discarded, since they are going to be only parts of NWs, whose dimensions are not significant. Those objects are coloured with a red overlay in Figure 2.8(a). Second, objects below or above a certain total area are discarded. In the example of Figure 2.8(a), one of such objects has a blue overlay. Third, objects whose BB has a height/width ratio below a certain threshold (in most cases 1) are discarded to remove fallen NWs. To discard partially overlapping NWs, the area of the object and of its BB are compared. If object's area is lower than a specified fraction of the BB area, the object is considered as partially overlapping NWs and it is discarded. Such objects have a green overlay in Figure 2.8(a). In some cases, NWs grow slightly tapered or with tapered bases. The large bases make this last filter useless. In those cases, the filter is applied to objects whose base is eroded of a certain number of pixels, to first remove enlarged bases. All the threshold and filter values (upper and lower area, BB aspect

ratio, base erosion and BB/object area ratio) are manually adjusted on test images of each NW sample to find optimal values, using a false-coloured image output (similar to the one shown in Figure 2.8(a)) to mark the results of the individual filters and the selected "good" NWs, carefully keeping to zero or to a minimum (<1-2%) both the "measurable" NWs discarded and the "non-NWs" accepted. Figure 2.8(b) shows in white the accepted objects and in grey the discarded ones. The selected objects (~200 in the worst case, ~10^3 in most cases, up to ~10^4 in a few samples) are then handed over to the measurement algorithm.

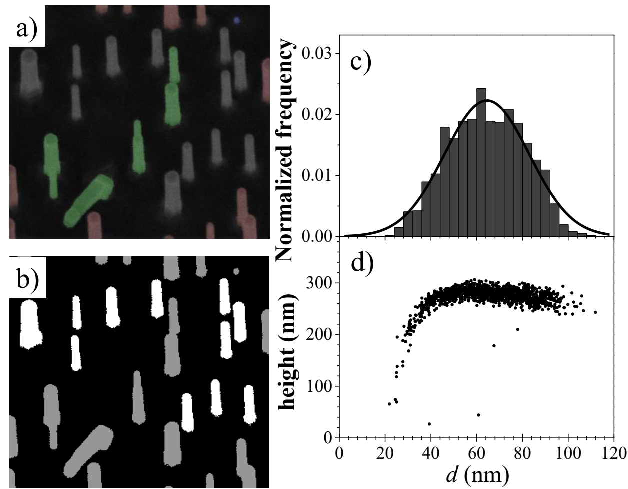

Figure 2.8. Diameter measurement procedure of InAs NWs from SEM images. (a) 20° tilted acquired SEM image of InAs NWs. Red, green and blue overlays mark NWs discarded by various software filters (see text). (b) Same image after binarization; grey objects were discarded by the filters while white ones are measured. (c) Diameter distribution of InAs NWs. (d) NW height plotted as a function of diameter for the NWs shown in the histogram. Figures are adapted from Ref [21].

2.5.2 NW diameter measurement

The "diameter" of the NWs is the width of the objects "near the tip", to avoid bias due to tapering. While "near tip diameter" is a commonly reported quantity in NW literature, measuring it with an automatic algorithm is not straightforward. The "near tip" diameter is the width of the InAs NW at the interface between the catalyst and the semiconductor. We have proceeded as follows: i) define the initial diameter approximation as the average width of the whole object (Figure 2.9(a)); ii) take as new diameter approximation the average width of the object in the height range from 1 to 2 radii away from the highest point in the object (Figure 2.9(b)); and iii) repeat point (ii). Ideally, this cycle should continue until convergence (Figure 2.9(c)). Practically, we

have decided to stop the process after three iterations, since it is the most computationally eager part of the code and algorithm execution time would risk diverging for little advantage in accuracy. The topmost part of the NW -for a height equal to half the diameter- is discarded since it is the catalyst hemisphere whose width varies from zero to the NW diameter. The average is taken only on the next fraction of the height equal again to half the diameter to mitigate tapering effects but still maintain some averaging. The procedure is schematically shown in Figure 2.9, while Figure 2.8(c) shows the histogram of the diameters for a sample, measured on ~1600 NWs out of 23 SEM images.

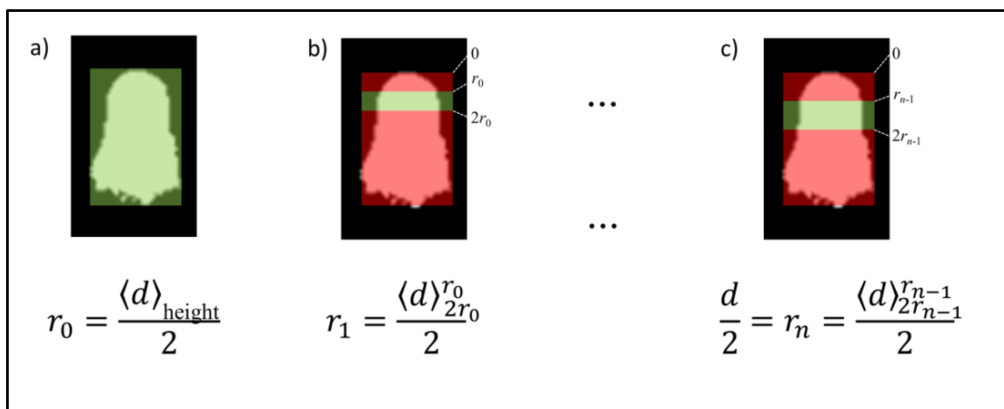

Figure 2.9. Algorithm for determining the near tip diameter from the NW silhouette of Figure 2.8 (see text for details). Figure is adapted from Ref [21].

2.5.3 NW length measurement

The easiest way to measure the NW length would be to tilt the sample by 90° and measure directly the height of the NWs. However, a very large number of NWs would be projected on the image plane and no thresholding would be capable to separate the individual NWs and measure them. The tilt must be lower than 90° in an attempt to reduce NW overlap in the image and easily isolate them from the substrate background to measure the NWs individually. As a rough estimate, for randomly distributed NWs of average height L_{NW} with average density (NWs/substrate unit area) ρ, the imaging tilt angle θ must satisfy $\tan\theta < 2/L_{NW}\sqrt{\pi\rho}$ Obviously when the tilt angle approaches to 0° (top view) no morphological characteristics of NWs can be derived from the SEM image except the extension of its tapered base and –in some cases– the size of the metal catalyst particle. In an intermediate regime (θ~10°-70°) one first approximation would be to consider the NW to be a diameterless stick and thus take the bounding box (BB)

height (see Figure 2.10(a) and (b)) as the projection of the NW height on the image plane: L_{NW}(from BB)=BBheight/sinθ. This is acceptable if BBheight >> $d\cos\theta$, i.e. if the projection of the NW diameter in the image plane is negligible with respect to the height. When the diameter is non-negligible, it is necessary to remove its projection from the BBheight.

If, however, the NWs are tapered or have a large base, then the quantity to be subtracted is the projection of the base radius and that of the tip radius (see Figure 2.10(c)). Tip radius is ½ the "near tip diameter", while a good approximation for base radius is ½ the BBwidth. Both quantities can be easily measured for each NW so the actual NW length can be calculated as shown in Figure 2.10(c). These estimates are exact for NWs with rotational symmetry around their growth axis (i.e. cylindrical NWs with circular cross-section). In case of (regular) hexagonal cross sections things are slightly more complicated by the different widths of NWs and their bases when viewed from two orthogonal orientations such as the <110> or the <211> substrate directions. In the real case of more or less irregular hexagons for both bases and NWs, exact calculation of length from tilted images is precluded. Length vs. diameter data acquired with automatic algorithms must be always carefully screened for systematic (and diameter dependent) biases. Figure 2.8(d) shows the plot of length-diameter distribution for a sample, measured on ~1600 NWs out of 23 SEM images.

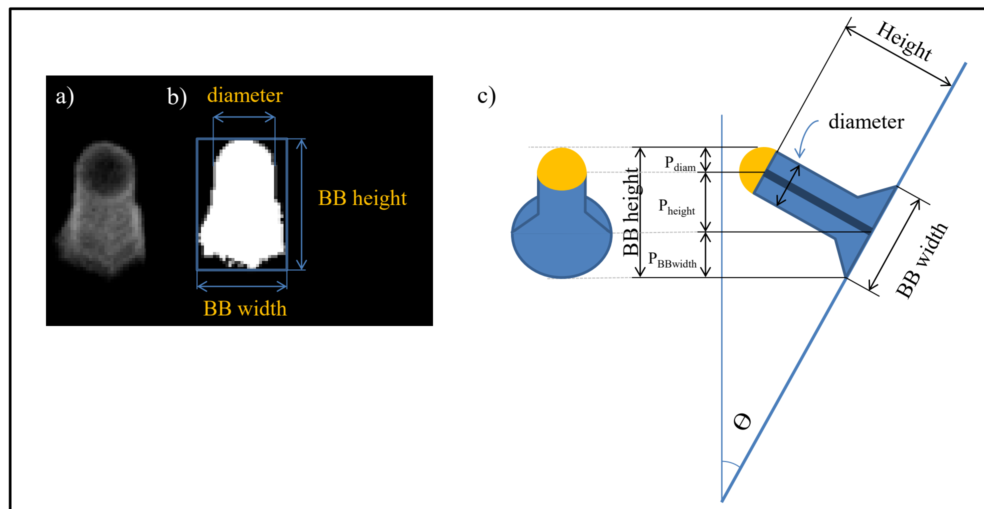

Figure 2.10. Determination of NW height from SEM micrograph. (a) The original greyscale micrograph of a NW, acquired with the sample tilted at an angle θ=20°. (b) NW binary silhouette obtained by thresholding the image in (a); the bounding box (BB) is indicated, along with the near tip diameter. (c) Reconstruction of the NW real height from the quantities measurable on the tilted image. Figure isadapted from Ref [21].

3 Au-catalyzed InAs NWs

The size uniformity of NWs is a crucial parameter for various photonic and electronic applications of III-V NWs grown by Au-catalyzed VLS mechanism. In fact, NW diameter defines its crystal structure and therefore determine its electronic and optical properties [3–7]. The NW diameter can be controlled directly by controlling the Au NPs [87–89]. NWs with uniform length are also a primary requirement for their suitability to be used in devices.

In this chapter, we investigate the influence of the two different Au NP preparation methods as described in section 2.2 to realize InAs NW with controlled morphology. Au NPs are obtained by thermal dewetting of Au film and colloidal dispersion. We present experimental data on the diameter and length distributions of Au-catalyzed InAs NWs. The length distributions are also described with a rate equation model that fits and explains the experimental data. This chapter includes content from: U. P. Gomes, D. Ercolani, V. Zannier, F. Beltram and L. Sorba, Semiconductor Science and Technology, 30, 115012 (2015) and V. G. Dubrovskii, N. V. Sibirev, Y. Berdnikov, U. P. Gomes, D. Ercolani, V. Zannier and L. Sorba, Nanotechnology, 27, 375602 (2016).

3.1 Growth protocol of Au-catalyzed InAs NWs

Figure 3.1 illustrates the scheme of VLS growth mechanism employed for growing InAs NWs as already described in chapter 2. Figure 3.1(a) shows the deposition of Au film (top) and colloidal NPs (bottom) dispersed on a InAs (111)B substrate. At high temperature the metal catalyst together with the substrate material form a liquid Au-In eutectic alloy as shown in Figure 3.1(b). By supplying the growth species, the particle reaches a supersaturation state leading to nucleation at the solid-liquid interface.

Continuous supply of growth species leads to one-dimensional NW growth with the NP on the NW top as shown in Figure 3.1 (c).

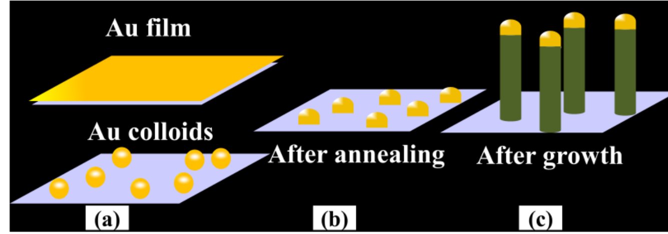

Figure 3.1. Schematic of the growth procedure: (a) Au film deposited (top) and Au colloids (bottom) dispersed on InAs (111) B substrates, (b) Au NPs formed after annealing and (c) growth of InAs NWs . Figure is adapted from Ref [21].

All Au-catalyzed InAs NWs were grown following the same protocol, regardless of the Au deposition method: (i) temperature ramp, from standby (~250 °C) to T_{ann} at a 30 °C/min rate, under a TBAs line pressure of 1.00 Torr; (ii) annealing at T_{ann} for a time t_{ann} still under TBAs flux. The annealing step ensures the formation of Au-In NPs by thermal dewetting of films and the surface oxide desorption from the InAs substrate; (iii) temperature ramp down from T_{ann} to a growth temperature of 390 °C, at 10 °C/min; (iv) growth at P_{TMIn}= 0.3 Torr and P_{TBAs} =0.7 Torr for a growth time of t_{growth}, respectively; (v) cool down to ~250 °C at ~20 °C/min with no TMIn and with a linearly decreasing TBAs line pressure from 0.70 to 0 Torr.

Diameter and length measurement of the individual NWs has been performed using the image analysis software package described in chapter 2. d_{avg} is the arithmetic mean of the resulting measured NW diameter of each sample while the diameter of each individual NW is denoted by d. The diameter standard deviation for each sample is denoted by δd. When the diameter distribution is fitted by a Gaussian, its width (standard deviation of Gaussian) is denoted by σ and the centre by d_c. Relative standard deviation (Δd) is calculated as $\delta d/d_{avg}$ (or σ/d_c for Gaussian distributions). The NW length L_{NW} is presented in terms of number of monolayers s (L_{NW} = hs, with h as the height of a monolayer=0.35 nm and s = 0, 1, 2 ...).

3.2 Diameter distribution and density of Au-catalyzed InAs NWs

In this section, we investigate the influence of the two different Au NP preparation methods on the diameter distribution and density of InAs NWs.

3.2.1 Au film thickness dependence

The Au film thickness (h_{Au}) is an important parameter that determines the diameter distribution of NWs. InAs NWs were realized by Au film annealing at T_{ann}=510 °C and t_{ann}=20 min with h_{Au} of 0.1, 0.5 and 1.0 nm. Figure 3.2 shows the NW diameter distribution for the three initial h_{Au}. Gaussian fits of the data are shown as lines.

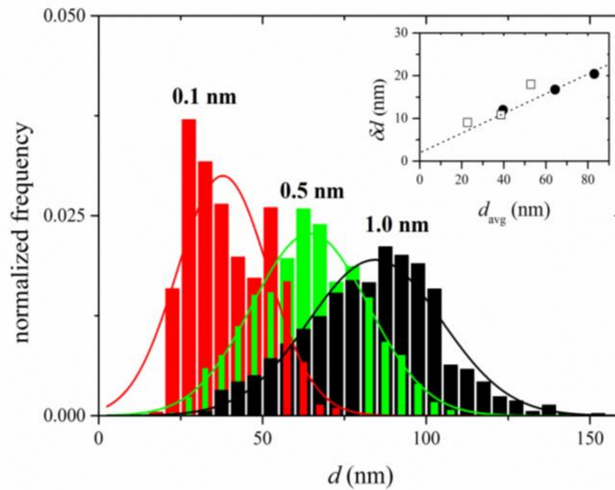

Figure 3.2. Diameter distribution of InAs NWs at fixed T_{ann}=510 °C and t_{ann}=20 min and different h_{Au}: 0.1 (red), 0.5 (green), and 1.0 nm (black). The superimposed lines are Gaussian fits of the data. The inset is a plot of δd versus d_{avg} for the samples shown in histogram (circles) while the squares are the corresponding values of NPs obtained after annealing of Au films and prior to NW growth. The dotted line in the inset is a guide to the eye. Figure is adapted from Ref [21].

The NWs grown from the smallest thickness of Au film have diameters ranging from 20 to 75 nm and the corresponding d_{avg} (δd) is 40 (12) nm. The average NW diameter increases to d_{avg} (δd) =64 (17) nm and NW diameter is distributed between 25 and 110 nm when h_{Au} is increased to 0.5 nm. In case of h_{Au} =1.0 nm, the average NW diameter is the largest with d_{avg} (δd) of 83 (20) nm and NW diameter varying from 30 nm to 150 nm. The inset in Figure 3.2 illustrates the variation of δd as a function of d_{avg} of NWs (circles) while the average of the NP diameters after annealing but before the NW growth are shown as empty squares. As we can observe, δd increase linearly with increasing d_{avg}, implying a roughly constant Δd, for both NWs and NPs, and showing that the diameter distribution of the NWs is strongly correlated to that of the NPs formed during annealing step. Furthermore, the NW density decreases when h_{Au} is increased from 0.1 to 1.0 nm as a consequence of annealing of thicker films yielding

NPs with lower density in analogy to the reported results [90–92].

3.2.2 Annealing temperature dependence

Also annealing temperature of the Au film has an influence on the diameter distribution of NWs. InAs NWs were grown by systematically varying T_{ann} (480, 510, and 540 °C) while fixing t_{ann}= 5 min and h_{Au}=0.1 nm. The diameter distributions are illustrated in the histograms of Figure 3.3, where d_{avg} is increasing with increasing T_{ann}. For T_{ann}=480 °C, d_{avg} (δd) *is* 22 (5) nm. d_{avg} (δd) increases to 35 (6) nm by increasing T_{ann} to 510 °C. A further increment of T_{ann} to 540 °C also shows similar behaviour. In fact, d_{avg} (δd) increases to 47 (11) nm. As shown in the inset of Figure 3.3 an increase in d_{avg} is accompanied by increase in δd resulting to a roughly constant Δd.

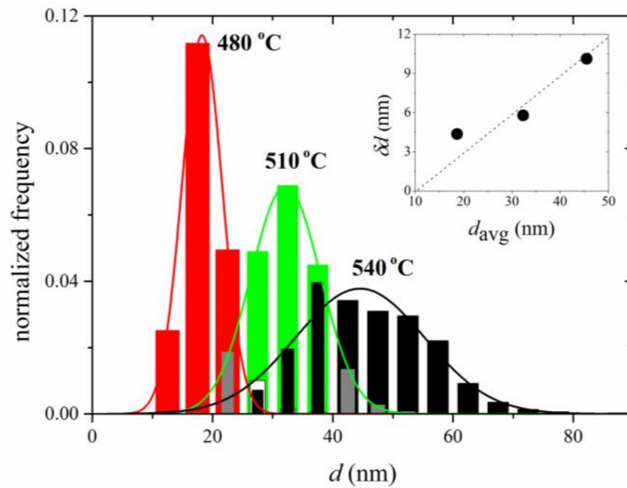

Figure 3.3. Diameter distribution of InAs NWs at fixed h_{Au}=0.1 nm and t_{ann}= 5 min for different T_{ann}: 480 °C (red), 510 °C (green), and 540 °C (black). The superimposed lines are Gaussian fits of the data. The inset is a plot of δd versus d_{avg} for the samples shown in the histogram. The dotted line in the inset is a guide to the eye. Figure is adapted from Ref [21].

The influence of T_{ann} on NW diameter distribution can be accounted for by two main mechanisms: Ostwald ripening (OR) and coalescence of Au NPs [93,94] . OR is a competitive mode of growth among NPs of different sizes, according to which larger NPs grow at the expense of smaller NPs through material exchange driven by Gibbs-Thompson effect. Coalescence implies an increase in particle size by merging the NPs as they diffuse on the substrate. Several models have been used to fit the diameter distribution profile of NPs and NWs to understand the underlying mechanisms [94–98]. Although OR is frequently reported as the main mechanism leading to NP diameter

increase and scattering [47,90,98,99], it is difficult to determine the primary mechanism involved in our NW growth based only on the diameter distribution and the effect of coalescence cannot be excluded [92,100]. Nevertheless, both OR and coalescence are diffusion-driven and thus thermally activated. Both increase the average particle size with increasing temperature [90,101]. As a consequence, d_{avg} and δd are minimum at lowest T_{ann}=480 °C and maximum at the highest T_{ann} = 540 °C. The increase in d_{avg} with increasing temperature is also accompanied by decrease in NW density. Annealing of Au films at higher temperatures yields Au NPs with larger diameter and therefore for material conservation results to lower NP density, which is reflected in lower NW density.

3.2.3 Annealing time dependence

Another degree of freedom to modulate the NW diameter is the annealing time. The histograms and the Gaussian fits in Figure 3.4 show NW diameter distribution for t_{ann}= 5 and 20 min with h_{Au}=0.5 nm and T_{ann}=510 °C.

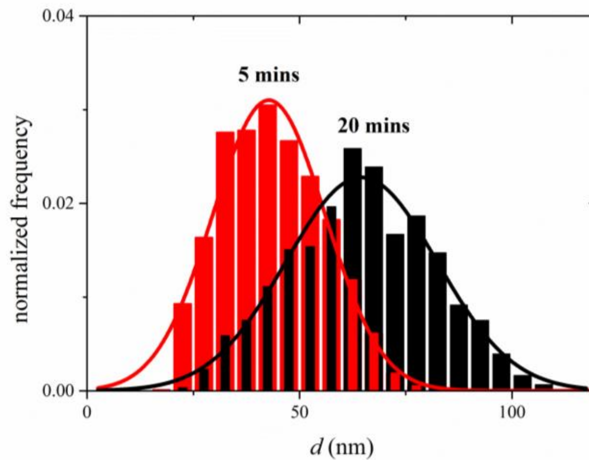

Figure 3.4. Comparison of InAs NW diameter statistics at a fixed h_{Au}=0.5 nm and T_{ann}=510 °C and annealed with t_{ann}= 5 min (red) and 20 min (black). Figure is adapted from Ref [21].

The peak of the histogram shifts to higher diameter upon annealing time increase. At t_{ann}= 5 min d_{avg} (δd) is 47 (13) nm. Within the next 15 min of annealing d_{avg} (δd) increases to 66 (17) nm. The effect of t_{ann} on NW diameter distribution was further investigated on a larger time frame (Figure 3.5). InAs NWs were grown for time series of t_{ann}= 5, 20, 40, 60, and 80 min with h_{Au}=0.5 nm and T_{ann}=470 °C. d_{avg} and δd both increases with increasing t_{ann}. The change in NW diameter distribution with t_{ann} is likely

driven by OR and/or coalescence. Shorter t_{ann} produces more uniform and small Au NPs and therefore NWs with small diameters and relatively smaller standard deviation. Concurrently, the average NW density is also higher at shorter t_{ann}.

However, it is important to note here that OR and/or coalescence is strongly dependent on the initial distribution of the NPs. A clear evidence of these mechanisms is observed when the same sample is monitored over a large time scale by real time in situ microscopic techniques [98,99,102–105]. In growth systems as in our case, the time evolution is investigated on different samples, where initial particle size distribution may vary from sample to sample due to thermal fluctuations which are intrinsically difficult to control in detail in growth reactors. Although these differences influence the final NW diameter distribution, a general trend of increase in d_{avg} and δd and reduction of density with increasing t_{ann} is deduced from all series investigated. An example of one of these series is depicted in Figure 3.5.

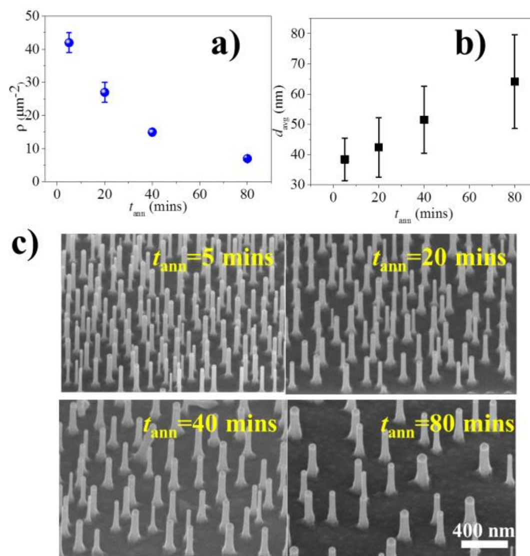

Figure 3.5. Variation of (a) InAs NW density ρ and (b) average diameter d_{avg} as a function of annealing time t_{ann} for h_{Au}=0.5 nm and T_{ann}=510 °C. (c) 45° tilted SEM micrographs of InAs NWs whose ρ and d_{avg} are plotted in (a) and (b).

Figure 3.5(a) and (b) show the variation of NW density (ρ) and d_{avg} as a function of t_{ann} at a fixed T_{ann}=510 °C and h_{Au}=0.5 nm, respectively. Figure 3.5(c) shows 45° tilted SEM micrographs of InAs NWs whose ρ and d_{avg} are plotted in Figure 3.5(a) and (b). Reduction of ρ (Figure 3.5(a)) and increase in d_{avg} and δd (Figure 3.5(b)) with increasing t_{ann} can be clearly inferred from this analysis.

3.2.4 Au colloidal dependence

We have employed a second method to seed NW growth which is the deposition of mono-disperse Au colloidal NPs in water solution on the substrate using the procedure discussed in chapter 2. Figure 3.6 shows the diameter distribution of InAs NWs grown from Au colloidal NPs of different initial diameters at T_{ann} = 465 °C and t_{ann} =20 min. We found that d_{avg} is larger than the average diameter of initial colloidal NPs. In particular, d_{avg} of 29, 45, 55, 78 and 108 nm are measured for 20, 30, 40, 60, and 80 nm NPs, respectively. In the inset of Figure 3.6 δd (circles) is plotted as a function of d_{avg}. Use of d_{avg} and δd as descriptors of the NW diameter distribution is, however, questionable in this case. All histograms present multiple peaks, while arithmetic average and standard deviation correspond to centre and width for normally distributed data. Therefore σ (squares) obtained from the main Gaussian peak is plotted as a function of the peak center, d_c.

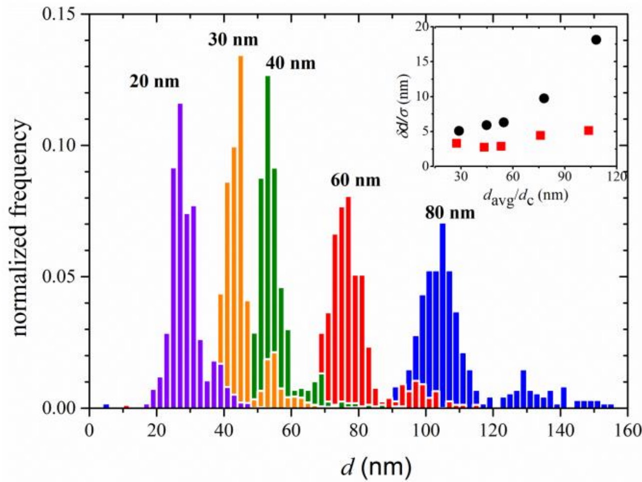

Figure 3.6. Diameter distributions of InAs NWs grown from colloidal NPs of diameter 20, 30, 40, 60, and 80 nm at T_{ann} = 465 °C and t_{ann} =20 min. The inset is a plot of δd versus d_{avg} (circles) and σ versus d_c (squares) for the samples shown in histogram. Figure is adapted from Ref [21].

As an example, a more detailed analysis of the data of one of the NW diameter distributions (80 nm colloids) is plotted in Figure 3.7. The distribution is obviously the superposition of multiple peaks. It can be excellently fitted by three Gaussians, with all three areas and widths left as free parameters. The three centres of the Gaussians are, instead, a single parameter: d_{c1} is the centre of the leftmost Gaussian, while d_{c2} (d_{c3}) has been fixed to $\sqrt[3]{2}\, d_{c1}$ $\sqrt[3]{2d_{c1}^3}$ ($\sqrt[3]{3d_{c1}^3}$), that corresponds to the diameter of a particle having 2 (3) times the volume of a single particle. This is easily understood as the initial

dispersion of colloidal NPs on the InAs substrate frequently shows bonded pairs of NPs, more rarely three linked NPs and in some cases larger agglomerates (see inset of Figure 3.7). When annealing the samples, multiple nearby colloids merge into one single particle, giving rise to NWs with diameters scaling as described above. When only individual colloid NPs seed the growth of NWs (whose distribution is represented by the left most peak), d_{avg} (=d_{c1}) is 104 nm, σ_1 = 5 nm and Δd (=σ_1/d_{c1}) is 5%. When NW growth is seeded from agglomerated NPs, multiple peaks are formed in the diameter distribution and d_{avg} and δd increases to 108 and 18 nm, respectively with Δd=17%. The difference between standard deviation of the whole ensemble of NWs, δd, and of the width of only the leftmost peak (σ) is shown as arrows in Figure 3.7. This behaviour is common to all the samples grown with different Au colloidal NPs. Although agglomerated colloids are present in different extent in the different samples, the single NPs lead to NW diameter dispersion comparable to the initial NP dispersion.

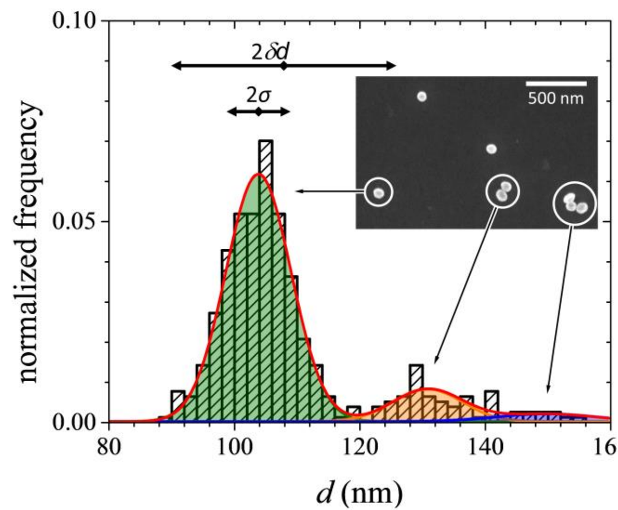

Figure 3.7. Diameter distribution of InAs NWs grown from 80 nm colloids at T_{ann} = 465 °C and t_{ann} =20 min. The histogram shows three peaks corresponding to NWs seeded from single and agglomerated colloidal NPs as pointed by arrows from the SEM micrograph in the inset. The line is a Gaussian fit superimposed on the data. δd obtained from the statistics of NWs grown from both single and agglomerated colloids is larger than σ of the leftmost Gaussian corresponding to the diameter distribution of NWs grown from single colloids. Figure is adapted from Ref [21].

Furthermore, the NW diameter distribution seeded from colloids has also been investigated as a function of T_{ann} and t_{ann}. Unlike in NWs grown from thin film annealing where NW diameter increases systematically with increasing T_{ann} and t_{ann}, due

to OR and/or coalescence, no considerable change in NW diameter was observed in case of colloids for T_{ann} in the range 435-495 °C (see Figure 3.8 (a)) and t_{ann} between 2 and 20 min (see Figure 3.8 (b)). In comparison to thermally dewetted Au NPs, the colloids seem less affected by OR/coalescence, probably due to their initial lower density which makes both mechanisms less effective due to the large particle to particle distance. The major factor influencing d_{avg} and δd of NWs seeded from Au colloids lies in the initial substrate preparation. Agglomeration of colloidal NPs by Van der Waals force during substrate preparation is the primary mechanism that increases d_{avg} and δd in NWs [20,106].

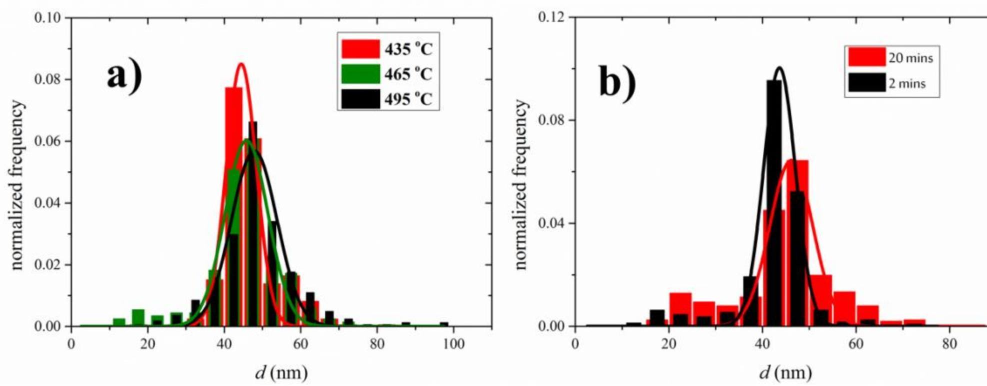

Figure 3.8. Comparison of InAs NW diameter distribution at a fixed colloid size of 30 nm as a function of (a) annealing temperature for a fixed annealing time of 20 min and (b) annealing time for a fixed annealing temperature of 465 °C.

3.2.5 Comparison of diameter distribution and density between the two NP preparation methods

A comparison of the NW diameter distribution grown from dewetting of Au thin film and colloids is shown as plot of Δd versus d_{avg} in Figure 3.9. The data shown spans over a wide range of parameters obtained by systematically changing colloid sizes, T_{ann}, t_{ann} and h_{Au}.

From Figure 3.9, it is seen that InAs NWs obtained from annealing of Au films have Δd (stars) in the range 20-40% giving a reasonable control of NW diameters although the dispersion grows larger as the diameter is increased. On the other hand, Δd of InAs NWs prepared by Au colloids (circles) is in the range 10-20%. Δd of colloids can be tailored to lower values (<10%) if NWs are grown only from single colloids by fine tuning the deposition process to reduce agglomeration (squares). This range of Δd matches that of initial colloidal NPs (5-7% marked by the shaded area in Figure 3.9).

Hence, colloidal NPs is the catalyst of choice where exact and reproducible NW diameter is necessary.

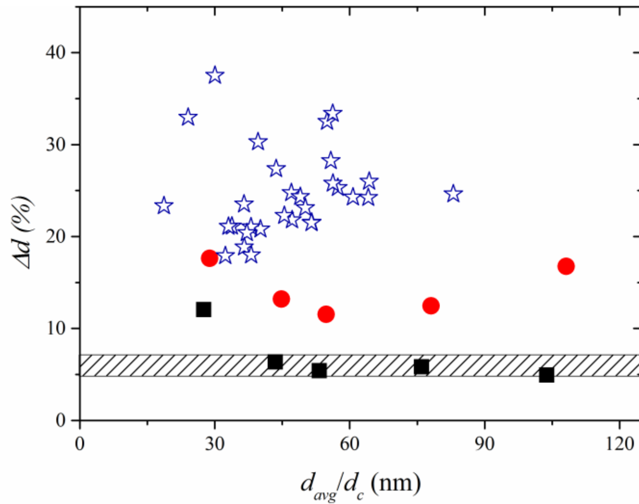

Figure 3.9. Comparison of Δd of InAs NWs grown from Au film (stars) and colloids (circles) as a function of d_{avg}. The squares represent Δd obtained from the main Gaussian peak and plotted as a function of d_c. The shaded region is the relative standard deviation of initial Au colloidal NPs as supplied by the manufacturer (5-7%). Figure is adapted from Ref [21].

So far we have mainly discussed about the NW diameter. However, NW density is, in some cases, as fundamental as the diameter since growth kinetics, NW morphology, and other important NW parameters may depend strongly on it [107–109]. Figure 3.10 is a plot of NW density when moving from one edge to the center of a 10×10 mm^2 sample for NWs seeded from 30 nm colloidal NPs and thermally dewetted NPs from a 0.5 nm thick Au film.

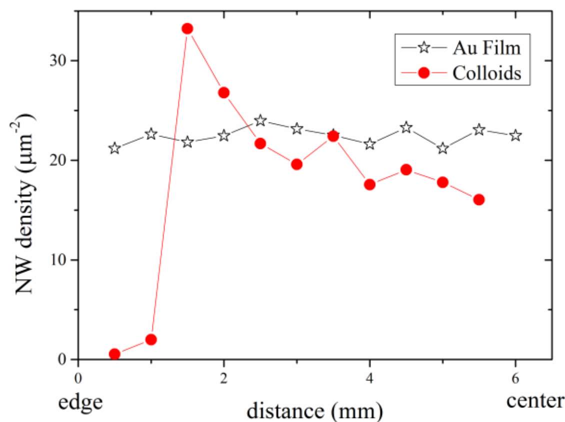

Figure 3.10. Comparison of NW density along the sample surface demonstrating high uniformity for NWs obtained from annealing of 0.5 nm Au film (stars). NWs obtained from 30 nm colloidal NPs (circles) are distributed non-uniformly. Figure is adapted from Ref [21].

A summary of the advantages and disadvantages of the two NW catalyst preparation methods is provided in table 3.2. It is clear that colloidal NPs is the catalyst of choice where exact and reproducible NW diameter is necessary. Very low dispersion is achievable if NP agglomeration is avoided. The initial investment for sample preparation is negligible, limited to the colloid purchase and some cheap labware. Conversely, a reasonable control of NW diameters can be obtained also by thin film annealing, although the dispersion grows larger as the diameter is increased. The strong advantage of thin film annealing is the wafer-scale uniformity and wafer-to-wafer reproducibility of the NW density and diameters, although a thin film deposition facility must be available, implying a much higher initial investment compared to the colloids.

Table 3.2. Summary of advantages and disadvantages of the two preparation methods.

<table>
<tr><th colspan="2">Feature</th><th>Film</th><th>Colloids</th></tr>
<tr><td rowspan="3">NW diameter</td><td>Average</td><td>Good</td><td>Excellent</td></tr>
<tr><td>Dispersion</td><td>Fair</td><td>Excellent</td></tr>
<tr><td>Reproducibility</td><td>Good</td><td>Excellent</td></tr>
<tr><td rowspan="3">NW density</td><td>Value</td><td>Good</td><td>Poor</td></tr>
<tr><td>Homogeneity</td><td>Excellent</td><td>Poor</td></tr>
<tr><td>Reproducibility</td><td>Good</td><td>Poor</td></tr>
<tr><td colspan="2">Initial investment</td><td>Fair</td><td>Negligible</td></tr>
</table>

3.3 Length distribution of Au-catalyzed InAs NWs

In this section, we investigate the influence of two different Au NP preparation methods on the length distribution (LD) of Au-catalyzed InAs NWs. The experimental data are explained using theoretical model obtained from rate equations.

3.3.1 Experimental results

Figure 3.11 shows the normalized LDs of InAs NWs seeded by thermally dewetted Au NPs formed from 0.5 nm thick Au film at T_{ann}= 510 °C and grown for t_{growth}=20 and 45 min along with their corresponding SEM micrographs. The LDs of NWs are fitted with sharp Poissonian lines.

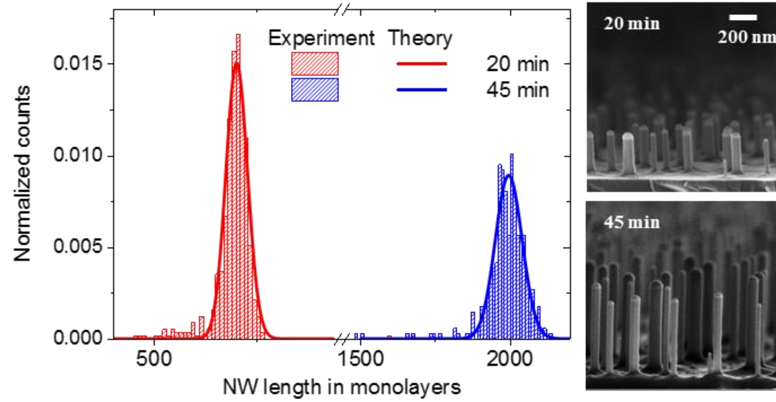

Figure 3.11. (a) Normalized LDs (histograms) fitted by the Poissonian shapes (lines) for Au-catalyzed InAs NWs grown from thermally dewetted Au NPs formed by annealing 0.5 nm thick Au film for t_{growth}=20 and 45 min along with their corresponding 90° tilt SEM micrographs. Figure is adapted from Ref. [110].

Figure 3.12 shows the LDs of InAs NWs grown from 40 nm Au colloids with the standard annealing procedure (T_{ann}= 510 °C and t_{ann} =20 min under P_{TBAs}=1.0 Torr) for t_{growth}=60 and 130 min along with the corresponding SEM micrographs.

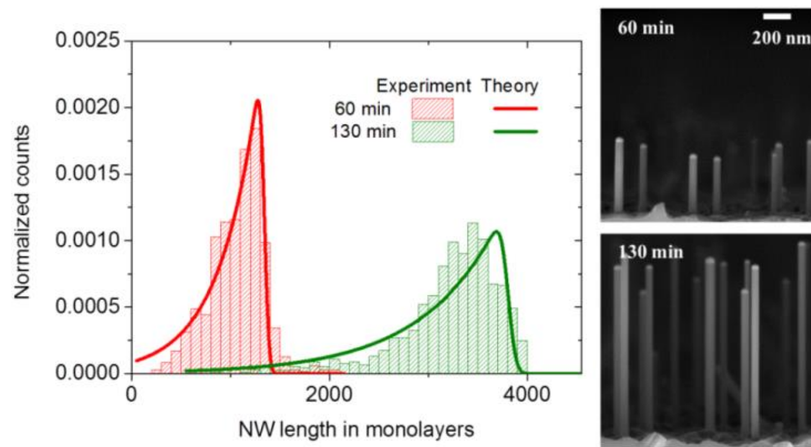

Figure 3.12. Normalized LDs (histograms) fitted by the model (lines) as discussed below of Au-catalyzed InAs NWs grown from 40 nm colloids at 500°C for t_{growth}=60 and 130 mins along with their corresponding 90° tilt SEM micrographs. Figure is adapted from Ref. [110].

These NWs feature much broader LDs with a long left tail that spread with the growth time. Clearly, no new Au NPs can emerge after starting the InAs deposition and thus the striking difference in the LD shapes between Figure 3.11 and Figure 3.12 should be associated with a much longer nucleation step of InAs NWs grown from colloidal Au NPs in comparison to thermally dewetted Au NPs formed from 0.5 nm thick Au film.

In fact, we noticed that during the standard annealing step (T_{ann}= 510 °C and t_{ann} =20

min under P_{TBAs}=1.0 Torr) the colloidal Au NPs dig deep into the substrate, as shown in the SEM micrographs in Figure 3.13(a). The same behavior is obtained even when T_{ann} is reduced to 380 °C (not shown).

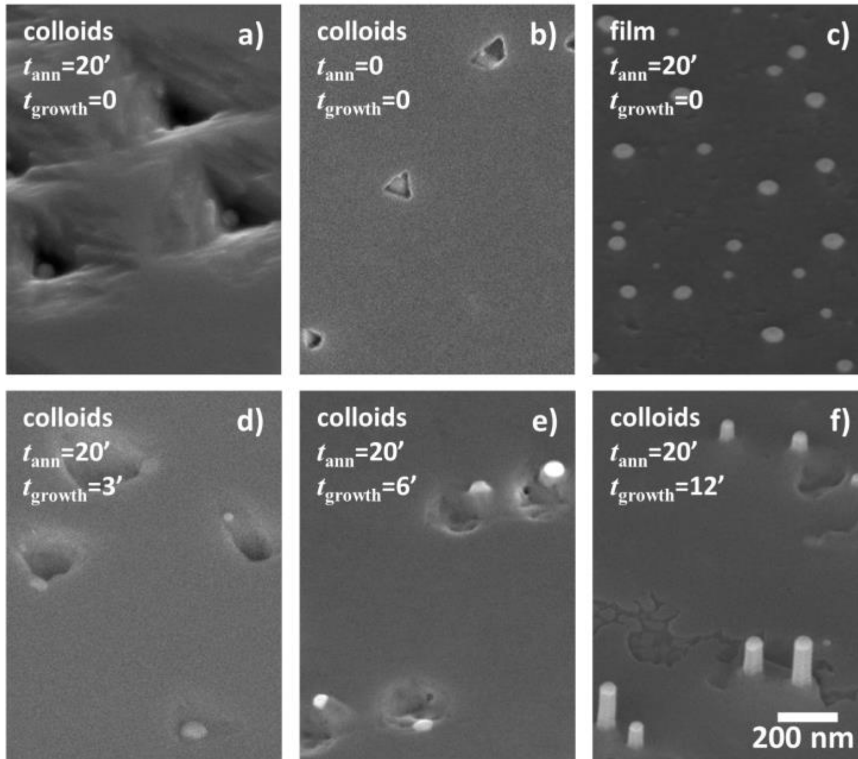

Figure 3.13. 45° tilted SEM image of (a) colloidal Au NPs after the standard annealing step (20 min at 500 °C under P_{TBAs} =1.0 Torr) compared to (b) colloidal Au NPs with just ramping the temperature up to 380 °C under P_{TBAs}=4.0 Torr, (c) the reference sample with thermally dewetted 0.5 nm Au film after the standard annealing step and (d-f) slow emerging of InAs NWs during the early stages of NW growth (3-12 min). Figure is adapted from Ref. [110].

The holes are formed as a result of interaction between Au colloidal NPs and the InAs substrate to form Au-In alloy accompanied by the evaporation of arsenic [27–29]. The nucleation delay leading to the wide and asymmetric LDs seen in Figure 3.12 should be due to a slow re-emerging of Au NPs from the holes when NW growth is started.

In fact, it is evident from the early stages of NW growth from 3 min to 12 min illustrated in Figure 3.13(d-f) that there is a significant delay in NW nucleation due to the the hole filling by InAs. No such holes were found on a substrate with 0.5 nm Au film subjected to identical annealing step as illustrated in Figure 3.13(c), and hence there was no delay in nucleation.

However, it is known that the decomposition of the InAs substrate depends on Au film thickness [29,111].We have observed the formation of holes in very thin layer of Au

film, i.e 0.01 nm and this tendency of formation of holes decreases as Au film thickness increases under identical annealing conditions as shown in Figure 3.14. The formation of holes on the substrate with low Au film thickness can also give broad and asymmetric length distributions of InAs NWs.

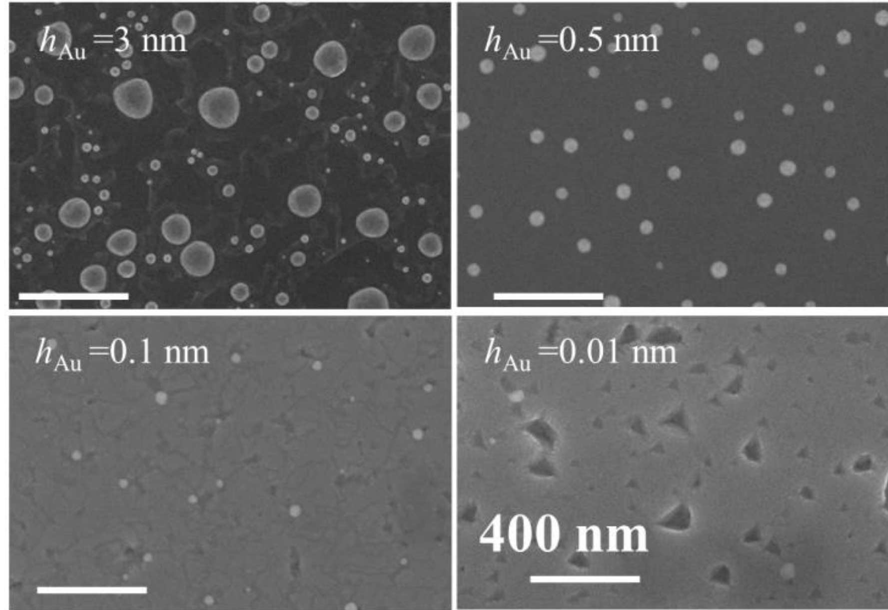

Figure 3.14. Plan-view SEM images of thermally dewetted Au NPs obtained after annealing Au film of different thickness (h_{Au}) under identical conditions. Smaller h_{Au} leads to hole formation.

The effect of hole formation by colloidal NPs was minimized by removing the annealing step by just ramping the temperature up to 380 °C under a high arsenic flux corresponding to P_{TBAs}=4.0 Torr which consequently reduced the size of the holes as shown in Figure 3.13(b). InAs NWs were then grown at the same temperature for t_{growth}=30, 60, 90 and 130 min. The measured LDs of these InAs NWs are shown in Figure 3.15. It is clearly seen that the NWs grown without the annealing step feature much narrower and symmetric LDs, in comparison to the LDs of InAs NWs grown under exactly identical conditions but with the standard annealing step as shown in Figure 3.12.The annealing step can be skipped only in the case of already formed metal NPs (i.e. using Au colloids as seeds) but not in the case of Au films as the annealing procedures are fundamental to dewet the Au film into NPs. As a consequence formation of holes in Au films of lower thickness cannot be avoided with this recipe.

In the case of colloids, a further delay may also be due to the use of poly-l-lysine adhesion layer which leaves nitrogen and carbon residues after annealing. It was previously determined that the nitrogen residues form a thin InN passivation layer on In

containing surfaces [112,113]. Moreover, it was speculated that the carbon residues surround the surface of the NPs and interfere its interaction with the precursors [89]. Such modifications of the surface properties of the substrate and NPs might infleunce the diffusivity, decomposition and incorporation of the precursors into the Au NPs resulting in longer incubation time [89,112,113]. In any case, the substrate preparation plays a crucial role for the NW length uniformity.

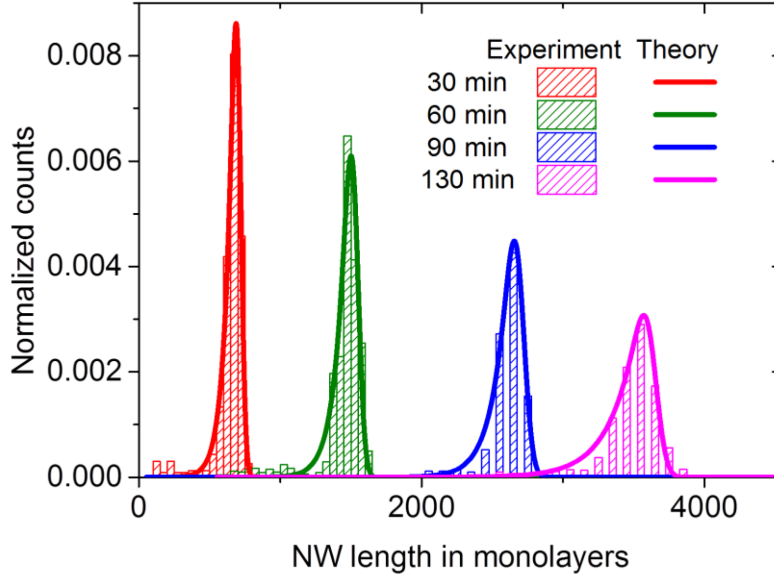

Figure 3.15. Normalized LDs (histograms) fitted by the model (lines) of Au-catalyzed InAs NWs grown from 40 nm Au colloids at 380 °C without the annealing step for t_{growth}= 30, 60, 90, and 130 min. Figure is adapted from Ref. [110].

3.3.2 Rate equation model

To understand the features of InAs NW LDs, we first consider the model for the NW elongation rates. The NWs are seeded by Au NPs deposited on the substrate surface at t =0. The In flux is denoted by *J*. For the very first NW monolayer emerging from the droplet, the vertical growth rate is given by $(dL_{NW}/dt)_{L=0} = \alpha J\Omega$. Here, Ω is the elementary volume per InAs pair in the solid state and α describes the NW nucleation probability. Measuring the NW length L in number of monolayers s (L = hs, with h as the height of a monolayer and s = 0, 1, 2 ...), we can rewrite the above equations for the growth rates as

$$\frac{ds}{dt} = K_s = -\alpha v_{In} \qquad 3.3.1$$

with v_{In} as the In vapor influx in monolayers per second.

The rate equations describing the LD of statistical ensemble of NWs are given as

$$\frac{dn_0}{dt} = -K_s n_0,$$

$$\frac{dn_1}{dt} = K_s n_0 - n_1,$$

$$\frac{dn_s}{dt} = n_{s-1} - n_s \quad s \geq 2 \qquad 3.3.2$$

The first equation means that the number of Au NPs decreases whenever the first NW monolayer has grown under it. The second equation means that the number of NWs with one ML decreases as another ML is added to it and increases if 1 ML is added to a Au NP. The third equation means that the number of NWs with *s* MLs decreases when one ML is added to it and increases if one ML is added to NWs with length *s*-1.

Consequently, in Au-catalyzed VLS growth with pre-existing Au catalyst NPs, the number of InAs NWs plus free NPs equals the number of initial Au NPs and hence the (LD) can be normalized to one. The distribution $f_s(\tau)$ over the NW lengths $s = L/h$ (measured in the units of the monolayer height h) at time $\tau = v_{In}t$ obeys the set of rate equations

$$\frac{df_0}{d\tau} = -\alpha f_0,$$

$$\frac{df_1}{d\tau} = \alpha f_0 - f_1,$$

$$\frac{df_s}{d\tau} = f_{s-1} - f_s \quad s \geq 2 \qquad 3.3.3$$

The model relies upon instantaneous axial growth rates without the nucleation antibunching [114–117] as the nucleation pulses require several conditions [114] that do not seem to hold in our experimental conditions as we cannot see any sub-Poissonian LDs. Second, we do not take into account surface diffusion of In adatoms since the measured length-radius dependences do not show any diffusion-induced inverse correlation [118] and the measured time dependences of the mean NW length are linear in most cases. Here and below, we also do not account for the Gibbs-Thomson effect that can decrease the axial growth rate of thin NWs or even suppress the NW nucleation from sufficiently small droplets [87,119,120]. According to Ref. [87], the Gibbs-Thomson effect usually becomes important for Au-NPs smaller than 40 nm in diameter. Therefore, this model implies a radius-independent axial growth rate of all NWs grown from Au NPs with diameter >40 nm. If a length-radius correlation is present, as in the diffusion-induced VLS growth, the resulting NW LDs will show additional size-dependent broadening as described in Ref.[121].

According to Ref. [114], Eqs. 3.3.3 with $\alpha = 1$ yield the Poissonian LD which rapidly tends to a symmetric Gaussian whose variance equals the mean length. Without the effect of nucleation antibunching [114–117], the Poissonian LD is the best case regarding the length uniformity [122].The NW nucleation probability α in Eqs. 3.3.3 accounts for the fact that nucleation of the very first monolayer of a NW may take a different time compared to the subsequent layers. The aim is to see how this effect influences the resulting LD.

Exact solutions to Eqs. 3.3.3 are given by

$$f_0(\tau) = e^{-\alpha\tau}, \qquad 3.3.4$$

$$f_{s+1}(\tau) = \frac{\alpha e^{-\alpha\tau}}{s!}\int_0^{\tau} dt e^{-(1-\alpha)t} t^s \ , s \geq 0 \qquad 3.3.5$$

When the NW nucleation is slow ($\alpha < 1$), the LD given by Eq. 3.3.5 can also be presented as

$$f_s(\tau) = \frac{\alpha e^{-\alpha\tau}}{(1-\alpha)^s}\gamma_s[(1-\alpha)\tau] \ ,$$

3.3.6

with

$$\gamma_s(x) = \frac{1}{(s-1)!}\int_0^{x} dt e^{-t} t^{s-1} \qquad 3.3.7$$

as the regularized incomplete gamma function.

In the continuum approximation for $s >> 1$, the rate equations are reduced to one Fokker-Planck kinetic equation

$$\frac{\partial f(s,\tau)}{\partial\tau} = -\frac{\partial f(s,\tau)}{\partial s} + \frac{1}{2}\frac{\partial^2 f(s,\tau)}{\partial s^2}. \qquad 3.3.8$$

This should be solved with the initial condition

$$f(s=0,\tau) = \alpha f_0(\tau) = \alpha e^{-\alpha\tau} \qquad 3.3.9$$

meaning that the LD at zero length equals the nucleation rate [123]. Green's function of Eq. 3.3.8 is given by the Gaussian with the mean length and variance τ [124]. When the droplet concentration is given by Eq. 3.3.4, the resulting LD is obtained by convoluting the Gaussian with this nucleation rate, as in Ref. [27]:

$$f(s,\tau) = \frac{\alpha}{2}e^{\alpha(s-\tau+\alpha\tau/2)} erfc\left(\frac{s+(\alpha-1)\tau}{\sqrt{2\tau}}\right). \qquad 3.3.10$$

Here,

$$erfc(x) = \frac{2}{\sqrt{\pi}} \int_x^\infty dt e^{-t^2} \qquad 3.3.11$$

denotes the regularized complimentary error function. This continuum representation can be used for both $\alpha < 1$ and $\alpha > 1$.

Figure 3.16 shows how the LDs broaden and acquire a pronounced asymmetry as the α value decreases from 0.99 (the Poissonian case) to 0.01.

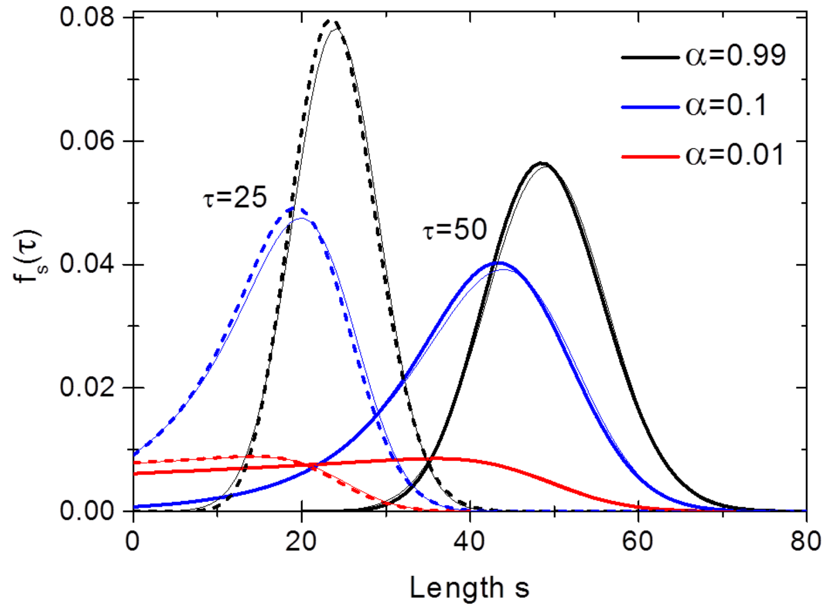

Figure 3.16. NW LDs after deposition of 25 (dotted lines) and 50 monolayers (solid lines) for different nucleation probabilities α . The LDs acquire broader and more asymmetrical shapes for smaller α . Thin lines show excellent fits of the continuum approximation given by Eq. 3.3.10 to the discrete LDs given by Eq. 3.3.5 already at the initial growth stage. Figure is adapted from Ref. [110].

This result can be well understood intuitively. Indeed, when the nucleation probability of the very first NW monolayer is much smaller than in the upper layers, the density of the catalyst droplets decreases very slowly with time and the nucleation process continues concomitantly with the VLS growth of the NWs that have emerged earlier. Consequently, NWs with shorter lengths will be more representative in the LDs and the left tail will be much longer than the right one. One may think that fast nucleation of NWs ($\alpha > 1$) would lead to a sharper LD with a shorter left tail. However, Figure 3.17 shows that this is not the case – a VLS system with $\alpha = 6$ forgets about a sharp nucleation step already after the deposition of 30 monolayers and the fluctuation-induced spreading renders the NW LDs to the Poissonian shape.

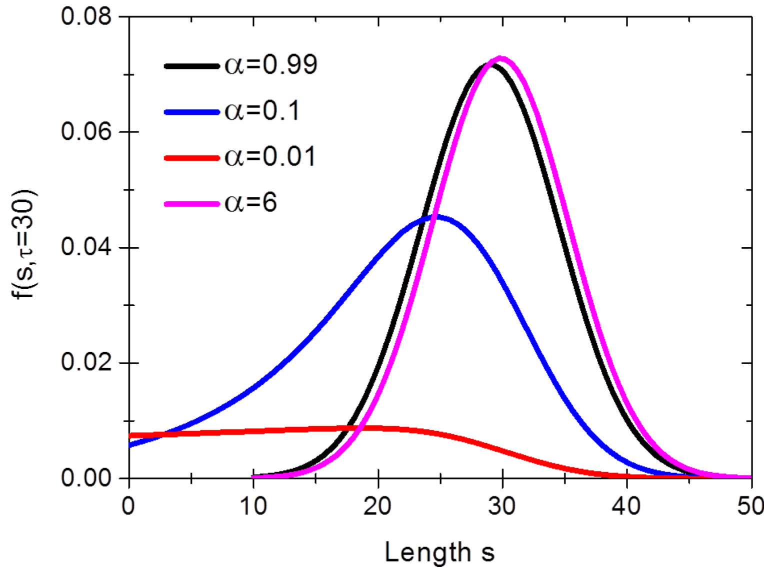

Figure 3.17. Continuum LDs after deposition of 30 monolayers showing broadening at $\alpha < 1$ and no narrowing at $\alpha > 1$. Fast NW nucleation yields only the Poissonian LDs $\alpha = 1$ due to the kinetic broadening. Figure is adapted from Ref. [110].

3.3.3 Modelling results and discussion

The LDs of NWs obtained from thermally dewetted Au NPs formed by annealing of a 0.5 nm thick Au film are fitted with the sharp Poissonian shape with α =1 (see Figure 3.11). This naturally leads to the conclusion about identical material transport rates and properties of the droplet at the very beginning and in the later stages of the VLS growth, not influenced, for example, by changing the droplet shape or barriers for the In adatom diffusion at the NW-substrate interface [125]. The pronounced asymmetrical and broad LDs of InAs NWs obtained from 40 nm Au colloids are best fitted with a very small α = 0.0025 for 60 min sample and 0.0013 for 130 min sample (see Figure 3.12). This corresponds to a significant delay in nucleation of the very first NW monolayer in this case (1000 times slower than in the upper layers). As mentioned above, this delay is due to Au NPs digging deep into the substrate during annealing (see Figure 3.13(a) and (d-f)). Removing the annealing step and just ramping to growth temperature to 380 °C under P_{TBAs}=4.0 Torr leads to a much better length uniformity because the NW nucleation becomes faster as the size of holes is reduced (see Figure 3.13(b)). This is supported by theoretical fits in Figure 3.15 obtained with α between 0.0053 and 0.017, i.e. of the order of magnitude larger than for the standard annealing step but two orders of magnitude lower than in the Poissonian case for thermally dewetted 0.5 nm thick Au film. This fully supports the initial assumption of the nucleation-related broadening of

the LDs.

3.3.4 Comparison of LDs between the two NP preparation methods

The NW nucleation probability α accounts for the NW length uniformity in the case of InAs NWs grown from thermally dewetted Au NPs and colloidal Au NPs in growth conditions where diffusion induced and Gibbs-Thompson length-diameter dependences are insignificant. A comparison of α obtained for InAs NWs grown thermally dewetted Au NPs (dotted line), colloids with (squares) and without (circles) the annealing step is shown as plot of α versus <*s*> in Figure 3.18.

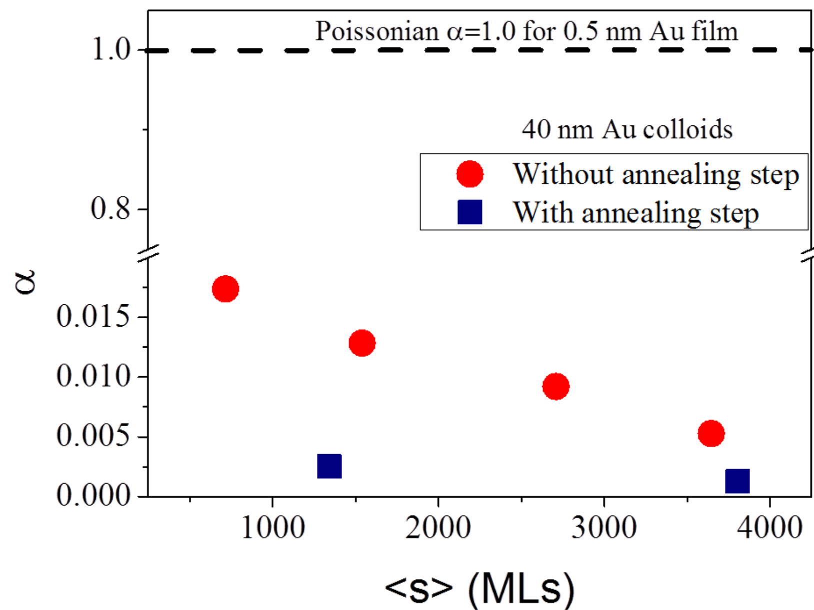

Figure 3.18. Comparison of α of InAs NWs grown from colloids as a function of NW length in monolayers <s>. The circles represent α obtained the LDs of InAs grown without the annealing step while squares represent α of LDs of InAs NWs grown with the annealing step.

InAs NWs grown from thermally dewetted Au NPs of 0.5 nm Au film are highly uniform with α =1 (dotted line) and features Poissonian distribution for all growth times. On the other hand, NWs grown from Au colloidal NPs in identical growth conditions have asymmetric and broad LDs due to nucleation delay of the first NW monolayer due to the formation of holes. Hence they have the lowest values of α (blue squares).The distribution can be improved by removing the annealing step that decreases the Au-InAs substrate decomposition. Even though α (red circles) is improved without the annealing step, it is still two orders of magnitude lower than the Poissonian distribution for which α =1 (dotted line).

3.4 Chapter summary

In this chapter, we have investigated the growth parameters to control diameter, density and length distribution of InAs NWs realized by annealing of Au thin films and colloidal Au NPs. By varying key parameters such as Au film thickness, colloid sizes, annealing temperature, and time significant understanding has been developed to control InAs NW diameter distribution. It is found that the average NW diameter and standard deviation of InAs NWs seeded from thermally dewetted Au NPs increases by increasing Au film thickness, annealing temperature, and annealing time. The relative standard deviation is in the range of ~20-40 %. In the case of colloids, annealing time and temperature do not have significant influence on the NW diameter.

We have also investigated the LDs of InAs NWs grown by Au-catalyzed VLS technique. Au NPs obtained by thermal dewetting of a 0.5 nm thick Au film shows Poissonian LD. Au colloidal NPs produce broader and asymmetric LDs that are influenced by slow nucleation of NWs on the surface. This is due to delay caused by the emergence of the Au colloidal NPs from holes formed on the substrate due to thermal decomposition. Nevertheless, the formation of holes can be reduced by removing the annealing step which leads to narrower LDs but still not Poissonian. The formation of holes that lead to broad and asymmetric distributions are not an exclusive property of colloids, but can show up also with particular film conditions (small Au film thickness, high annealing temperature, etc).

Along with NW diameter and length, density is another crucial parameter that needs a careful control. We found that colloids do not facilitate uniform growth on the sample surface while high uniformity is obtained with Au film. Therefore, by adjusting the different parameters and employing different preparation methods, it is possible to realize samples with the desired morphology and distribution.

4 Catalyst-free InAs NWs

This chapter provides an overview of the nucleation and growth mechanism of catalyst-free (CF) InAs NWs on Si (111) substrates. The first section of the chapter discusses about the growth protocol to obtain CF InAs NWs with high aspect ratio and its dependence on the various growth parameters. This section includes content from: U. P. Gomes, D. Ercolani, N. V. Sibirev, M. Gemmi, V. G. Dubrovskii, F. Beltram and L. Sorba, Nanotechnology, 26, 415604 (2015).
The second section of this chapter discusses about the density and yield control of CF InAs NWs on Si (111) substrates. This section includes content from: U. P. Gomes, D. Ercolani, V. Zannier, S. Battiato, E. Ubyivovk, V. Mikhailovskii, Y. Murata, S. Heun, F. Beltram and L. Sorba, submitted to Nanotechnology (2016).

4.1 CF InAs NW growth

4.1.1 Two-stage NW growth protocol

The growth process employed for growing InAs NWs on Si (111) substrates involves a high temperature annealing under TBAs flux followed by a two-temperature sequence. The latter consists of a low-temperature (LT) nucleation and a high-temperature (HT) growth steps followed by a rapid cool down under TBAs flux to terminate the growth. Figure 4.1 shows the growth sequence along with the corresponding SEM images on different stages of growth, marked by the coloured dots in the temperature graph of Figure 4.1(a). Sputtered Si (111) substrates using SiO_2 sputtering was obtained using sputter bias of 520 V and sputter time of 60 s (see section 2.2). Further details of the silicon substrate preparation will be provided in section 4.2. After etching the oxide in

BOE for 2 min, rinsing in deionized water and blowing dry by nitrogen, the hydrogen-terminated Si (111) substrates were annealed at 790 °C under a TBAs line pressure of 1.00 Torr for 15 min. After annealing, the temperature was ramped down to 390 °C. All standard samples were then grown with a 10 min LT nucleation step (P_{TMIn}=0.30 Torr, P_{TBAs}= 3.00 Torr. 390 °C), 10 min ramp (P_{TMIn}=0.30 Torr, P_{TBAs}=3.00 Torr) to the HT growth step (P_{TMIn}=0.20 Torr, P_{TBAs}=3.00 Torr) continuing for 60 min at growth temperature T_{growth}=520 °C.

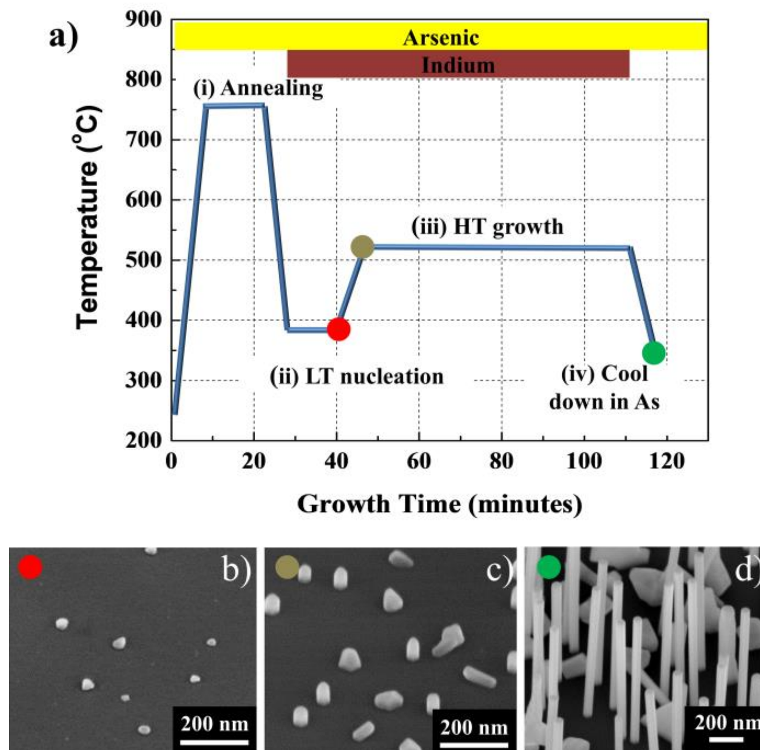

Figure 4.1. (a) Schematic of two stage growth protocol for growing InAs NWs on Si (111) substrate including: (i) annealing in P_{TBAs}=1.00 Torr, (ii) low temperature (LT) nucleation step, (iii) high temperature (HT) growth step, and (iv) cool down in TBAs flux. 45° tilted SEM images corresponding to the end of the LT nucleation step (b), the beginning of the HT growth step (c), and the end of growth (d). Figures are adapted from Ref.[126].

Figure 4.1(b) shows that at the end of the LT step the silicon surface appears decorated by InAs crystals with a typical size of about 10 nm. At the end of the ramp between the LT nucleation and the HT growth steps (Figure 4.1(c)) some crystals start elongating in the direction orthogonal to the silicon surface. At the end of the HT step (Figure 4.1(d)) two different types of crystals are present: highly anisotropic NWs with hexagonal cross section and along axis normal to the silicon surface and large isotropic islands having the aspect ratio of the order of one. Each step of the two stage growth protocol is crucial

for NW growth. Therefore, in the following, we consider the role of each step in details. The annealing procedure is essential for removing the weakly-bound organic contaminants and transforming the silicon surface reconstruction from Si (1×1)-H to Si (1×1)-As [69]. The As-passivated substrate is an ideal surface for growing polar semiconductor on non-polar substrate and was successfully implemented for 2D and 1D epitaxial growth of III-Vs on Si (111) [69,127].The annealing step also determines the density of defects on the sputtered silicon surface which controls the nucleation of islands and NWs as will be described later in section 4.2.

The LT step governs the NW nucleation phenomenon and prevents thermal desorption of In from Si (111) substrates. Figure 4.2 shows the results of 20 min constant temperature growth runs with P_{TMIn}=0.30 Torr and P_{TBAs}=3.00 Torr, at three different temperatures.

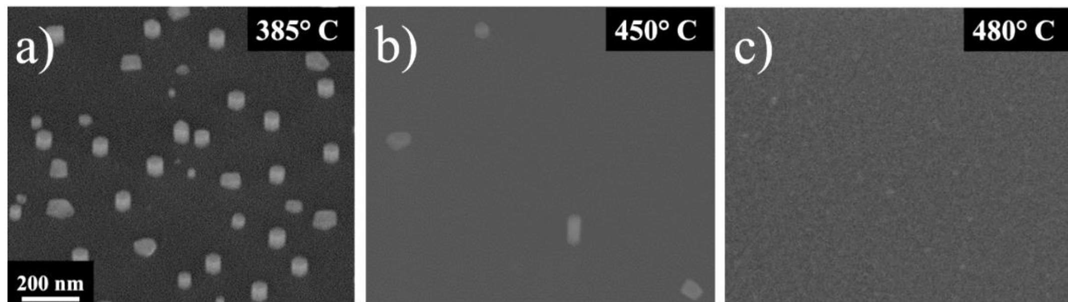

Figure 4.2. 45° tilted SEM images of InAs NWs grown on Si (111) with a constant temperature of 385 °C (a), 450 °C (b) and 480 °C (c). Samples were grown for 20 min with P_{TBAs} and P_{TMIn} of 0.30 and 3.00 Torr, respectively. Figures are adapted from Ref. [126].

At the lowest temperature of 385 °C, we observed the formation of a high density ensemble of InAs crystals with the aspect ratio of the order of one (Figure 4.2(a)). At the intermediate temperature of 450 °C, the island density was strongly reduced (Figure 4.2(b)). Further increase of the growth temperature to 480 °C (Figure 4.2(c)) resulted in a clean silicon surface with no nucleation of InAs islands. It must be noted that this last temperature is still lower than that used for the HT step in the two-temperature growth (see Figure 4.1(a)).

Figure 4.3(a) shows selected 45° tilted SEM micrographs of NWs taken from samples grown from 15, 30, and 45 min, respectively at 390 °C. Figure 4.3(b) shows the plot of NW radius as a function of the low temperature growth time, t_{growth}. The inset shows the plot of NW length as a function of the low temperature growth time, t_{growth}.

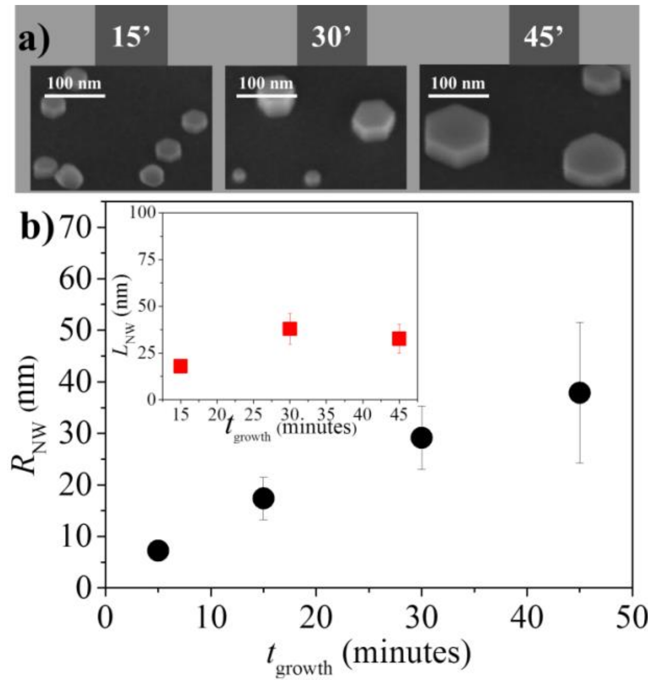

Figure 4.3. (a) Selected 45° tilted SEM images of InAs NWs gown with different low temperature growth times. (b) Plot of NW radius vs growth time. The inset is a plot of NW length vs growth time.

From Figure 4.3(a) and (b) it is conclusive that as time progress, the NWs grow significantly in radial directions but the axial growth is negligible. This is due to the low growth temperature (390 °C) employed to promote nucleation. In summary, the LT step promotes NW nucleation but owing to the low temperature the NWs grow radially while the axial growth is negligible.

As for the nucleation mechanism of InAs islands, it is driven by the lattice mismatch between InAs and Si and it proceeds via the Volmer-Weber growth mode. Three-dimensional islands are formed because they have a lower elastic energy compared to a 2D layer and may undergo several shape transitions to minimize their free energy before NWs form, as in the case of GaN islands on lattice-mismatched AlN interlayer on Si(111) [49]. Plastic relaxation via the formation of misfit dislocation at the island-substrate interface [49] is not excluded, and after that the transformation to anisotropic growth may be associated with a lower surface energy of hexahedral elongated NWs [128].

Having explained the LT nucleation mechanism, at this point it is important to understand how InAs NWs can grow with high aspect ratio. As mentioned above, the LT step promotes NW nucleation but the HT step is required to start anisotropic growth where the axial elongation of NWs dominates over their radial extension, similarly to

the case of self-induced GaN NWs on Si substrates [49,51,128,129]. Since, the axial growth of InAs NWs necessarily requires the HT growth step, the kinetic factors strongly influence the surface morphology of InAs NWs. Some considerations on the highly anisotropic growth leading to the CF InAs NW formation during the HT step is explained below.

First, under the As-rich conditions employed in CF InAs growth experiments, the InAs (111) surface of the NW top facet is likely to exhibit 2×2 reconstruction with As trimers on top of the As layer [27,130,131]. The nucleation barrier to form a critical 2D nucleus on the NW top (ΔG_*) is proportional to h, the height of the nucleus: $\Delta G_* \propto h$ [132,133]. When modelling the VLS growth of NWs the nucleus height is usually considered as the height of a bilayer [132,133]. On the contrary, in the case of CF InAs NWs, the arsenic part of the bilayer should form almost instantly and thus the nucleation requires the completion of only the In layer with an h value that is approximately half that of the complete bilayer. This reduces the nucleation barrier to approximately one half of its value on the side facets. Due to a steep exponential dependence of the nucleation rate (and the resulting growth rate V) on the nucleation barrier [133], $V \propto \exp(-\Delta G_*/k_B T)$, the axial growth rate will be an order of magnitude higher than the radial one. This simple argument applies to the nucleation-mediated growth rate. On the other hand, a much faster growth on the NW top with respect to the side facets requires efficient diffusion transport of In adatoms to the top. Indium will migrate to the top only if the chemical potential at the tip is lower than at the NW sidewalls [52]. This property is ensured by the fact that the top facet is a more efficient sink of group III adatoms relative to the side facets and therefore the group III concentration on the NW top is the lowest as was observed for catalyst free GaN NWs [51] or selective area III-V NWs [134]. Under As-rich conditions, CF growth of InAs NWs is expected to be limited by surface diffusion of In, similarly to the case of self-induced GaN NWs under high nitrogen flux [51].

4.1.2 Length-radius dependence

As discussed in the previous section, the anisotropic CF growth of InAs NWs necessarily requires a positive diffusion flux of In adatoms from the NW sidewalls to the top. Diffusion-induced growth of NWs with a time-independent radius is characterized by a decreasing length-radius [$L_{NW}(R_{NW})$] correlation at a given time [118,135]. For a hexahedral NW with a flat top facet (see schematic in Figure 4.4), the

simplest equation for the axial growth rate, dL_{NW}/dt, can be expressed as [135]

$$\frac{dL_{NW}}{dt} = W\left[1 + \frac{3\sqrt{3}}{16}\frac{\lambda \tan\alpha}{R_{NW}}\right] \qquad 4.1.1$$

Here, the first term describes the direct impingement of TMIn beam, with W (($\phi_{In}\cos\alpha$) the effective deposition rate of In accounting for the incorporation efficiency of TMIn that can depend on both P_{TBAs} and P_{TMIn}. The second term accounts for the diffusion flux of In adatoms from the NW sidewalls to the top, with λ the effective diffusion length of In and $\alpha = 38^o$ the incident angle of TMIn beam. λ accounts for the pyrolysis efficiency of TMIn at the sidewalls.

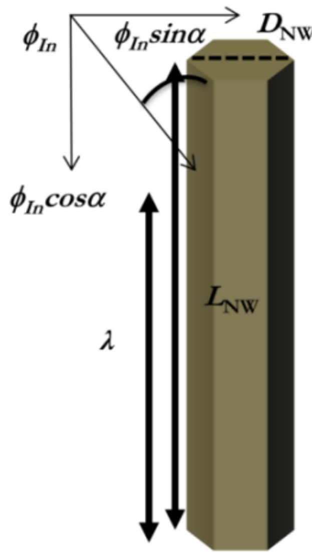

Figure 4.4. Schematic description of a CF InAs NW illustrating the geometrical parameters of NW and CBE chamber geometry used in the growth model.

Now, two specific features of self-induced mechanism of CF InAs NW formation is introduced into the standard scenario of the diffusion-induced growth. First, CF InAs NWs not only grow axially but also extend radially. The measured time dependence of the NW diameters is well fit by the linear law $R_{NW} = R_0 + vt$, with R_0 initial radius and v the radial growth rate which depends on the V/III flow ratio $F=P_{TBAs}/P_{TMIn}$. The linear fit of the data obtained for a time series of samples with F=15 is shown in Figure 4.5 and yields $v = 0.3$ nm/min. The zero growth time data point corresponds to the NWs formed in the LT and ramp step. Each point is the average of many NWs measured on one sample.

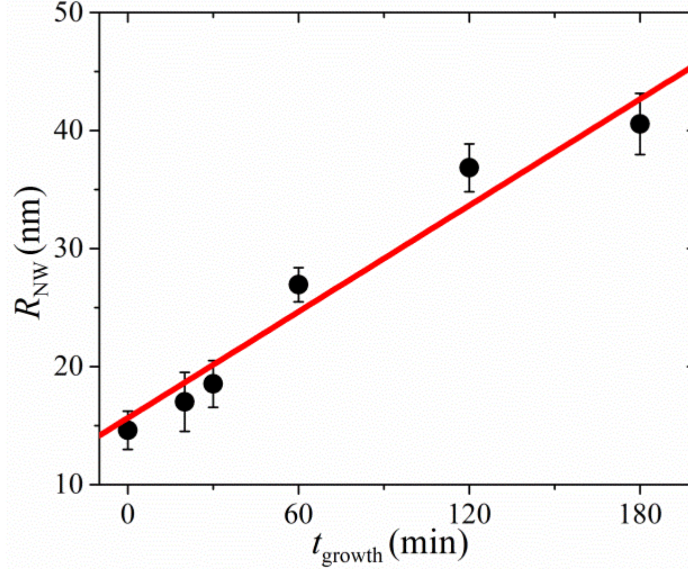

Figure 4.5. Growth time dependence of the average radius of InAs NWs grown at P_{TBAs}= 3.00 Torr, P_{TMIn}=0.20 Torr, and F=15 for different growth times in the HT step (symbols), with its linear fit (line). Figure is adapted from Ref. [126].

Second, self-induced NWs grow from pre-existing NWs that are formed after the LT nucleation stage and ramp (see Figure 4.1(c)). These pre-existing NWs also have some length-radius dependence at $t = 0$. L_{NW}-R_{NW} data of pre-existing NWs are plotted in Figure 4.6 as blue triangles and are fitted by a linear dependence: $H(R_0) = H_0 - H_1 \cdot R_0$, with $H_0 = 363$ nm and $H_1 = 8.23$. Considering an individual NW with a length L_{NW} and a radius R_{NW} measured after a HT growth time t_{growth}, and combining the two linear relations above, it is possible to derive the length $H(R_0)$ that one such NW has at the end of the LT stage: $H(R_0) = H(R_{NW} - vt) = H_0 - H_1(R_{NW} - vt)$. This, in turn, allows us to integrate Eq. 4.1.1 for each individual NW, obtaining the NW length (including the initial island height) in the form

$$L_{NW} = Wt + \frac{W}{v}\frac{3\sqrt{3}}{8}\lambda \tan\alpha \ln\left(\frac{R_{NW}}{R_0}\right) + H(R_0) \qquad 4.1.2$$

Figure 4.6 shows good fits of the measured length-radius correlations after different growth times, obtained from Eq. 4.1.2 and with $\lambda \approx$ 400 nm and $W \approx 1.6$ nm/min; all other parameters come from direct measurements on the SEM images of the samples. In spite, of scattering of the experimental data, the theoretical fits show a qualitative behaviour of the NW length and radius correlation as a function of growth time.

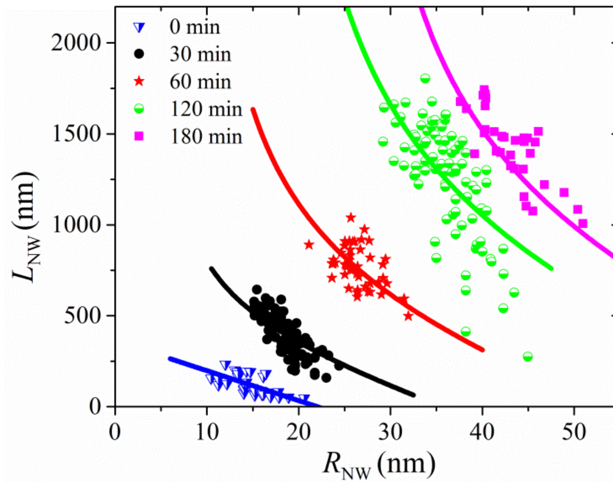

Figure 4.6. Measured length-radius correlations of InAs NWs grown at P_{TBAs}= 3.00 Torr, P_{TMIn}= 0.20 Torr (F=15), for different growth times in the HT step (symbols), fitted by Eq. 4.1.2 (lines). The "0 min" data (blue triangles) correspond to the InAs islands formed after the LT step plus ramp. Figure is adapted from Ref. [126].

4.1.3 Influence of MO precursors

In order to understand the influence of MO flow rates on the effective deposition rate W, we investigated the total volume of NWs, Ω (excluding the volume of the islands formed after the LT step plus ramp) versus P_{TBAs} and P_{TMIn}.

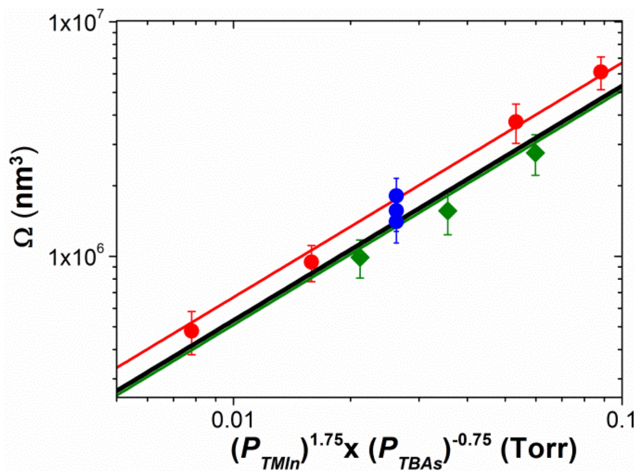

Figure 4.7. Log-Log plot of NW volume Ω versus $P_{TMIn}^{1.75}/P_{TBAs}^{0.75}$ for different sample series grown with a fixed P_{TBAs} =3.00 Torr and different P_{TMIn} (red circles), fixed P_{TMIn} = 0.20 Torr and different P_{TBAs} =3.00 (green diamonds), and in standard growth conditions (P_{TBAs} =3.00 and P_{TMIn} = 0.20, blue symbols). The coloured lines are linear fits of the two series while the black one is the linear fit of all data. Figure is adapted from Ref. [126].

It turns out that this dependence is well fitted by power-law dependence $\Omega \propto P_{TMIn}^{1.75} / P_{TBAs}^{0.75} = P_{TMIn} F^{-3/4}$ for a variety of samples, as shown in Figure 4.7. In the As-rich conditions used for the growth, the NW volume should be proportional to the available In: $\Omega \propto \chi P_{\mathrm{TMIn}}$. Thus χ, the pyrolysis efficiency of TMIn, scales with the V/III flow ratio approximately as $\chi \propto F^{-3/4}$. Although a detailed understanding of this dependence is missing, a decrease of the effective deposition rate with increasing V/III flow ratio was previously reported for Au-catalyzed InP NWs [136] and GaAs NWs [55]. This effect could be explained by a reduced adsorption of In which is suppressed by an increasing density of As trimers [130].

In the absence of an In-rich droplet (which would serve as a reservoir of indium), the axial growth rate on the NW top facet is expected to be proportional to $(\chi P_{\mathrm{TMIn}} P_{\mathrm{TBAs}})^{1/2}$ so that at a fixed χ, an increase of both fluxes by a factor 2 leads to a twice as fast growth rate. These simple considerations yield to $W=A\ (P_{\mathrm{TMIn}}/P_{\mathrm{TBAs}})^{3/4}\ (P_{\mathrm{TMIn}}\ P_{\mathrm{TBAs}})^{1/2}$, where A is a uniform normalization factor. Combining this with Eq. 4.1.2, we obtain the following model equation for the average NW length $\langle L \rangle$ as a function of the growth time, MO line pressures, and the average NW radius $\langle R \rangle$:

$$\langle L \rangle = A\left(\frac{P_{TMIn}}{P_{TBAs}}\right)^{\frac{3}{4}} \left(P_{TMIn} P_{TBAs}\right)^{\frac{1}{2}} \left[t + \frac{3\sqrt{3}}{8} \frac{\lambda \tan\alpha}{v} \ln\left(\frac{\langle R \rangle}{\langle R_0 \rangle}\right)\right] + \langle H(R_0) \rangle \qquad 4.1.3$$

Here, $\langle R_0 \rangle$ and $\langle H(R_0) \rangle$ are the average radius and length of the initial InAs islands, respectively. Since v, $\langle R_0 \rangle$, and $\langle H(R_0) \rangle$ can be directly derived for each sample as shown before, Eq. 4.1.3 contains only two adjustable parameters: the effective diffusion length of In adatoms, λ and the normalization constant A. Figure 4.8 shows very good consistency between the measured data and calculated $\langle L \rangle$ for the NWs grown in different conditions in the HT stage. The computed $\langle L \rangle$ values in Figure 4.8 were all obtained with the same values of the fitting parameters λ=400 nm nm and A=18 nm $\times$ Torr^{-1} $\times$ min^{-1}.

Although λ in principle has a non-trivial dependence on precursor fluxes and ratio, we have decided to use the constant value determined from the fit with Eq. 4.1.3 of the growth time series of Figure 4.8. This leaves only one fitting parameter, A. The overall linearity of the heterogeneous data shown in Figure 4.8, considered the single free parameter for the fit, confirms the soundness of the assumptions and the validity of the model.

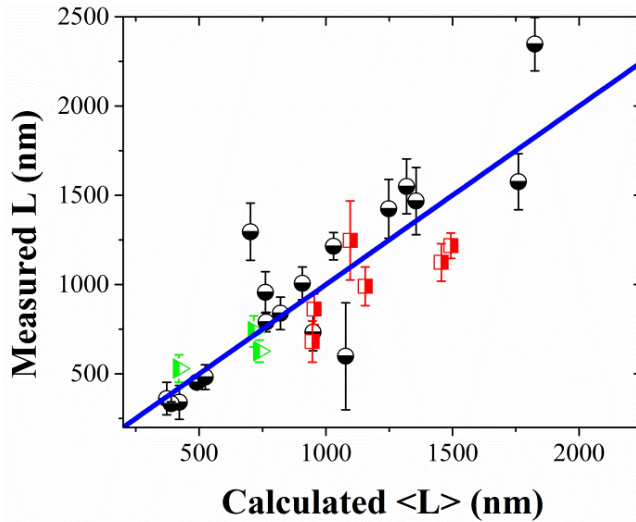

Figure 4.8. Comparison of measured and calculated lengths of InAs NWs grown with F=15 (black circles), F <15 (red squares) and F>15 (green triangles) during the HT stage. The calculated lengths $\langle L \rangle$ have been obtained from experimental values through Eq. 4.1.3. Figure is adapted from Ref. [126].

4.1.4 Influence of growth temperature

Figure 4.9(a) shows the growth-temperature dependence of InAs NW length and radius, with the typical SEM images presented in panels b-d. All these NWs were grown with the same LT nucleation step (P_{TBAs} =3.00 Torr, P_{TMIn}=0.30 Torr, and at 390 °C) while in the HT stage the growth temperatures were varied from T_{growth}=480 °C to 540 °C under P_{TBAs} of 3.00 Torr and P_{TMIn} of 0.20 Torr, with 60 min growth time.

The NW length first increases with increasing growth temperature, due to an enhanced thermally-activated diffusion of In adatoms at higher temperatures [40]. When the diffusion length increases, the sidewall incorporation of In adatoms becomes less pronounced and consequently the NW radius decreases [40]. At 520 °C, the NW length reaches its maximum of (955±116) nm while the radius reaches the minimum at (49±4) nm, yielding the highest aspect ratio observed (about 20). Decrease of the NW length at temperatures higher than 520 °C and a corresponding increase of the radius are likely caused by the enhanced thermal decomposition of InAs along the <111> direction, as shown by In desorption experiments [41]. When the adatom sink at the NW top decreases its efficiency due to this thermal decomposition, the diffusion flux to the top decreases and thus the NW radius increases [25].

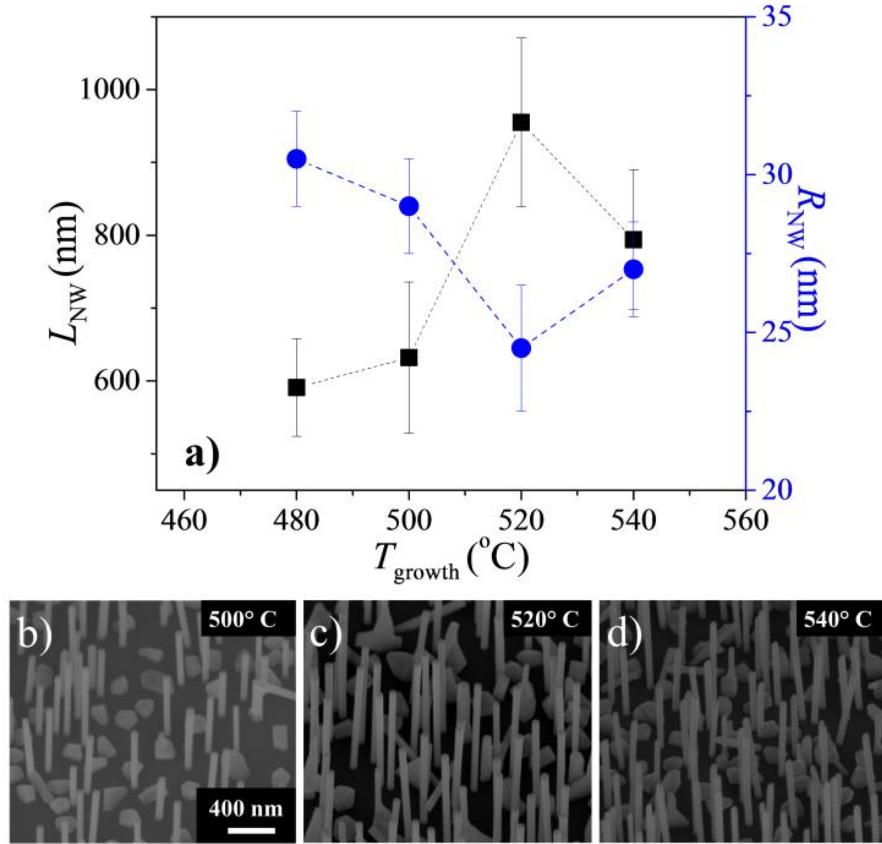

Figure 4.9. (a) Plot of InAs NW length and radius versus the growth temperature during the HT step. 45° tilted SEM images show the samples grown at (b) 500 °C, (c) 520 °C and (d) 540 °C. Figures are adapted from Ref. [126].

4.1.5 Aspect ratio control

With the understanding of the NW morphology on the growth temperature, we have systematized the InAs NW aspect ratios as a function of the MO line pressures. The overall results are summarized in the map of Figure 4.10(a) for samples grown 60 min at 520 °C in the HT step. The diameter of the islands formed in the LT step for all the growths shown on the map is 28±4 nm. Based on this map, we are able to carefully modulate the InAs NW aspect ratio by changing the MO line pressures during the HT growth steps. In particular, Figure 4.10(b) shows the SEM images of the InAs NWs with the highest aspect ratio of 20, obtained with P_{TMIn}=0.20 Torr and P_{TBAs}=3.00 Torr, (F=15), while Figure 4.10(c) displays the InAs NWs with the lowest aspect ratio of 8.5, obtained with P_{TMIn} =0.20 Torr and P_{TBAs} =1.00 Torr (F=5). InAs NWs with any desired aspect ratio between these values can be obtained by the appropriate choice of the MO line pressures.

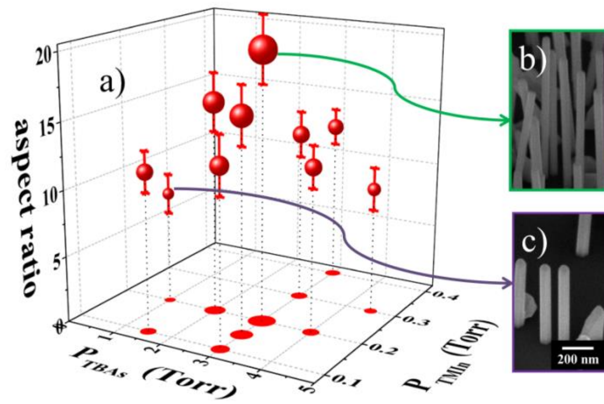

Figure 4.10 (a) Map of InAs NW aspect ratio versus MO line pressures. (b) and (c) are 45° tilted SEM images of the NWs grown with *F*=15 and 5 respectively, resulting in the extreme aspect ratio. Figures are adapted from Ref. [126].

4.1.6 Crystal structure

TEM analysis of InAs NWs confirms non-tapered shape and reveals a defective crystal structure. The bright-field image in $[2\bar{1}\bar{1}0]_{WZ}$ (or $[110]_{ZB}$) zone axis shown in Figure 4.11 (b) display a sequence of bright and dark stripes characteristic of a disordered stacking.

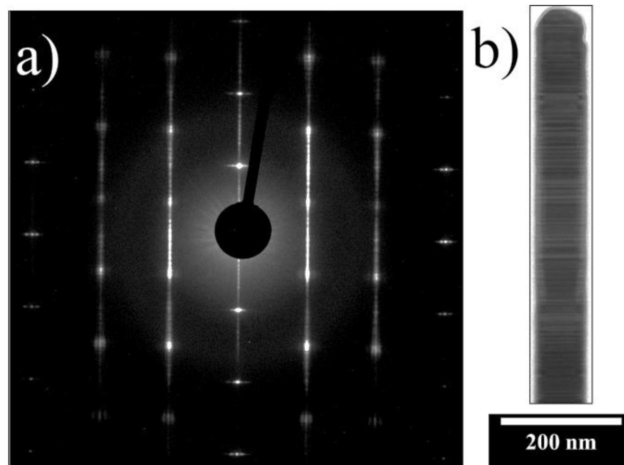

Figure 4.11. (a) Electron diffraction pattern and (b) bright field TEM image in the $[2\bar{1}\bar{1}0]_{WZ}$ (or $[110]_{ZB}$) zone axis of an InAs NW on Si (111) showing disordered stacking sequence. Figures are adapted from Ref. [126].

The WZ and ZB index in the zone axis notation indicates a hexagonal WZ or a cubic ZB bravais lattice. The corresponding diffraction pattern (Figure 4.11(a)) exhibits a strong streaking parallel to $[0001]_{WZ}$ (or $[110]_{ZB}$) reciprocal direction, which does not allow the determination of any dominant polytype between the WZ and ZB structures.

Thus, CF InAs NWs can be considered as a disordered stacking sequence of hexagonal InAs closed-packed layers where the ordered ZB and WZ domains do not exceed few nanometers in length.

4.2 Density and yield control of CF InAs NWs

In this section, we will discuss the strategies to control the density and yield of InAs NWs. The nucleation of InAs NWs and islands is attributed to the surface defects formed on the silicon substrate due to sputtering. The formation of these surface defects can be controlled by the sputtering parameters, which allows to obtain samples with a wide range of NW densities. Moreover, annealing and growth temperature can be optimized to reduce the relative density of the parasitic islands and to realize samples with high NW yield.

4.2.1 NW growth process

In order to investigate the density and yield of CF InAs NWs, we employ a growth protocol depicted in Figure 4.12. The growth protocol consists of only the LT stage instead of the two-step growth protocol as was described in section 4.1. This is because the LT stage determines the nucleation of NWs and islands. By controlling the nucleation of NWs and islands at the LT stage, it is possible to control their density and yield.

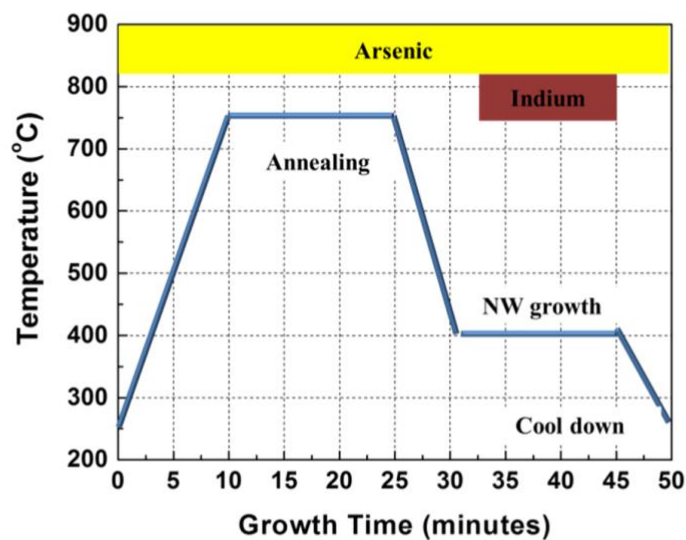

Figure 4.12. Schematic of the growth protocol consisting on an annealing step and low temperature NW growth step.

In particular, the growth process involved a high temperature annealing (T_{ann}) under As flux of (P_{TBAs}=1.0 Torr) for 15 min. After the annealing step, the temperature was ramped down to the growth temperature T_{growth} and InAs growth was initiated for a growth time of t_{growth} by introducing In and As fluxes at MO line pressures of P_{TBAs}=3.0 Torr and P_{TMIn} =0.30 Torr. The NW growth was terminated by cooling down the samples in As flux.

Figure 4.13 shows plan-view SEM micrographs of InAs NWs grown on non-sputtered Si (111) and on sputtered Si (111) substrates using two different sputtering procedures as discussed in chapter 2: RF magnetron SiO_2 sputtering and ICP argon sputtering. The sputtered surface using SiO_2 sputtering was obtained using sputter bias ($V_{sputter}$) of 520 V and sputter time ($t_{sputter}$) of 60 s. $V_{sputter}$ and $t_{sputter}$ was 35 V and 600 s respectively for ICP argon sputtering.

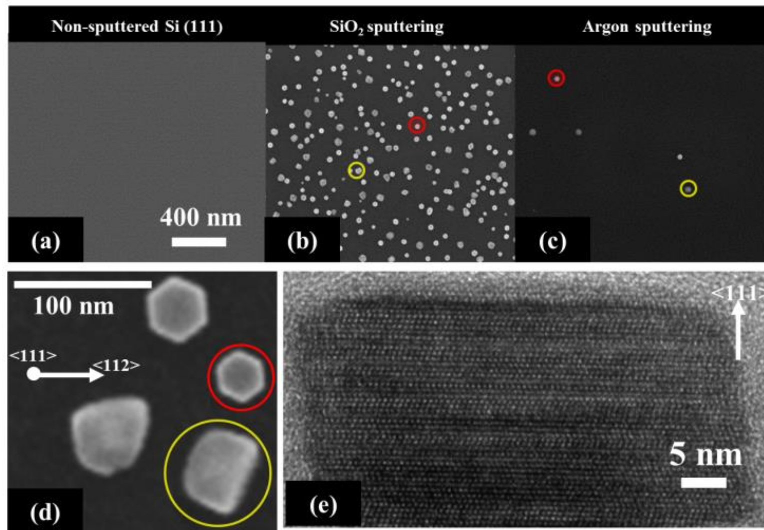

Figure 4.13. Plan-view SEM micrographs of InAs crystals grown under identical conditions on (a) non-sputtered, (b) SiO_2 sputtered and (c) ICP argon sputtered silicon substrate. The coloured markers are used to identify islands (yellow) and NWs (red) shown in figure (d). (e) High-resolution TEM image of InAs crystal taken from the sample shown in (b). Figures are adapted from Ref.[85].

It is evident from the SEM micrographs in Figure 4.13(a-c) that InAs crystals nucleated only on the sputtered Si (111) surfaces. Extensive investigation of non-sputtered samples grown with a wide variety of growth parameters never revealed NWs or islands. The enhancement of nucleation on sputtered Si (111) surfaces in comparison to that of non-sputtered Si (111) surface is likely due to the formation of surface defects by sputtering [137]. Although a large number of processes occur during sputtering, it is

well established that bombarding the surface with energetic atoms leads to the formation of surface defects, which serve as preferential nucleation sites [137–139]. In fact, the role of surface defects as nucleation sites in CF NW growth has been already established where it was found that the defects ease the formation of critical nuclei and enhance the nucleation rate [46,140]. It is also known that sputtering by particles within specific range of energies can transform a crystalline silicon into an amorphous state or even etch the silicon substrate when the density of defects become very high [141]. No NW growth occurs on silicon substrate that gets etched due to sputtering. Hence, the energy of the sputtered particles needs to be controlled to a restricted parameter space such that surface defects can be created without etching or amorphizing the substrate. The amorphous silicon may convert to the desired crystalline phase by annealing at temperature >800 °C, however, the maximum annealing temperature T_{ann}=790 °C used in our experiments is lower than this temperature.

The InAs crystals shown in Figure 4.13(b) and (c) consist of NWs (red circles) and islands (yellow circles). Therefore, the InAs crystal density (*N*) is the sum of InAs NW and island density. Figure 4.13(d) shows a magnified view of InAs NWs and islands. The NWs have a hexagonal cross-section and grow along the <111> direction with side facets oriented parallel to {112} silicon planes while the islands appear to have random crystalline facets. For a given sample, the yield (*Y*) of NWs is determined as the ratio of NW density to the InAs crystal density (NWs and islands) which is ~50% for samples shown in Figure 4.13(b) and (c). Figure 4.13(e) is a cross-sectional HRTEM image of a NW taken from sample shown in Figure 4.13(c). The micrograph is taken in the Si <110> zone axis with the NW growing along a vertical [111] axis. At this early stage, and for the chosen growth parameters, the NW has aspect ratio less than one, displaying vertical {112} sidewalls. It is growing epitaxially on the substrate, with horizontal InAs (111) planes and a flat top facet. Already at this early stage of growth, the crystal structure has high density of stacking faults, showing intermixing of WZ and ZB layers. Overall, the morphology is equivalent to longer InAs NWs as shown in Figure 4.11.

4.2.2 Dependence of *N* and *Y* on annealing conditions

In Figure 4.14(a) the dependence of *N* and in Figure 4.14(b) the dependence of *Y* for InAs NWs is plotted as a function of T_{ann} grown on a SiO_2 sputtered silicon substrate ($V_{sputter}$ =520 V and $t_{sputter}$=60 s). Figure 4.14(c)-(e) correspond to selected plan-view SEM micrographs of samples grown at different T_{ann}. The annealing time was kept fixed

at 15 min and conducted in a background of As flux corresponding to P_{TBAs} of 1.0 Torr. Growth was done at T_{growth}=400 °C for 15 min.

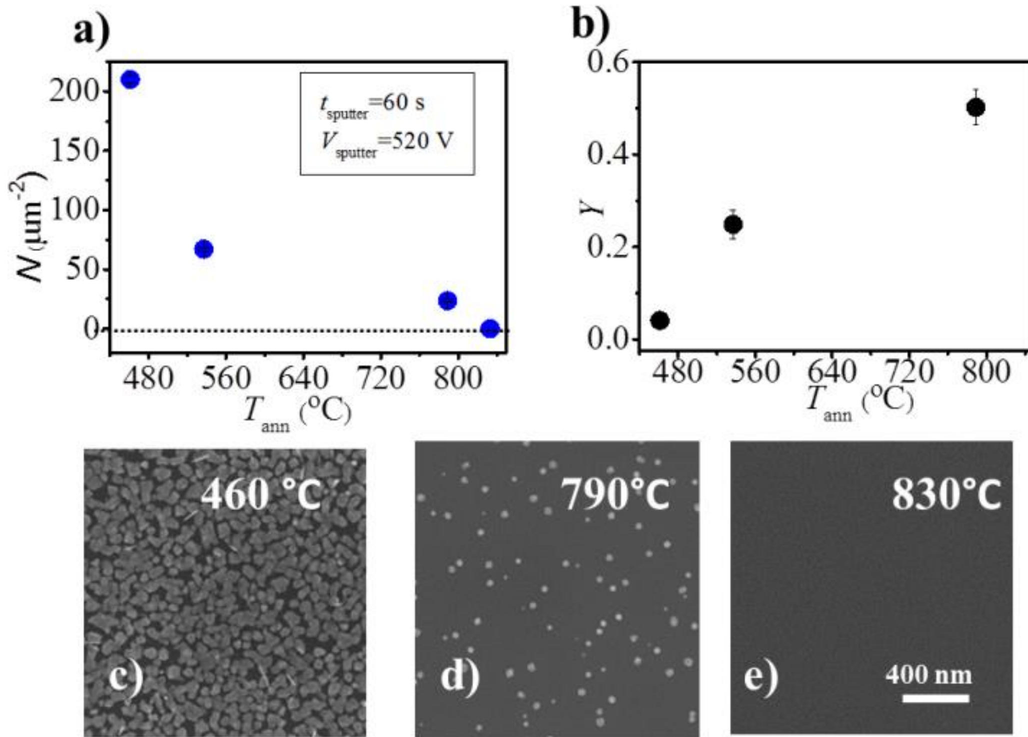

Figure 4.14. Correlation between (a) InAs crystal density and (b) yield with T_{ann}. (c)-(e) selected SEM micrographs of the samples annealed at 460, 790 and 830°C, respectively. Figures are adapted from Ref.[85].

Figure 4.14(a) demonstrates appreciable reduction of InAs crystal density with an increase in the annealing temperature. At the lowest T_{ann} of 450 °C, the InAs crystal density is the highest (~210 crystals/μm^2) while at the highest T_{ann} of 830 °C, the InAs crystals are completely absent. The reduction in the InAs crystal density observed due to annealing suggests that the surface defects annihilate as T_{ann} is increased and at highest T_{ann} of 830 °C the sputtered silicon surface with lattice disorder regenerates into an ordered silicon surface, comparable to a non-sputtered silicon surface (see Figure 4.13(a)). Figure 4.14(b) shows that the yield of NWs increases with T_{ann} and at T_{ann} =790 °C, the yield of NWs is maximum (~ 50%) as more NWs nucleate on the surface in comparison to islands. At, higher T_{ann} > 790 °C there was no nucleation of NWs and islands due to ordering of the surface and hence Y is undefined.

This is because the annealing and cooling cycles under UHV conditions not only determines the defect density but also surface reconstruction [142,143]. It is known that different surface reconstructions have different surface energies that determine the

polarity and morphology of InAs crystals [144,145]. We expect the annealing process at T_{ann} =790 °C for 15 min and subsequent cool down to the growth temperature of 400 °C in As background transforms a large portion of the surface from Si (1×1)-H to Si (1×1)-As [69,146]. At annealing temperature up to approximately 500 °C hydrogen atoms desorb from the hydrogen passivated silicon surface and becomes As-passivated in As ambient [145]. An As-passivated silicon surface was found to have a very low surface energy due to the existence of As lone-pair states [147] inducing Volmer-Weber (VW) island growth. Moreover, the arsenic terminated surface was shown to resemble InAs (111)B oriented surface and nucleation of VW islands on such a surface results in a very high yield of CF NWs [143,145,148].

Although the As-passivated surface should be very stable [147], the passivation of the surface may still be incomplete due to the temperature dependence of adsorption and desorption of As atoms on silicon [146]. The silicon surface may therefore contain at the same time some portions of unpassivated surface [149] and surface that resemble InAs(111)A surface [53,69] which have different surface energies in comparison to As-passivated surface. The VW islands that nucleate on the unpassivated and InAs(111)A-like surfaces may not develop the top (111) facets and therefore continue to grow isotopically as islands as reported in [53,70,145]. This simple argument applies to our case where 100% yield of NWs was not achievable. Overall, a spectrum of defect sites exists on the sputtered substrate enabling InAs crystal nucleation whose density and morphology depends on the annealing conditions.

4.2.3 Dependence of *N* and *Y* on growth temperature

Figure 4.15(a) shows the variation of N as a function of the T_{growth} for SiO_2 sputtered silicon substrate by employing two different sputtering parameters and for ICP argon sputtered silicon surface. NW growth time was fixed at 15 min and was preceded by annealing at T_{ann}=790 °C for 15 min. The inset represents Arrhenius plot of the same set of data of SiO_2 sputtered silicon surfaces from which the activation energy is derived. Figure 4.15(b) shows the variation of Y as a function of the T_{growth} for the SiO_2 sputtered samples.

Figure 4.15(a) reveals that N strongly declines upon increasing the growth temperature for all types of substrates. The crystal density N for the substrate sputtered with parameters $t_{sputter}$=3 s and $V_{sputter}$=345 V (red squares) is reduced to zero at 420°C while at the same temperature N=25/μm^2 for substrate with parameters $t_{sputter}$=60 s and

$V_{sputter}$=520 V (green circles). On the other hand, the argon sputtered sample has a very narrow temperature window with N=0.7/μm^2 at 365 °C and no nucleation takes place above 400°C for a fixed growth time of 15 min (blue triangles).

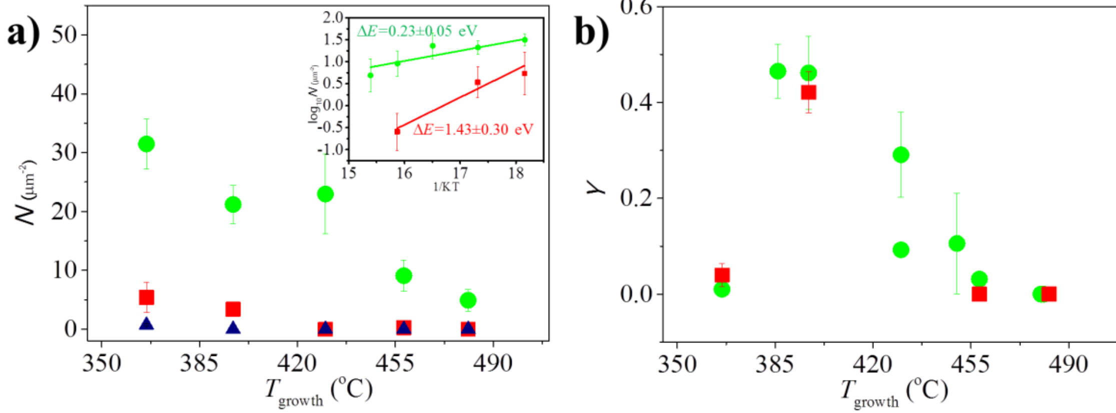

Figure 4.15. (a) Growth temperature dependence of InAs crystal density (N) for three different substrate preparation protocols using SiO_2 sputtering with sputtering parameters $t_{sputter}$=60 s, $V_{sputter}$=520 V (green circles) and $t_{sputter}$=3 s, $V_{sputter}$=345 V (red squares) and ICP argon sputtering with sputtering parameters $t_{sputter}$=600 s, $V_{sputter}$=35 V (blue triangles). The inset shows an Arrhenius plot of the same data from which the activation energy is determined. (b) Yield of InAs NWs as a function of T_{growth} for the SiO_2 sputtered samples shown in (a). Figures are adapted from Ref.[85].

This simple observation can be rationalized by the island nucleation theory [138,150]. According to the theory, the crystal nucleation density, N, is given as [151]:

$$N \propto N_D \exp\left(-\Delta E_b / KT_{growth}\right) \exp\left(\Delta E_T / KT_{growth}\right) \qquad 4.2.1$$

Here N_D is the density of surface defects and ΔE_b is the nucleation energy barrier associated with defect-mediated heterogeneous nucleation. Generally, a high density of defects effectively reduces ΔE_b and enhances the nucleation rate. On the other hand, ΔE_T is the sum of a number of energy terms for thermally activated processes accounting for surface diffusion, desorption, dissociation of InAs critical nuclei, etc. [150,152].

According to Eq 4.2.1, the first exponent will result in increase and the latter in decrease of the nucleation density with T_{growth}. Therefore, the decrease in N with increasing T_{growth} as evidenced in Figure 4.15(a) is due to the increase in thermally activated processes like surface diffusion and desorption.

The total activation energy, ΔE is the sum of ΔE_b and ΔE_T . ΔE is derived from the

Arrhenius plot (see inset of Figure 4.15(a)) and is 0.23±0.05 eV for SiO_2 sputtered silicon with parameters $t_{sputter}$=60 s at 520 V which is lower than 1.43±0.30 eV for sputtered silicon with parameters $t_{sputter}$=3 s at 345 V. These results confirm that increased sputtering time and voltage increases the surface defect density and lowers the total nucleation energy barrier when grown under identical conditions. As N is 0 for ICP argon sputtered silicon at temperature greater than 400 °C, no Arrhenius plot could be obtained.

In Figure 4.15(b) it can be seen that there is an optimum temperature window where the yield of NWs is maximum. It is seen that within the temperature window of 385-395°C, ~50% of the InAs crystals nucleated are NWs. In order to understand this, the island nucleation theory must be coupled with the self-induced nucleation mechanism. According to the self-induced nucleation mechanism, the three dimensional VW islands undergo a series of shape transformations to form NWs [48,128,153]. Such a process is thermally activated and an optimum temperature is required to overcome the energy barrier for shape transformations [72,154,155]. At an optimized temperature, a large fraction of three-dimensional VW islands can transform into NWs thereby increasing the yield as shown in Figure 4.15(b).

4.2.4 Dependence of *N* and *Y* on sputtering parameters

Figure 4.16(a) shows a plot of crystal density (N) versus $t_{sputter}$ for a fixed $V_{sputter}$=345 V and Figure 4.16(b) shows N versus $V_{sputter}$. Sputtering at $V_{sputter}$=345 V corresponds to a SiO_2 deposition rate of 1Å/s, i.e 20 nm of oxide is deposited for $t_{sputter}$ =200 s. After sputtering, the substrates were etched for 2 min in BOE to remove the deposited oxide, rinsed in deionized water and blown dry with nitrogen. On all samples, NWs were grown at 400 °C for 15 min with P_{TBAs}=3.0 Torr and P_{TMIn}=0.3 Torr after annealing at 790 °C for 15 min in P_{TBAs}=1.0 Torr. Figure 4.16 (c) shows a plot of NW yield (Y) versus $t_{sputter}$ for a fixed $V_{sputter}$=345 V and the inset shows Y versus $V_{sputter}$.

It is seen from Figure 4.16(a) that N increases with increasing $t_{sputter}$ from 3 s to 200 s and saturates after 200 s of sputtering. Increase of N from 3 s to 200 s is likely due to the increase of defect density with sputtering time. Instead N does not increase after 200 s because the deposited oxide of thickness t_{ox}=20 nm masks the penetration of SiO_2 atoms to the silicon substrate such that no new surface defects are created. In Figure 4.16(b) N increases from 85 V to 345 V while it is reduced at the highest $V_{sputter}$=820 V. The reduction in N at the highest bias is likely due to damage of the substrate leading to

amorphization. Figure 4.16(c) shows that the yield of NWs is independent of both parameters, i.e $t_{sputter}$ and $V_{sputter}$.

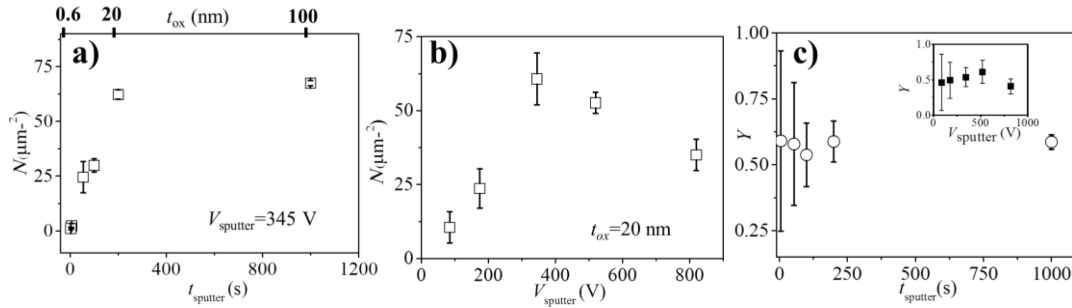

Figure 4.16. (a) Variation of N on SiO_2 sputtered silicon as a function of $t_{sputter}$ and (b) $V_{sputter}$. (c) Variation of Y on SiO_2 sputtered silicon as a function of $t_{sputter}$. The inset shows the variation of Y as a function of $V_{sputter}$. Figures are adapted from Ref.[85].

Figure 4.17(a) shows the dependence of N on ICP argon sputtered silicon substrate as a function of $t_{sputter}$ for a fixed $V_{sputter}$=35 V and Figure 4.17(b) shows a plot of N vs $V_{sputter}$ for a fixed $t_{sputter}$=600 s. After sputtering, the substrates were etched for 2 min in BOE to remove any form of residues and oxides. The substrates were rinsed in deionized water and blown dry with nitrogen. All samples were grown at 400 °C for 15 min with P_{TBAs}=3.0 Torr and P_{TMIn}=0.3 Torr after annealing at 790 °C for 15 min in P_{TBAs}=1.0 Torr.

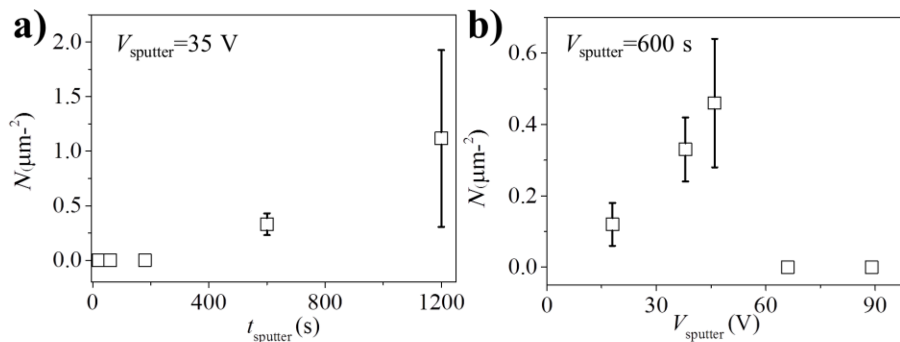

Figure 4.17. Variation of N on ICP argon sputtered silicon as a function of $t_{sputter}$ for a fixed $V_{sputter}$=35 V (b) Variation of N as a function of $V_{sputter}$ for a fixed $t_{sputter}$=600 s. Figures are adapted from Ref.[85].

It is seen from Figure 4.17(a) that the InAs crystal density increases with increasing $t_{sputter}$ due to the increase of defect density with sputtering time. In Figure 4.17(b) N increases from 10 V to 40 V but reduces to zero at higher values. The reduction in N at $V_{sputter}$>40 V is due to etching of the silicon surface. The yield of NWs for all the

samples is independent of sputtering parameters and lies in the range of 40-50%.

4.2.5 Dependence of *N* on growth time

In Figure 4.18(a) and (b), N is plotted as a function of t_{growth} grown on ICP argon sputtered substrate with sputtering parameters $t_{sputter}$=600 s, $V_{sputter}$=35 V and SiO_2 sputtered sample with sputtering parameters $t_{sputter}$=60 s and $V_{sputter}$=520 V. Figure 4.18(c) is a plan-view SEM micrograph of a sample grown for 135 min on ICP argon sputtered substrate and Figure 4.18(d) and (e) are SEM micrographs of samples grown for 15 and 60 min respectively on SiO_2 sputtered substrate. Growth is conducted at T_{growth}=400 °C.

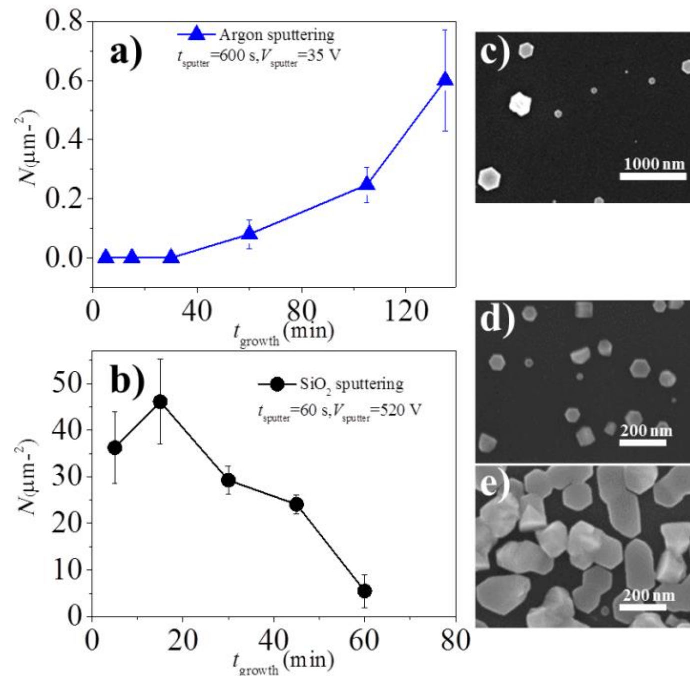

Figure 4.18. InAs crystal density as a function of growth time on an (a) ICP argon sputtered substrate and (b) SiO_2 sputtered substrate. Plan-view SEM micrograph of InAs crystals (c) after 135 min of growth on argon sputtered sample (d) after 15 min and (e) after 60 min of growth on SiO_2 sputtered sample. Figures are adapted from Ref.[85].

For ICP argon sputtered substrate, as shown in Figure 4.18(a), N increases with increasing t_{growth} yielding NWs with a large diameter distribution as shown in Figure 4.18(c) after 135 min of growth. However, no significant increase in N with t_{growth} is seen in SiO_2 sputtered substrates (Figure 4.18 (b)). Rather N decreases with t_{growth}. This is because the variation of N with t_{growth} is strongly affected by (i) surface coverage and (ii) coalescence effects. The high density of InAs crystals at the early stages of growth

covers a large fraction of the surface. As the growth time is increased, the size of the crystals increases which further increases the surface coverage. High surface coverage reduces new nucleation events such that *N* does not change appreciably [110,138]. Furthermore, the coalescence of InAs crystals reduces the overall crystal density. The coalescence can be seen in plan-view SEM micrograph in figure 5(e) for a sample grown for 60 min. Hence, the occurrence of new nucleation cannot be reliably inferred from Figure 4.18(b).

4.3 Chapter summary

In section 4.1, we demonstrated CF growth of InAs NWs on Si (111) substrates. In order to grow InAs NWs with controlled morphology and high aspect ratio, we presented a two-temperature growth protocol having a LT nucleation stage and HT growth stage. Growth begins and proceeds during the high-temperature step without any metal catalyst at the NW tip thanks to the lower nucleation energy barrier on the top (111) NW facet with respect to its side facets. The resulting NWs have a mixed WZ/ZB crystal structure and predominantly grow normal to the Si {111} surface plane. We analysed the influence of the growth parameters on the NW morphology. In particular, the optimum temperature to obtain NWs with the highest aspect ratio was shown. The impact of the TBAs and TMIn line pressures on the NW growth rate and morphology was also investigated and modelled. The general model yielded good agreement with the experimental results for the whole set of deposition conditions and growth durations. In section 4.2, we have investigated the heterogeneous nucleation of CF InAs NWs on silicon substrate. In particular, we have shown that InAs crystals nucleate on sputtered Si (111) surfaces while no nucleation occurs on non-sputtered Si (111) surfaces. We discuss the role of surface defects as preferential nucleation sites formed by sputtering under controlled parameters using different sputtering techniques. The InAs crystals nucleating on the sputtered silicon surfaces consist of InAs NWs as well as parasitic islands. Although the nucleation of parasitic islands could not be completely inhibited, the yield of NWs can be increased up to ~0.5 by proper choice of growth and annealing temperatures. We show that a range of InAs NW densities can be obtained by modifying *in situ* growth and *ex situ* sputtering parameters.

5 Self-catalyzed InAs NWs

This chapter focusses on the nucleation and growth mechanism of self-catalyzed (SC) InAs NWs grown on Si (111) substrates. SC InAs NWs nucleate from an In droplet and grow by the VLS mechanism while sustaining an In droplet at the tip. This is achieved by careful choices of the growth parameters leading to In-rich conditions. The growth parameters allowing SC NW growth are discussed thoroughly in this chapter. Even though, the SC NWs grow by the well-known VLS mechanism, the SC mechanism has its own specific features and therefore needs a dedicated theoretical treatment. The observed behaviour in SC NW nucleation and growth is therefore described within suitable theoretical model allowing us to extract relevant growth parameters. This chapter includes content from: U. P. Gomes, D. Ercolani, V. Zannier, J. David, M. Gemmi, F. Beltram and L. Sorba, Nanotechnology, 27, 255601 (2016)

5.1 Nucleation and growth mechanism

The NW growth process employed for growing SC InAs NWs is depicted in Figure 5.1.The silicon substrates were prepared by SiO_2 sputtering with $t_{sputter}$=60 s and $V_{sputter}$=520 V. The growth process involved a standard high temperature annealing (T_{ann}) under TBAs flux of 1.0 Torr for 15 min. After the annealing step, the temperature was ramped down to the growth temperature T_{growth} and InAs growth was initiated for a growth time of t_{growth} by introducing In and As fluxes at MO line pressures of P_{TBAs} and P_{TMIn} yielding different line-pressure ratios (F=P_{TBAs}/P_{TMIn}). The NW growth was terminated by cooling down the samples without As flux.

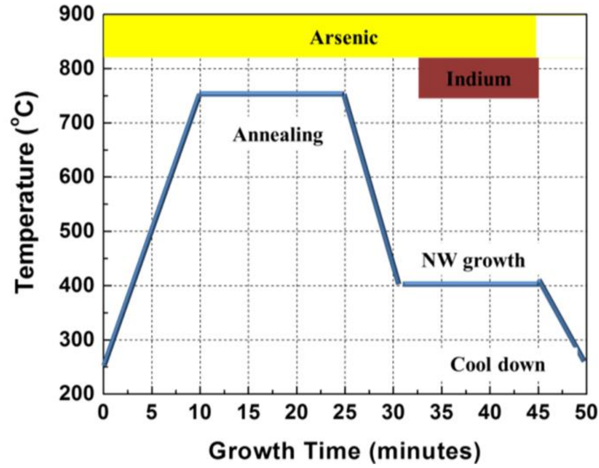

Figure 5.1. Schematic of the growth protocol consisting on an annealing step and SC NW growth step.

The line pressures used for the growth are plotted in Figure 5.2(a) as open squares and circles in a P_{TBAs}-P_{TMIn} map. The solid line corresponds to the F=1 line. All samples were grown for t_{growth} =30 min at 370 °C. In Figure 5.2(a) the open circles represent the growth conditions in which a droplet was observed on the NW tip, and they all lie in the F<1 region of the parameter space. The open squares represent conditions in which NWs grow without a droplet on the NW tip, and they and all lie in the F≥1 area of the parameter space. The 45° tilted SEM micrographs shown in Figure 5.2(b-e) illustrate the morphological transition from droplet to droplet-less NWs as F is changed from 0.75 to 1.00. For F=0.75 (P_{TMIn}=0.40 Torr, P_{TBAs}=0.30 Torr, purple circle), InAs NWs grow with an indium droplet at the NW apex as shown in Figure 5.2(b) and confirmed by EDX analysis (see Figure 5.11(a)). At F=0.81 (P_{TMIn}=0.37 Torr, P_{TBAs}=0.30 Torr, red circle), the growth of InAs NWs with In droplets was still observed. However, NWs have a tapered morphology and the average droplet size is reduced (Figure 5.2(c)).

At F=0.86 (P_{TMIn}=0.35 Torr, P_{TBAs}=0.30 Torr, green circle), a dramatic change in morphology is observed with the formation of InAs NWs with and without the droplet at the NW tip as shown in Figure 5.2(d). The NWs without the droplet have complex faceting as shown in the inset. At F=1.00 (P_{TMIn}=0.30 Torr, P_{TBAs}=0.30 Torr, orange square), no NWs show In droplets at the tip and all exhibit a regular hexagonal shape with well-defined side facets. The F≥1 regime can therefore be used to grow CF InAs NWs [126] while the SC growth occurs in the regime of F<1 as depicted in Figure 5.2(a). These observations are in agreement with the growth-mode transition of NWs from SC to CF by controlling the V/III ratio observed for GaAs [47] and InAsSb NWs [156].

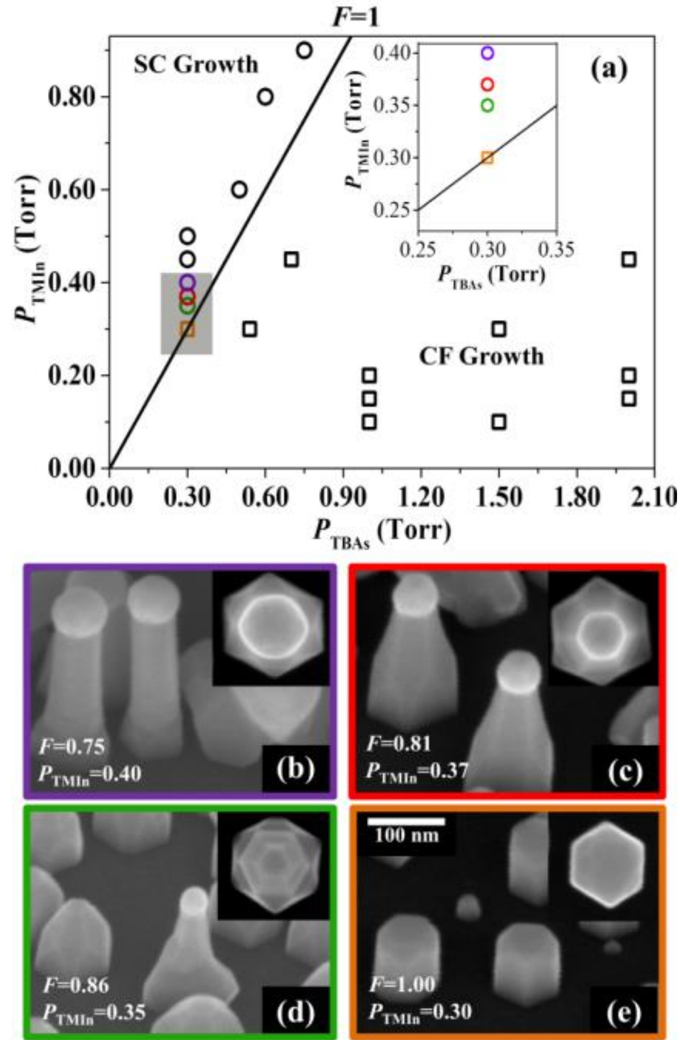

Figure 5.2. (a) Map showing the line pressures P_{TBAs} and P_{TMIn} used for InAs NW growth. Each symbol corresponds to a grown sample: squares are CF InAs NWs and circles correspond to SC InAs NWs. The black solid line corresponds to F=1 line. The inset is a magnified view of the shaded region of the main panel. (b-e) Selected 45° tilted SEM micrographs of NWs (with a top-view inset of a single NW) grown with different F (P_{TBAs}/P_{TMIn}) by changing P_{TMIn} and fixing P_{TBAs} at 0.30 Torr as shown in the inset of panel (a). The color of the frame of each SEM image corresponds to the colored symbols in panel (a). Figures are adapted from Ref.[73].

5.2 Length-radius dependence

Figure 5.3(a) shows a plot of NW radius (R_{NW}) versus length (L_{NW}) of an ensemble of SC InAs NWs measured from a series of samples with different sample growth times (namely, t_{growth}=15, 30, 45 and 70 min). Each of the experimental points represents the measurement of a single NW while the solid line is a theoretical fit using Eq. 5.3.4. The colors of the points correspond to different sample growth times. Matching colored pins are used as markers to highlight the maximum length (L_{max}) and maximum radius (R_{max})

of NWs for various t_{growth} values. The inset is the plot of R_{NW} as a function of the In droplet radius (R_{In}) for the same ensemble of NWs shown in the main panel. Figure 5.3(b) is a representative 45° tilted SEM image of the longest NW selected from panel (a) for different growth times (indicated by colored markers). For illustrative purpose a 45° tilted SEM image of an InAs NW from a sample grown for 5 min is also shown. The NW morphology could not be accurately measured for such a short sample growth time and is therefore not plotted in Figure 5.3(a).

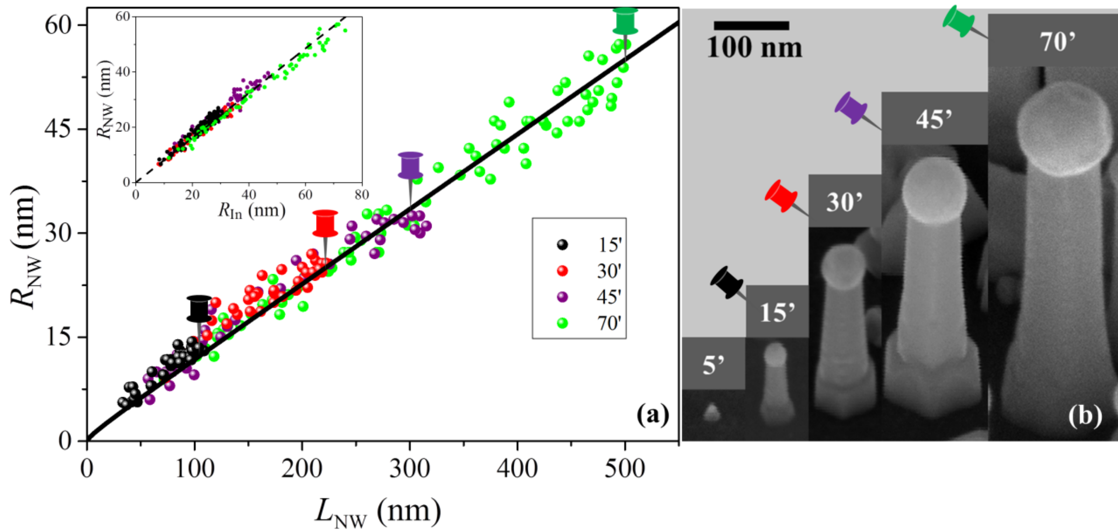

Figure 5.3. (a) R_{NW}- L_{NW} distributions for SC InAs NWs for t_{growth}= 15, 30, 45, and 70 min. Coloured spheres mark experimental data points that correspond to measurements done on a single NW. The colours of the points refer to different growth times. The solid line is a theoretical fit of the experimental data. The pins mark NWs with L_{max} and R_{max} under different growth durations. The inset is a plot of R_{NW} as a function of R_{In} with a linear fit; (b) 45° tilted SEM micrographs of longest NWs for different sample-growth times (marked by coloured pins). Figures are adapted from Ref.[73].

For each sample growth time there is a clear spread in the NW length and radius distribution as seen from Figure 5.3(a). For t_{growth} = 15 min (black dots), NWs have radius distribution in the range of 5-15 nm and length in the range of 25-110 nm. The distribution widens with increasing sample-growth time so that the experimental points overlap the distributions of samples for shorter growth times. At the longest t_{growth} value of 70 min (green dots), R_{NW} and L_{NW} lie in the range of 5-60 nm and 70-500 nm, respectively, overlapping the entire range of shorter sample growth time series. In the inset of Figure 5.3(a), the measured droplet radius scales linearly with the NW radius implying that the In droplet contact angle is independent from time, NW length and

radius. The R_{NW}-L_{NW} distributions for various t_{growth} values, as shown in Figure 5.3 can be interpreted within the frame of recent existing theoretical models on SC III-V NWs [62,157,158].

5.3 SC NW growth model

In our model, we assume a cylindrically-shaped NW with a spherical apical In droplet. The droplet shape is determined by its radius R_{In} and contact angle β. The NW radius R_{NW} equals the base radius of the In droplet spherical cap (see the schematic description in Figure 5.4).

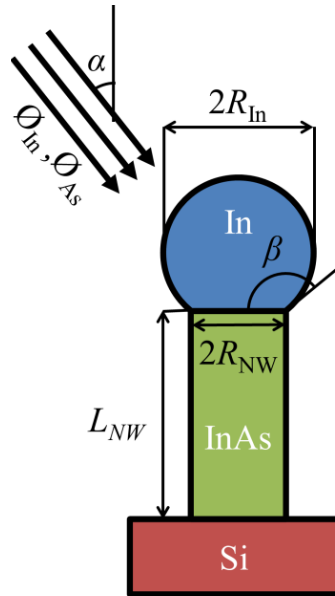

Figure 5.4. Schematic description of a SC InAs NW on a silicon substrate illustrating the geometrical parameters of NW, In droplet and CBE chamber geometry used in the growth model. Figure is adapted from Ref.[73].

We assume that the droplet is a reservoir of In atoms which are supplied by direct impingement and by sidewall diffusion as a result of a uniform flux of the In (ϕ_{In}) beam making an angle α with the NW axis. Diffusion of In atoms from the substrate to the droplet is neglected. Likewise, the droplet receives As species from a uniform flux of As beam (ϕ_{As}) impinging at the same angle α. Since sidewall diffusion of As can be safely neglected [88,159], we assume that the liquid droplet is fed by As through direct impingement only. Possible re-emission of As from the neighboring NW sidewalls and substrate can be accounted for by defining an effective ϕ_{As} [159,160]. In and As atoms are instead subtracted from the droplet due to the growth of InAs at the liquid-solid

interface. We assume that the desorption of In and As atoms from the droplet is negligible (if not, it can be incorporated as a factor in ϕ_{As} and ϕ_{In}). Furthermore, we assume that the axial growth rate of the NW is limited only by the kinetics of As species since In is always available from the droplet: $dL_{NW}/dt = \Omega_{InAs} f(\alpha,\beta)\phi_{As}$. Integrating over NW growth time, for a constant contact angle β, the length of an individual NW is given by:

$$L_{NW} = \Omega_{InAs} f(\alpha,\beta)\phi_{As} t_{NW} \quad 5.3.1$$

where $\Omega_{InAs} = 0.0556$ nm^3 is the volume per In-As dimer in ZB InAs ($\Omega_{InAs} = 0.0549$ nm^3 in WZ InAs) [135], $f(\alpha,\beta)$ is a geometrical factor representing the ratio between the cross-sectional area of the droplet normal to the impinging beam and the area of the growth front of the NW. The expression of $f(\alpha,\beta)$ was derived by Glas [161] and we shall use this result for the range of α and β of interest for the present work (i.e. $\beta \le \alpha + \pi/2$). t_{NW} is the growth time of the individual NW, i.e. the time elapsed from NW nucleation (which may be different from the sample total growth time, t_{growth}). We assume that not all NWs nucleate at the beginning of the growth when the MO precursors are switched on, rather each individual NW begins growth at a time, $t_{nucleation}$, after sample growth start. Thus $t_{NW} = t_{growth} - t_{nucleation}$ and the length of an individual NW is expressed as

$$L_{NW} = C(t_{growth} - t_{nucleation}) \quad 5.3.2$$

where $C = \Omega_{InAs} f(\alpha,\beta)\phi_{As}$

According to Eq. 5.3.2, at the end of a given sample growth a distribution of NW length values, L_{NW}, is possible only if individual NWs have different nucleation times under the condition that the In droplet is not consumed during growth and C is a constant.

On the other hand, the radial growth rate is determined by the kinetics of both In and As species. If too much In is supplied to the droplet, its size will increase with time. Conversely, if there is a net loss of In from the droplet during growth, the later will shrink with time. Taking into account this kinetics, the NW radius can be obtained from the material balance equation as follows [62,157,158]:

$$At_{NW} = R_{NW} + B/A \ln\left(\frac{B/A}{B/A + R_{NW}}\right) \quad 5.3.3$$

where $A = \Omega_{In} f(\alpha,\beta)\nu(\beta)(\phi_{In} - \phi_{As})$, $B = \Omega_{In}\nu(\beta)\frac{2\lambda \sin\alpha\phi_{In}}{\pi}$, λ is the In diffusion length on NW sidewalls, Ω_{In} =0.0261 nm^3 is the In atomic volume [135], and

$v(\beta)=(2-3\cos\beta+\cos^{3}\beta)^{-1}\sin^{3}\beta$ is the volume of a spherical cap of unitary radius having contact angle β. B is the diffusion term that models the contribution of In diffusion to the droplet; A is the flux imbalance term, accounting for the relative weight of group III and V fluxes. Indeed it can be seen from the equation that –focusing on the flux-imbalance term– an excess of In supplied to the droplet (A>0) causes the droplet size to increase while it will shrink for A<0 due to net In loss during crystallization.

Figure 5.5 shows how the dependence of R_{NW} on the growth time varies as λ changes. The curves are obtained using Eq. 5.3.3 with A=1.6 and B=750 (black curve), A=1.6 and B=100 (orange curve), A=1.6 and B=8 (green curve), and A=1.6 and B=0 (red curve). It can be seen that increasing values of λ makes the curve non-linear. The same theoretical treatment has been utilized in [62].

To describe the R_{NW} -L_{NW} distribution of SC NWs, we combine Eq. 5.3.1 and 5.3.3, such that the following equation is obtained:

$$L_{\mathrm{NW}} = C/A \cdot R_{\mathrm{NW}} + C/A \cdot B/A \cdot \ln\left(\frac{B/A}{B/A+R_{\mathrm{NW}}}\right) \quad . \qquad 5.3.4$$

Here, L_{NW} is linked to R_{NW} by parameters $A(\alpha,\beta,\phi_{\mathrm{As}},\phi_{\mathrm{In}})$, $B(\alpha,\beta,\lambda,\phi_{\mathrm{In}})$, $C(\alpha,\beta,\phi_{\mathrm{As}})$. Note that time is not present in the relationship between NW length and radius. For a given droplet and chamber geometry, fixed group III and V fluxes, whatever the sample growth time t_{growth} (for different samples) or the nucleation time $t_{\mathrm{nucleation}}$ of each individual NW, all (L_{NW}, R_{NW}) points must fall on the same line, with upper limits $L_{\max}$, $R_{\max}$ determined by t_{growth}. The lower limit is either zero or some finite value if there is a nucleation delay or if nucleation ceases at a certain point during growth.

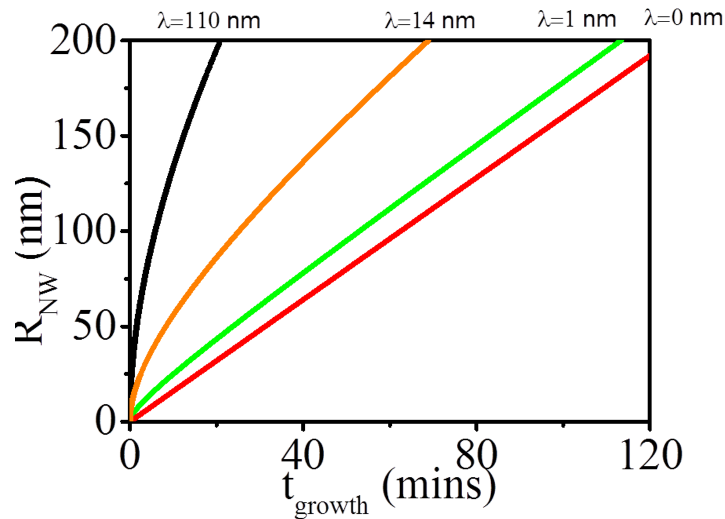

Figure 5.5. Variation of R_{NW}- t_{growth} correlation as a function of diffusion length λ.

5.4 Modelling results and discussion

A discussion of the experimental data within the model is now presented. The spread and overlap of experimental points with growth time shown in Figure 5.3(a) indicate that SC InAs NWs do not nucleate simultaneously. NWs that nucleated in the first seconds of growth continue to increase in length and radius finally attaining maximum values L_{max} and R_{max} (marked by coloured pins in Figure 5.3(a)) at the end of the growth, while NWs with shorter length and smaller radius nucleated at later nucleation times, $t_{nucleation}$. Thus, $t_{nucleation}$ of an individual NW can be determined using Eq. 5.3.2 for a known L_{NW}, t_{growth} and C. The spread in nucleation times in SC GaAs NW growth was ascribed to slow pinhole formation in the surface oxide layer [162]; in the present case, however, the mechanism driving the delayed nucleation is ascribed to surface defects with different nucleation energies that depend on T_{growth} and T_{ann} for a given t_{growth} and sputtering parameters as discussed in chapter 4. Figure 5.3(b) shows 45° tilted SEM micrographs of individual NWs with dimensions L_{max} and R_{max} from samples grown from 5-70 min. The figure shows axial NW growth together with a significant radial growth. Within measurement accuracy, L_{max} and R_{max} increase linearly with growth time. It is also evident from NW morphology that the droplet dimension increases with growth time too. In fact, the maximum droplet radius increases linearly with growth time. Such a morphological change of the droplet observed in Figure 5.3(b) indicates that the line pressure employed (P_{TMIn}=0.40 Torr and P_{TBAs} =0.30 Torr) provide a surplus supply of In atoms that accumulate in the droplet rather than crystallize into InAs, so that the flux imbalance parameter A is > 0.

The experimental data of Figure 5.3(a) fits very well with Eq. 5.3.4 (fitting parameters are C/A=4.67±0.14 and B/A=0.57±0.56 nm). The contact angle β used in the fit was determined to be $\beta = 125 \pm 0.9°$ from the slope of R_{In} vs. R_{NW} (see inset of Figure 5.3(a)) using $\cos(\beta - 90) = R_{NW}/R_{In}$. The incident flux angle to the substrate normal is $\alpha = 38°$ and the value of the geometrical factor $f(\alpha, \beta)$ for $\alpha = 38°$ and $\beta = 125°$ is 4.68.

The C/A value allows us to determine the effective V/III flux ratio $\phi_{As}/\phi_{In} = (1+\Omega_{InAs}/\Omega_{In}\nu(\beta)\cdot C/A)^{-1}$=0.25±0.095. This value is less than F (P_{TBAs}/P_{TMIn}) = 0.75 and it reflects the different precursor masses and decomposition and incorporation behaviour of the MOs used.

The B/A value, in turn, can be used to estimate the In atoms sidewall diffusion length $\lambda = \pi(f(\alpha, \beta)/2\sin\alpha)(1-\phi_{As}/\phi_{In})B/A$=1.7±1.7 nm. This negligible diffusion length fully

justifies the choice of ignoring substrate diffusion and of neglecting the details of NW shape, since both contribute only if some species diffuse from the sidewalls to the droplet. This somewhat surprising absence of diffusion can stem from several concurring effects. First, the growth temperature is very low (370 °C) thus reducing adatom mobility. Second, the value of λ comprises several factors accounting for the complex nature of MO precursor decomposition and incorporation kinetics in the catalyst and on the sidewalls [163], the desorption probability, and the presence of a diffusion barrier at the sidewall/catalyst boundary. The combination of all these factors can lead to a net zero contribution of sidewall diffusing species to the catalyst even for an intrinsically non-zero diffusion length of the atoms themselves.

The limitation of the SC-VLS theoretical model used to fit our experimental data is that the influence of sidewall growth on the overall NW morphology is not taken into consideration. In fact for SC-VLS mechanism, radial growth with positive flux imbalance ($A>0$) and negligible sidewall growth leads to a reverse tapered morphology [164,165]. Instead no reverse-tapering is observed in our SC InAs NWs for $A>0$. In this regards, the NW shape can be preserved only if the sidewall growth rate of the NW is larger than the radial growth rate. The In atoms reaching the sidewalls (by surface diffusion or direct impingement) gets incorporated on the sidewalls by reacting with As atoms thereby widening the base radius relative to the NW radius typically leading to tapered shape. The sidewall growth rate increases with increasing F as a high As flux increases the incorporation of In on the sidewalls. On the other hand radial growth rate decreases with increasing F, such that the NWs grow with a tapered morphology.

5.5 Influence of MO precursors

Figure 5.6 is a plot of measured L_{max} (squares) and R_{max} (circles) (determined as the average of the longest 10% of measured NWs using standard deviation as associated uncertainty) as a function of P_{TMIn} at fixed P_{TBAs} of 0.30 Torr and t_{growth} of 30 min. In the inset L_{max} is plotted as a function of P_{TBAs} for another series of samples grown for t_{growth} of 30 min. The dashed line is a linear fit of the data.

As seen in Figure 5.6,the change of P_{TMIn} at fixed P_{TBAs} does not influence the NW length which increases linearly with P_{TBAs} (see inset).The observed linear P_{TBAs} dependence of the NW length (independent of P_{TMIn}) is a sound confirmation of the assumptions leading to Eq. 5.3.1 i.e $L_{NW} \propto \phi_{As}$. The NW radius monotonically increases with increasing P_{TMIn} in the investigated range of line pressures. The increase

in NW radius is governed by the flux imbalance. For a fixed P_{TBAs}=0.30 Torr, the parameter $A \propto (\phi_{In} - \phi_{As})$ in Eq. 5.3.3 increases with increasing P_{TMIn}. The droplet in turn gets inflated due to intake of excess indium atoms. Consequently, the NW radius also increases.

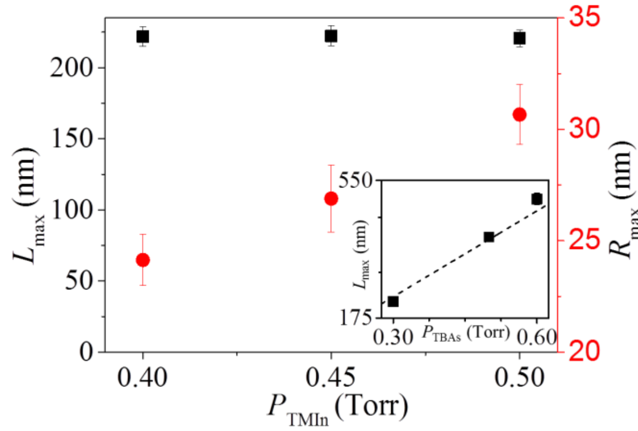

Figure 5.6. Plot of L_{max} (squares) and R_{max} (circles) as a function of P_{TMIn} at a fixed P_{TBAs}=0.30 Torr and t_{growth} was 30 min. The inset is a plot of L_{max} as a function of P_{TBAs}. The dashed line is a linear fit of the data. Figure is adapted from Ref.[73].

Figure 5.7 is a plot of L_{max} (squares) and R_{max} (circles) of SC InAs NWs as a function of P_{TMIn} grown using a two-step growth protocol. The two steps differ for the precursor line pressure ratio F (F_1 and F_2) used at the same growth temperature of 370 °C. The first step is initiated with F_1=0.75 (P_{TMIn}=0.40 Torr and P_{TBAs}=0.30 Torr) to achieve SC NWs (stems) with L_{max}=220±6 nm and R_{max}=21±4 nm after 30 min of growth. The next 40 min of growth is carried out utilizing variable P_{TMIn} at a fixed P_{TBAs}=0.30 Torr yielding F_2 in the range of 0.75-1.00. The inset is a plot of L_{max} (squares) and R_{max} (circles) versus P_{TBAs} of samples grown using a two-step growth protocol in which F_2 in the range of 0.75-1.00 is obtained by varying P_{TBAs} at a fixed P_{TMIn}=0.40 Torr. The colours of the symbols indicate that the NWs have different contact angles. The green symbol corresponds to $\beta \approx 125°$ and red symbol corresponds to $\beta \approx 90°$. The top panel displays SEM image with coloured marker showing the geometry of an In droplet on NW tip along with the value of β for F_2=0.75-0.88 (green) and F_2=1.00 (red).

In Figure 5.7, no significant variation in L_{max} was observed while decreasing P_{TMIn} from 0.40 Torr to 0.34 Torr but R_{max} decreases. The results are in agreement with the model that NW length depends only on the As flux (independent of P_{TMIn}) while NW radius depends on the flux imbalance between As and In. Decreasing P_{TMIn} reduces the flux imbalance parameter A which is $\propto (\phi_{In} - \phi_{As})$(see Eq. 5.3.3) reducing droplet radius and

therefore reducing final NW radius. Within these values of P_{TMIn}, indium droplets do not show noticeable change in geometry and have a typical β of about 125° as shown in the SEM image on the right hand side of the top panel. Further decrease of P_{TMIn} to 0.30 Torr yields F_2=1.00.This results in a further decrease of R_{max} due to the consumption of the droplet. The droplet consumption is also accompanied by a decrease in β which now gets close to 90° as shown on the left hand side of the top panel. As far as the NW length is concerned, a drop in L_{max} occurs. Such a morphological behaviour can be attributed to the decrease in β. L_{max} reduction is in agreement with the reduced value of $f(\alpha,\beta)$ due to the 90° contact angle.

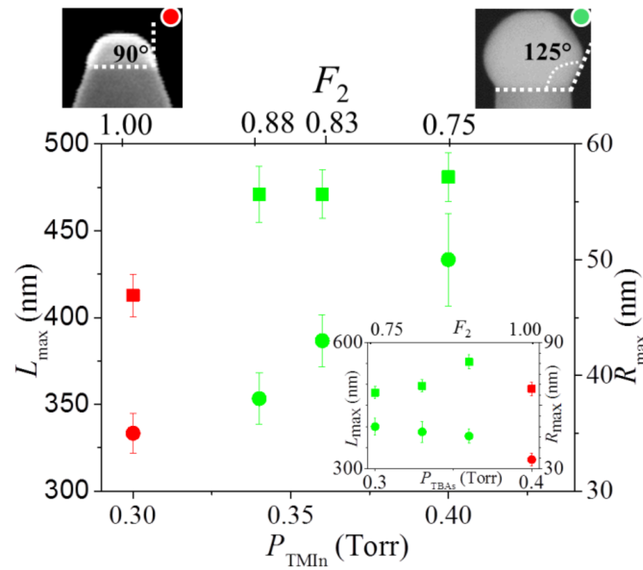

Figure 5.7. Plot of L_{max} (squares) and R_{max} (circles) as a function P_{TMIn}. The samples are grown using two-step approach at a constant growth temperature of 370 °C. The first step is initiated with F_1=0.75 (P_{TMIn}=0.40 Torr and P_{TBAs}=0.30 Torr) to achieve SC NWs (stems) with L_{max}=212±6 nm and R_{max}=21±4 nm after a sample growth time of 30 min. The second step growth is done with F_2 for 40 min at the same growth temperature of 370 °C. P_{TMIn} is changed from 0.40 and 0.30 Torr at a fixed P_{TBAs} of 0.30 Torr resulting in F_2=0.75, 0.83, 0.88 and 1.00. The inset is a plot of L_{max} (squares) and R_{max} (circles) as a function P_{TBAs} of samples grown using the two-step approach. The upper panel shows the geometry of the In droplet on a NW tip for F_2=0.75-0.88 (green) and F_2=1.00 (red). Figure is adapted from Ref.[73].

It is worth noting that the indium droplet on the stems is not completely consumed at F_2 =1.00 which is the regime of CF NW growth (see Figure 5.7). Instead, R_{NW} is 35±2 nm which is larger than that of the stems having average value of 21±4 nm. This situation demands that even with F_2 =1.00 the indium droplets sitting on top of the stems continuously receive either reduced supply of arsenic species or excess indium during

the growth process making A>0. The latter of course is not feasible as we are progressively decreasing P_{TMIn} along with no diffusion contribution ($\lambda \approx 0$). It is possible that alternative routes of arsenic atoms reaching the droplet probably through re-emission that contribute to effective ϕ_{AS} is inhibited. Such a situation leads to high lateral growth [159] and this is experimentally observed in our SC InAs NWs grown by two-step method. However, determination of the remission contribution of arsenic is a non-trivial task for our randomly distributed NWs as it depends on the neighbourhood of the NWs [157].

Similar observations are made when samples are grown with an identical first step for the stems while in the second step F_2 (0.75-1.00) is changed by varying P_{TBAs} at a fixed P_{TMIn}=0.40 Torr (see inset of Figure 5.7). Increase of P_{TBAs} from 0.30 Torr to 0.36 Torr shows an increase in L_{max} and a decrease in R_{max} which is consistent with the model. At F_2=1.00 (P_{TMIn}=0.40 Torr and P_{TBAs}=0.40 Torr), L_{max} decreases in spite of increasing P_{TBAs} as β is now close to 90°.

5.6 Influence of growth temperature

The growth of SC InAs NWs was investigated in a temperature ranging from 310 to 410 °C with P_{TBAs}=0.30 Torr and P_{TMIn}=0.40 Torr for a growth time of 30 min, following the standard protocol (see Figure 5.1). Figure 5.8(a) shows the yield of vertically aligned NWs growing along <111> direction versus the growth temperature along with selected SEM micrographs (b-d) of NWs grown at different temperatures. The yield of NWs is the ratio of density of straight InAs NWs aligned to the <111> direction to the total density (kinked NWs + NWs growing along <111> direction and non-<111> directions).Generally, the majority of NWs growing along the non-<111> directions are planar NWs that grow along the substrate.

At the highest temperature of 410 °C, all the NWs have kinked morphology as shown in Figure 5.8(d) and gives a yield of 0. At intermediate temperature range from 350-370 °C the growth of NWs with highest yield is achieved (Figure 5.8(c)). Most of the InAs NWs grow along the <111> direction with negligible density of kinked and planar NWs. The maximum yield of NWs is ~60 %. As the substrate temperature is reduced to 335 °C, formation of islands and kinked NWs are observed giving a reduced yield of 10%. At very low temperatures of 310 °C no growth of SC NWs is observed as shown in Figure 5.8(b).

The kinking of NWs may be related to the instabilities at the liquid/solid interface

caused by abrupt changes of effective V/III ratio which depends on temperature [71,166,167]. At high temperatures, the amount of In atoms decreases due to desorption which increases the effective ϕ_{As}/ϕ_{In} . The amount of In decreases also at low temperatures as low temperature reduces the pyrolysis of TMIn. Consequently, this will also increase the effective ϕ_{As}/ϕ_{In} . The increase in effective ϕ_{As}/ϕ_{In} may cause kinking of SC InAs NWs. Indeed kinking of NWs due to high V/III ratios have been previously observed in SC NWs [168] and Au-catalyzed NWs [71]. Furthermore, at very low temperature (310 °C), growth of SC InAs NWs is completely inhibited and islands without In droplets are obtained (see Figure 5.8(b)). This may happen if the effective ϕ_{As}/ϕ_{In} fall in the regime of ϕ_{As}/ϕ_{In} >1 where NWs grow by CF mechanism without In droplets. It is likely that at 310 °C, the pyrolysis of TMIn produces very less In atoms making ϕ_{As}/ϕ_{In} >1.

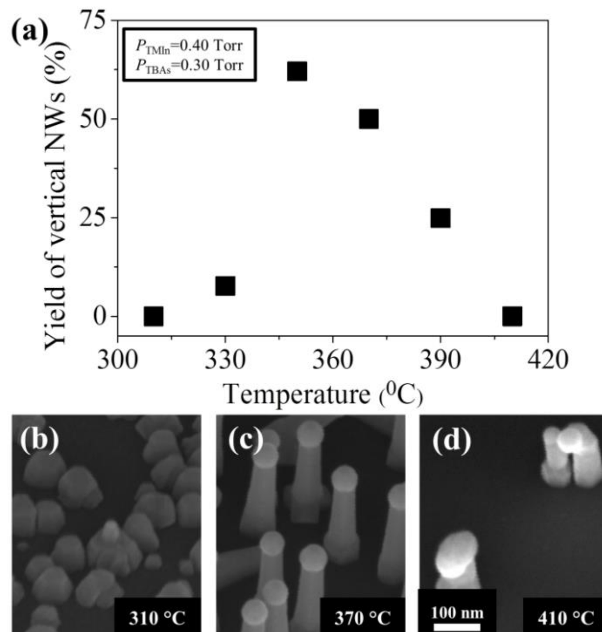

Figure 5.8. (a) Plot of yield of vertical NWs as a function of growth temperature (b) Selected 45° tilted SEM micrographs of SC NWs grown at (b) 310 °C, (c) 370 °C and (d) 410 °C, respectively. SC NWs were grown with P_{TMIn}=0.40 Torr and P_{TBAs}=0.30 Torr and t_{growth} was 30 min.

5.7 Influence of predeposited In droplets

The influence of Indium predeposition step has been investigated in order to form Indium droplets before the NW growth. Indium droplets deposited *in situ* on Si (111) substrate using P_{TMIn}=0.9 Torr at 370 °C for 13 min are shown in the top-view SEM

image of Figure 5.9. The droplets have a wide radius distribution (grey histogram) having an average R_{In} of about 25 nm .The measured contact angle of the droplets on the substrate is about 125°. After indium predeposition, InAs NWs are grown with P_{TBAs}=0.30 Torr and P_{TMIn}=0.40 Torr for sample growth time of 5-15 min. The radius distribution of the droplets at the tip of InAs NWs grown for 15 min is plotted in Figure 5.9 (black histogram) and has an average R_{In} of about 15 nm. The inset is a plot of density of predeposited indium droplets (t_{growth}=0) and density of InAs NWs grown after indium predeposition for t_{growth}=5 and 15 min.

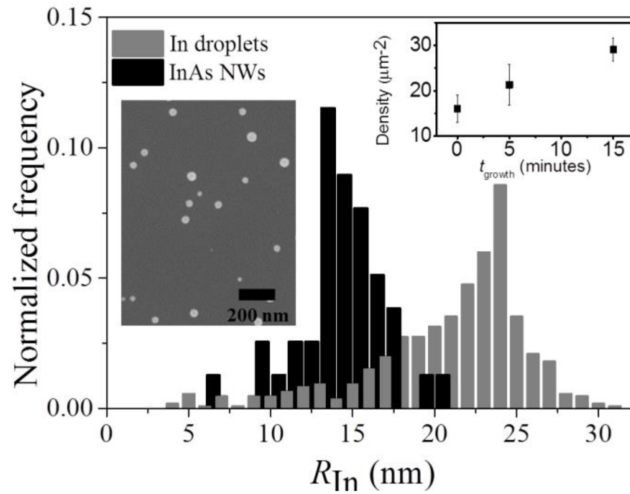

Figure 5.9. Droplet diameter distribution after In predeposition on silicon substrate (grey) and after 15 min NW growth (black) at the NW tip. The top-view SEM image shows predeposited In droplets. The inset is a plot of variation of NW density after 5 and 15 min of growth and the value at 0 is the density of predeposited droplets. Figure is adapted from Ref.[73].

Form Figure 5.9 it is evident that the R_{In} of the droplets deposited on the substrate is larger than that of the droplets at the apex of InAs NWs after 15 min of growth. This is in contrast to the observed variation of R_{In} of InAs NWs with t_{growth} ranging from 5-45 min grown without In predeposition (see Figure 5.3 (a) and (b)). In fact, R_{In} of InAs NWs grown without indium predeposition increases linearly with time as the growth parameters employed (P_{TMIn}=0.40 Torr and P_{TBAs}=0.30 Torr) corresponds to indium-rich conditions i.e A>0. Therefore, the same behaviour is expected for InAs NWs grown from predeposited indium droplets, i.e R_{In} is expected to increase after 15 min of growth time in identical indium-rich growth conditions. The inspection of SEM images of time series (5-15 min) shows that the indium droplets lead to parasitic planar NW growth which could be influenced by thermodynamic factors [169] or the droplets nucleate on nucleation sites (surface defects) that favour parasitic growth (not shown). These results

show that SC InAs NWs are not nucleating from predeposited indium particles but directly from Si (111) surface. An additional confirmation comes from the increase in density of InAs NWs (shown in the inset) beyond the predeposited droplet density due to new nucleation of InAs NWs on Si (111) substrate. This is an important difference from other III-V SC NWs like GaAs [158] and InP [170], where vertically aligned NWs nucleate from pre-deposited group III droplets.

5.8 SC InAs NW length distribution (LD)

The LDs derived by Eqs. 3.3.4, 3.3.5 or 3.3.10 for Au-catalyzed InAs NWs in chapter 3 can also apply for SC NWs in situations where new NWs do not emerge concomitantly with the NW growth. If, however, the nucleation of new NWs is present, the NW nucleation rate is described by a time-dependent function $J(t)$ .Green's function of the continuum rate equations remains Poissonian, and the resulting LD is obtained in the form

$$f(s,\tau) = \frac{1}{\sqrt{\pi}} \int_{\frac{s-\tau}{\sqrt{2\tau}}}^{\infty} dx e^{-x^2} J\left(\sqrt{2\tau}x - s + \tau\right). \qquad 5.8.1$$

Of course, finding particular shapes of the nucleation rate requires additional considerations regarding the nucleation of the group III metal droplets.

The appropriately normalized nucleation rate of NWs in the model is given by $J(\tau) = \alpha.f_0(\tau)$, i.e., is proportional to the concentration of In droplets on the surface. In contrast to the Au-catalyzed case where $f_0(\tau)$ can only decrease with time, the In droplets also emerge at a certain rate j . Therefore, the $f_0(\tau)$ evolves in time according to

$$\frac{df_0}{d\tau} = j - \alpha f_0 \cdot \qquad 5.8.2$$

Assuming j as being time-independent and solving it with the initial condition $f_0(\tau = 0) = 1$ (corresponding to a fixed density of predeposited In droplets), we find the NW nucleation rate

$$J(\tau) = j + e^{-\tau}(\alpha - j) \,. \qquad 5.8.3$$

Injecting this into Eq. 5.8.2 and integrating, the LD of SC InAs NWs is obtained in the form

$$f(s,\tau) = \frac{(\alpha - j)}{2} e^{\alpha(s-\tau)+\alpha^2\tau/2} erfc\left(\frac{s-\tau}{\sqrt{2\tau}} + \frac{\alpha\sqrt{2\tau}}{2}\right) + \frac{j}{2} erfc\left(\frac{s-\tau}{\sqrt{2\tau}}\right). \qquad 5.8.4$$

Compared to Eq. 3.3.10 for the Au-catalyzed case, this LD contains additional parameter j describing the secondary nucleation of In droplets.

Figure 5.10 shows the time evolution of LDs for SC InAs NWs, where In droplets are clearly seen on the NW tips in the SEM micrographs.

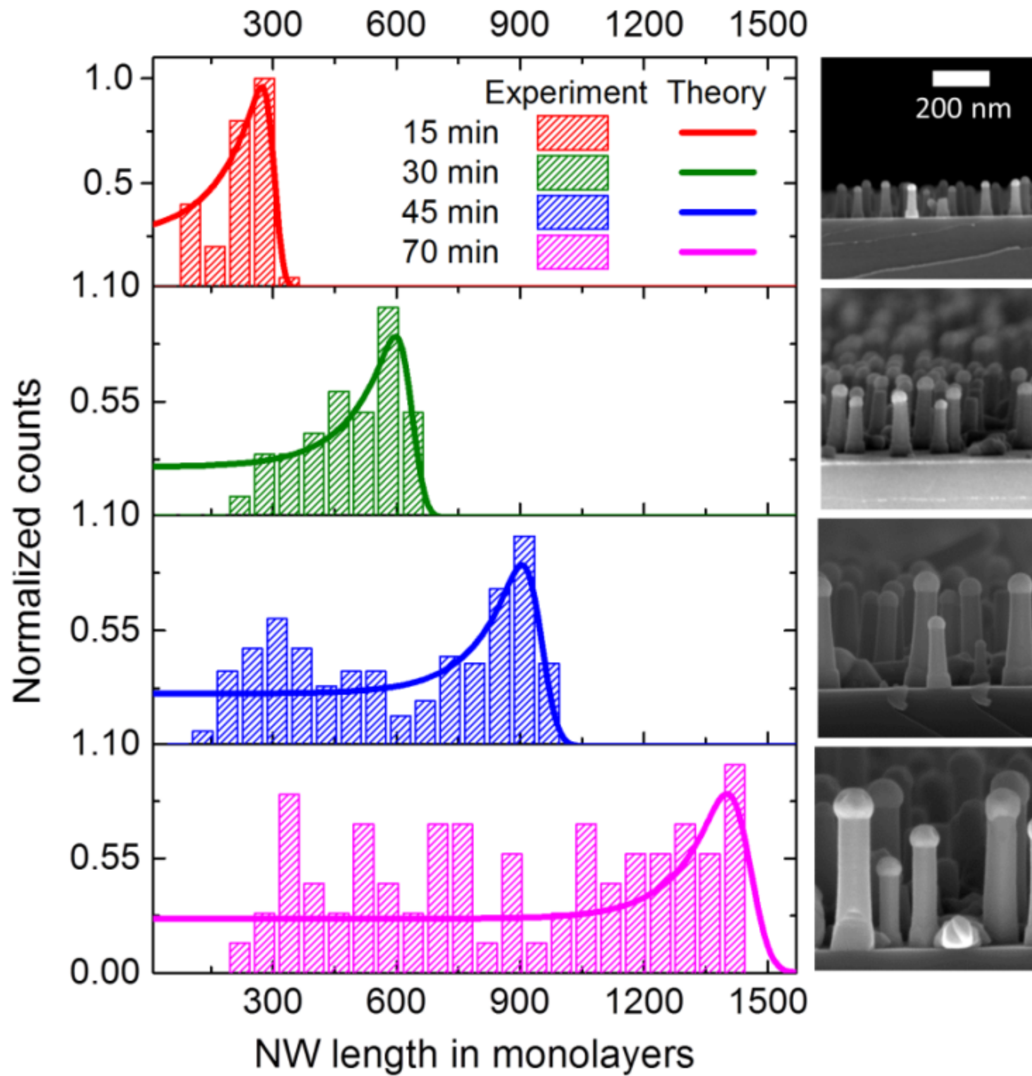

Figure 5.10. Normalized LDs (histograms) fitted by the model (lines) for SC InAs NWs grown for t_{growth}=15-70 min along with the corresponding 90° tilt SEM micrographs. The LDs are normalized to their peak values. Figure is adapted from Ref.[110].

The LDs of SC InAs NWs are very broad, as shown in Figure 5.10- even after 70 min of growth, very short NWs are still present in the histograms. These broadest LDs is due to a continuing nucleation of the In droplets under the effectively In-rich growth conditions. The newly formed droplets subsequently produce InAs NWs and this effect broadens the LDs. The LDs in Figure 5.10 have the peaks at large lengths and show an almost length-independent tail for shorter NWs. We can thus conclude that the NW

nucleation rate is higher at the beginning and saturates for longer times. This is possibly because of the decrease of nucleation events as the surface area is decreases due to material deposition. The fits shown in Figure 5.10 are obtained from Eq. 5.8.4 with $\alpha = 0.01$ and $j = 0.24$ and represent fairly well the major trends in the noisy data.

5.9 Crystal structure

Figure 5.11(a) shows a bright-field TEM image of a NW along with EDX profile and panel (b) shows its diffraction pattern. The sample was grown with F=0.75 (P_{TMIn}=0.40 Torr, P_{TBAs}=0.30 Torr) for t_{growth} of 70 min.

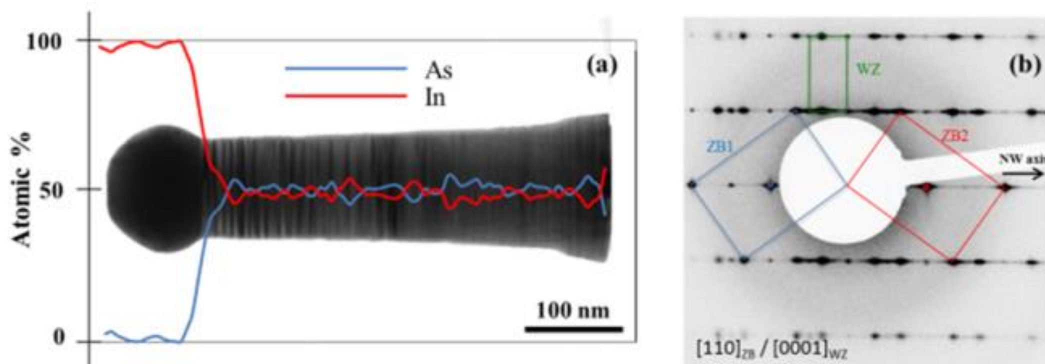

Figure 5.11. Bright field TEM image with superimposed EDX line profile of SC InAs NW grown for t_{growth} =70 min with F=0.75 (P_{TMIn}=0.40 Torr and P_{TBAs}=0.30 Torr). (b) Diffraction pattern showing the presence of both WZ and ZB structures. Figures are adapted from Ref.[73].

The In droplet located at the NW tip is clearly visible in the TEM image. EDX line profile superimposed to this bright-field image along the axial direction of the NW illustrates the composition of the droplet at the NW tip to be 100% indium (red curve). The NW composition is 50% indium and 50% arsenic (blue curve), as expected for an InAs stoichiometry (the observed fluctuation around the 1:1 composition are smaller than the sensitivity of the measurement in case of line profile). A high density of defects (stacking faults) perpendicular to the growth direction of the NW is visible in the bright field image (Figure 5.11 (a)). The diffraction pattern collected on the same NW (Figure 5.11(b)) shows the superposition of several lattices. We have a pattern corresponding to the [2-1-10]$_{WZ}$ zone axis of the WZ structure (highlighted in green) superimposed to one pattern corresponding to the [110]$_{ZB}$ zone axis pattern of the ZB structure (ZB1 highlighted in blue), together with its twin (ZB2 highlighted in red). The strong streaking along (111)$_{ZB}$ (or (0001)$_{WZ}$) indicates a disordered stacking of ZB and WZ segments along the entire NW.

5.10 Comparison between CF and SC NW growth mechanisms

5.10.1 Requirement of different growth parameters

The most important growth parameter for the formation of CF or SC InAs NWs is the line pressure ratio ($F= P_{TBAs}/ P_{TMIn}$). InAs NWs grow by CF mechanism when $F\geq1$ while SC growth of InAs NWs occurs for $F<1$. In other words, CF InAs NW growth requires As-rich growth conditions while In-rich growth conditions are necessary for the growth of SC NWs. The axial growth rate of CF InAs NWs is found to be proportional to $(P_{TMIn} P_{TBAs})^{1/2}$ so that an increase of both fluxes by a factor 2 leads to a twice as fast growth rate. On the other hand, the SC InAs NW axial growth rate was found to be linearly dependent on P_{TBAs} which is typical for the self-catalyzed growth.

The CF NW growth is a diffusion-limited growth process which takes place when a high diffusion flux of III adatoms is available from the substrate and sidewalls towards the NW top. Since diffusion is a thermally activated process, CF NW growth requires high growth temperatures. In contrary, low temperature is preferred for SC NWs which ensures the stability of In droplet.

5.10.2 Different growth rates for CF and SC NWs

Figure 5.12(a) and (b) show the plot of dependence of NW radius and length versus growth time for CF InAs NWs grown at 400°C with F=15. Figure 5.12(c) and (d) show the plot of dependence of NW radius and length vs growth time for SC InAs NWs grown at 400 °C with F=0.75.

From the plot of R_{NW} vs t_{growth}, it is possible to estimate the radial growth rate. The radial growth rate (G_R) of CF InAs NWs is found to be 2.53 nm/min (see Figure 5.12(a)) while G_R=1.58 nm/min for SC InAs NWs (see Figure 5.12(b)). The non-negligible radial growth rate in both the cases is due to low growth temperature (400 °C). The low temperature reduces the diffusion length of In adatoms and enhances radial growth.

The axial growth rate (G_L) of SC NWs (see Figure 5.12(d)) is much greater than the CF NWs (see Figure 5.12(c)).In particular, we found G_L =7 nm/min for SC InAs NWs while it is only 1.0 nm/min for CF InAs NWs. The enhanced axial growth rate of the SC NWs can be explained by the presence of the catalyst at the NW tip which acts as an efficient sink of the growth species as compared to the CF NWs.

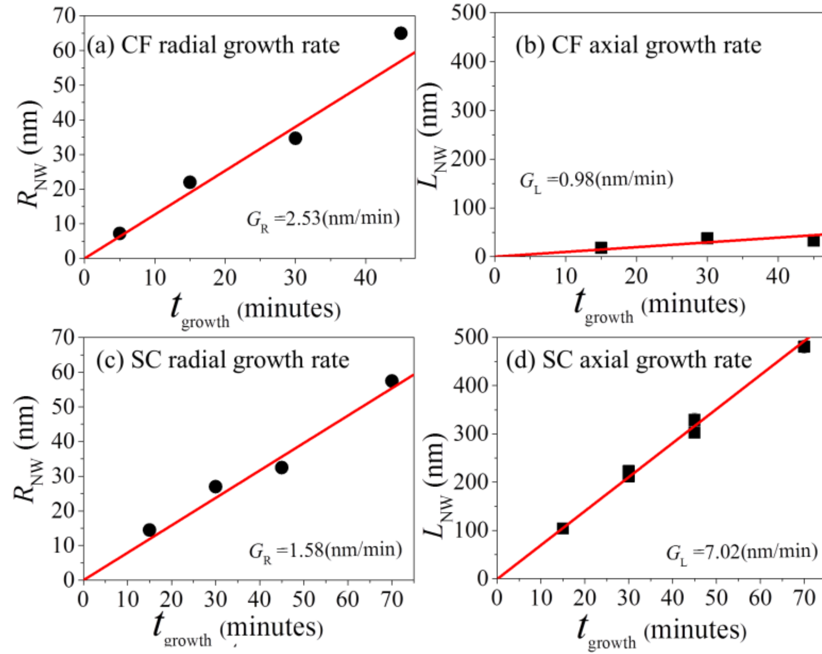

Figure 5.12. CF InAs NW (a) radius and (b) length as a function of growth time at 400 °C and *F*=15. SC InAs NW (c) radius and (b) length as a function of growth time at 400 °C and *F*=0.75.

5.11 Chapter summary

In this chapter, we have demonstrated the nucleation and growth of SC InAs NWs on Si (111) substrates. Appropriate choice of the growth parameters lead to In-rich conditions such that the NWs nucleate from an In droplet. As a consequence of more In atoms arriving to the droplet relative to As, the In droplet is preserved and the VLS condition for a continuous NW growth is maintained. Moreover, we found that SC InAs NWs continue to nucleate on Si (111) substrate throughout the growth thereby broadening the NW length distribution. The presented observations were accurately described by a theoretical growth model of SC III-V NWs incorporating specific features of nucleation which yielded quantitative estimates of all relevant growth parameters.

6 InAs-GaAs NW heterostructures

This chapter is dedicated to the Au-assisted growth of InAs/GaAs, GaAs/InAs and InAs/GaAs/InAs axial NW heterostructures. While GaAs easily grows straight on InAs, growth of InAs on GaAs results in kinked morphology.According to previous reports [36], kinking occurs because the Au NP prefers to remain in contact with GaAs as Au/GaAs surface energy is lower than for Au/InAs. Kinking can be inhibited by using graded interfaces [38] but to obtain heterostructures with sharp interfaces other strategies must be utilized. We show that straight InAs segments can be grown on GaAs by tuning the group III/Au ratios in the initial NPs before the GaAs growth. The experimental results demonstrate that the catalyst composition, rather than other growth parameters, strongly affects the growth mode and the resulting NW morphology. The observed trend has been discussed within a model by relating the droplet stability on the NW tips and the group III concentration. This chapter includes content from: V. Zannier, D. Ercolani, U. P. Gomes, J. David, M. Gemmi, V. G. Dubrovskii and L. Sorba, Nano Letters, 10.1021/acs.nanolett.6b03524, (2016).

6.1 GaAs/InAs heterostructured NWs

Figure 6.1 shows the growth protocol developed for the GaAs/InAs heterostructured NWs on InAs(111)B substrates, along with the corresponding SEM images of the NWs obtained at different stages, marked with the respective coloured dots. The top bars in Figure 6.1(a) indicate when and which precursors are switched on and off. The Au NPs were obtained by thermal annealing of 0.5 nm Au film at 500 °C for 20 min in As flux

(P_{TBAs}=1.0 Torr). After annealing, the temperature was ramped down to 410 °C. Subsequently, InAs NWs were grown for 5 min at 410 °C, followed by a 10 min temperature ramp up (+50 °C) while growing InAs with P_{TMIn}= 1.6 Torr and P_{TBAs}= 3.6 Torr. Figure 6.1(b) shows vertical and well-oriented InAs NWs obtained after this step (green dot). The growth of the GaAs segments on top of these InAs NWs was performed directly by switching from TMIn to TEGa and ramping up the growth temperature by ΔT while growing for 10 min with P_{TEGa}= 0.7 and P_{TBAs}= 1.1 Torr. Such a step was necessary, as the optimal temperature window for the growth of GaAs NWs is higher than that for the growth of InAs NWs. Various temperature ramps with ΔT between 20 and 100 °C were investigated. Figure 6.1(c) and (d) show the typical GaAs/InAs NWs obtained with ΔT of 50 °C (blue dot) and 70 °C (pink dot), respectively. For all ΔT investigated, straight axial GaAs/InAs NW heterostructures were obtained. However, along with axial GaAs growth there was a significant lateral growth of GaAs on the InAs sidewalls.

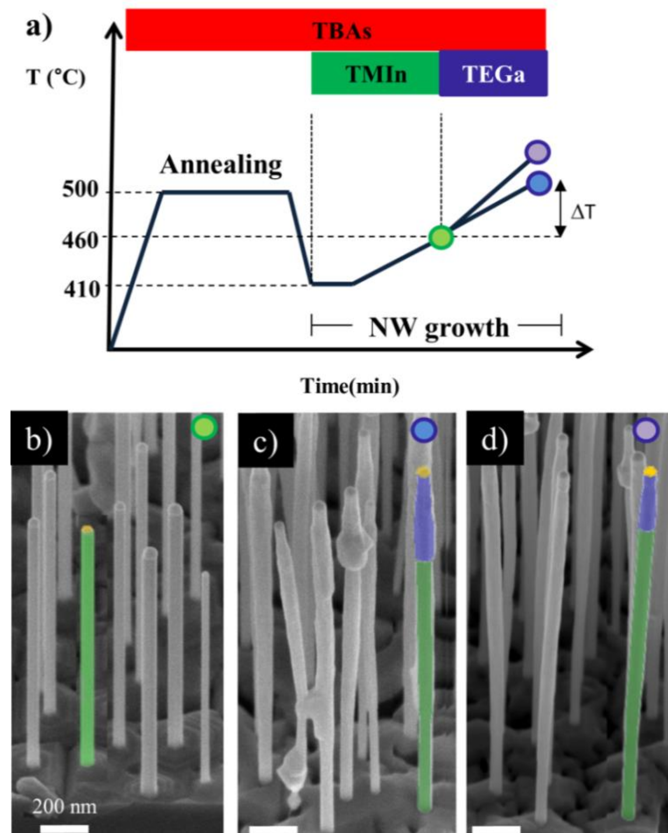

Figure 6.1.(a) Growth protocol for GaAs/InAs NW heterostructures on InAs(111)B substrates with (b-d) showing the corresponding 45°-tilted SEM images of NWs obtained at different stages indicated by coloured dots. The InAs stems are highlighted in green and the GaAs segments in blue. Figures are adapted from Ref.[171].

The lateral growth of GaAs was reduced with increasing the temperature ramp from ΔT=50 °C to 70 °C, as seen from comparing the NW morphologies in Figure 6.1(c) with ΔT of 50 °C and (d) with ΔT of 70 °C. However, if the ramp is too high (ΔT ≥ 100 °C) InAs starts to desorb from the stems and the NW morphology is degraded. In order to suppress lateral GaAs growth without damaging the NWs, InAs NWs were grown with higher density which was obtained by annealing the Au film at lower temperatures. In fact, by increasing the NW density, the lateral growth can be completely suppressed by the shadowing effect. By decreasing the annealing temperature to 450 °C, a fourfold increase in the NP density was obtained. The subsequent growth of InAs followed by 5 min GaAs growth with a ΔT of 70 °C results in the heterostructured NWs shown in Figure 6.2(a).

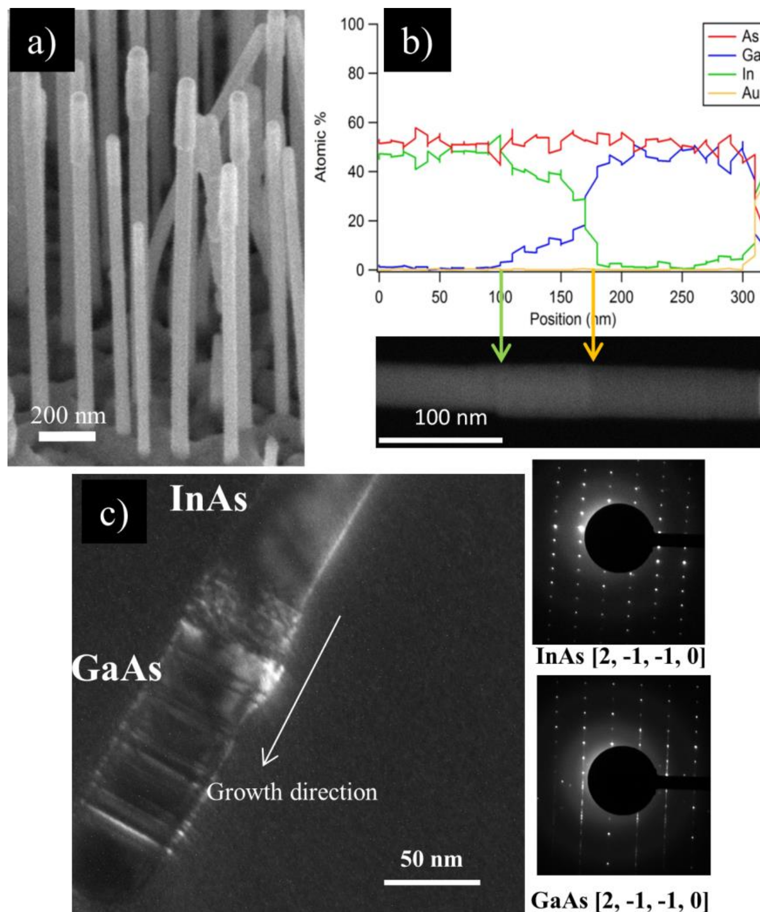

Figure 6.2. (a) SEM image (45°-tilted-view) of the high dense GaAs/InAs NWs grown on InAs(111)B. (b) EDX line profile (top) and STEM image (bottom) of an individual NW. The yellow arrow indicates the GaAs/InAs interface, while the green arrow indicates the end of the GaAs shell grown around the InAs NW. (c) TEM image with the SAED patterns of the two portions, taken along the [2, -1, -1, 0] zone axis. Figures are adapted from Ref.[171].

Figure 6.2(a) is a 45°-tilted SEM image of the as-grown sample showing reduced GaAs lateral growth. The GaAs segment length after 5 min of growth is around 140 nm. In Figure 6.2(b) and (c) the TEM analysis of individual NWs transferred onto the TEM grid are presented. Figure 6.2(b) shows a STEM image and the EDX elemental line profile of a single NW. The GaAs/InAs interface (indicated by the yellow arrow) is quite sharp. However, there is still a short (<100 nm) GaAs shell around the InAs NW in the proximity of the heterointerface (see the green arrow, which indicates its end). This shell is formed by lateral overgrowth around the core and can be explained by the model of Ref.[172], suggesting a sphere of "activated" Ga around the NP which is available for growing GaAs. From the length of the GaAs shell, the diffusion length of the "activated" Ga can be estimated at approximately 100 nm. Figure 6.2(c) shows the TEM image of the upper part of GaAs/InAs NW, together with the selected area electron diffraction (SAED) pattern of the two segments. Both InAs and GaAs show WZ crystal structure. InAs is almost free from structural defects, while GaAs crystal structure reveals several stacking faults randomly distributed along the whole segment. The NPs at the NW tips are composed of 38% of Au and 62% of In (atomic percent), while the Ga concentration is below the instrumental detection limit (~ 4%). Such negligible amount of Ga in the NPs have been previously reported where no measurable Ga were found after GaAs axial growth on InAs NWs with GaAs length ranging from 300 to 1000 nm [36].

In order to evaluate the changes in the chemical composition of the NPs as a function of the GaAs length, a series of samples were grown following the growth scheme depicted in Figure 6.3(a). InAs NWs were grown for 5 min at 410 °C plus 10 min ramping the temperature up to 460 °C with P_{TMIn}= 1.6 Torr and P_{TBAs}= 3.6 Torr. After the growth of InAs NWs, GaAs growth was grown with P_{TEGa}= 0.7 and P_{TBAs}= 1.1 Torr during the 5 min ramping the temperature up to 530 °C. After this step, GaAs growth was carried out for different times (t_{GaAs}) with the same line pressures. Figure 6.3(b) shows the SEM images of heterostructured NWs obtained at three different t_{GaAs} (5, 15, and 55 min).

Both length and diameter of the GaAs segment increase with t_{GaAs}. The NP composition on the tips of pure InAs NWs (t_{GaAs}=0) was Au/In 33/67. Such alloy NPs should be liquid at this growth temperature according to the Au-In phase diagram [173] and to previous reports on the Au-assisted InAs NW growth [52] suggesting VLS growth mechanism. As the GaAs segment growth is started, the amount of In in the NPs decreases and the amount of Ga slightly increases. It was previously reported that an addition of Ga into Au/In alloy NPs lowers their melting temperature [174], therefore

the NPs retain their liquid state and the growth mechanism does not change when In is switched to Ga.

In Figure 6.3(c) we plot the In/Au and the Ga/Au atomic percent ratios as a function of the GaAs growth duration t_{GaAs}. The amount of In drops from 67% to 40% in 15 min of GaAs growth (GaAs segment length around 450 nm). A further increase of the growth time does not appreciably change the amount of In, which is still around 30% after 95 min of growth (resulting in a ~1.7 μm long GaAs segment). On the other hand, Ga which was undetectable in the NPs before t_{GaAs}=15 min, reaches 12-16% atomic percent concentration after t_{GaAs}=55-95 min with segment length > 1 μm.

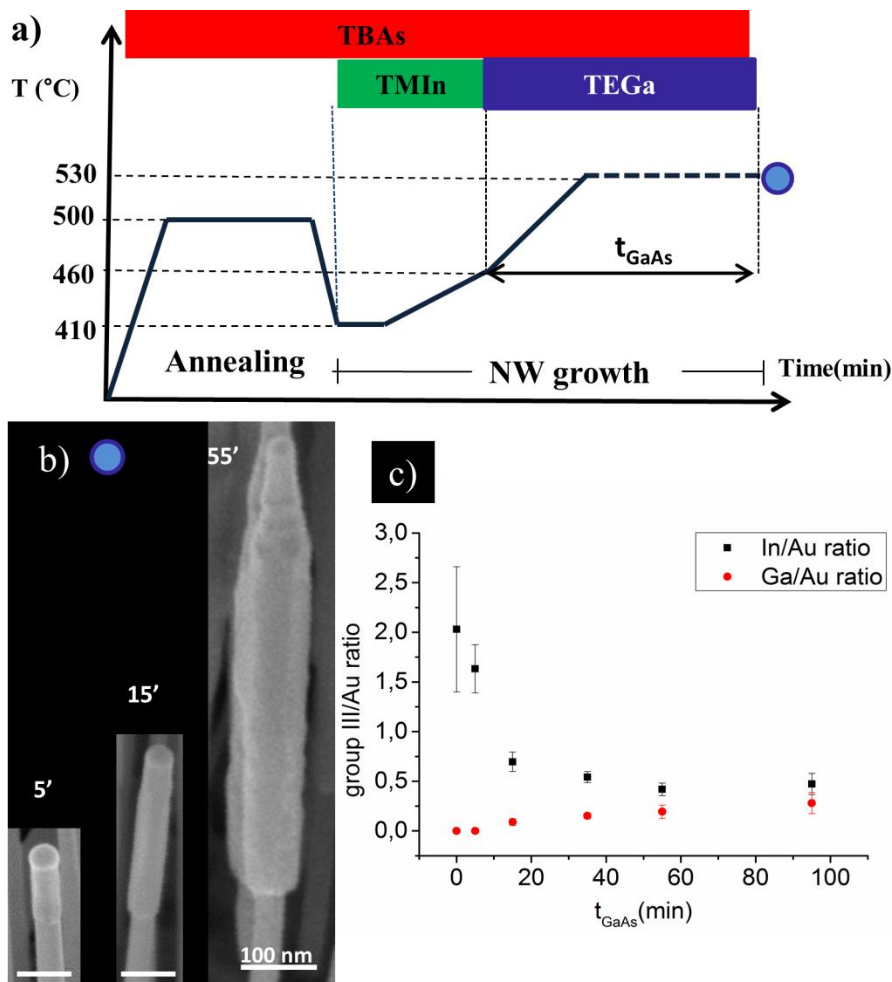

Figure 6.3. (a) Schematic diagram of the process developed for the growth of GaAs/InAs NWs with the GaAs part grown for variable times (t_{GaAs}). (b) 45° tilted SEM images of a portion of GaAs/InAs NWs obtained at different t_{GaAs} reported in the panel. (c) Plot of the NP composition (In/Au and Ga/Au ratios) as a function of t_{GaAs}. Figures are adapted from Ref.[171].

6.2 InAs/GaAs/InAs double-heterostructured NWs

The growth protocol used to grow InAs/GaAs/InAs double-heterostructured NWs on InAs(111)B substrates is shown in Figure 6.4(a). First, the GaAs/InAs heterostructured NWs are grown with different GaAs length by growing at different t_{GaAs}. After the growth of GaAs/InAs heterostructured NWs, InAs segment was grown during a 10 min ramp-down of the growth temperature (ΔT = -70°C). GaAs growth was conducted with P_{TEGa}= 0.7 and P_{TBAs}= 1.1 Torr and InAs with P_{TMIn}= 1.6 Torr and P_{TBAs}= 3.6 Torr.

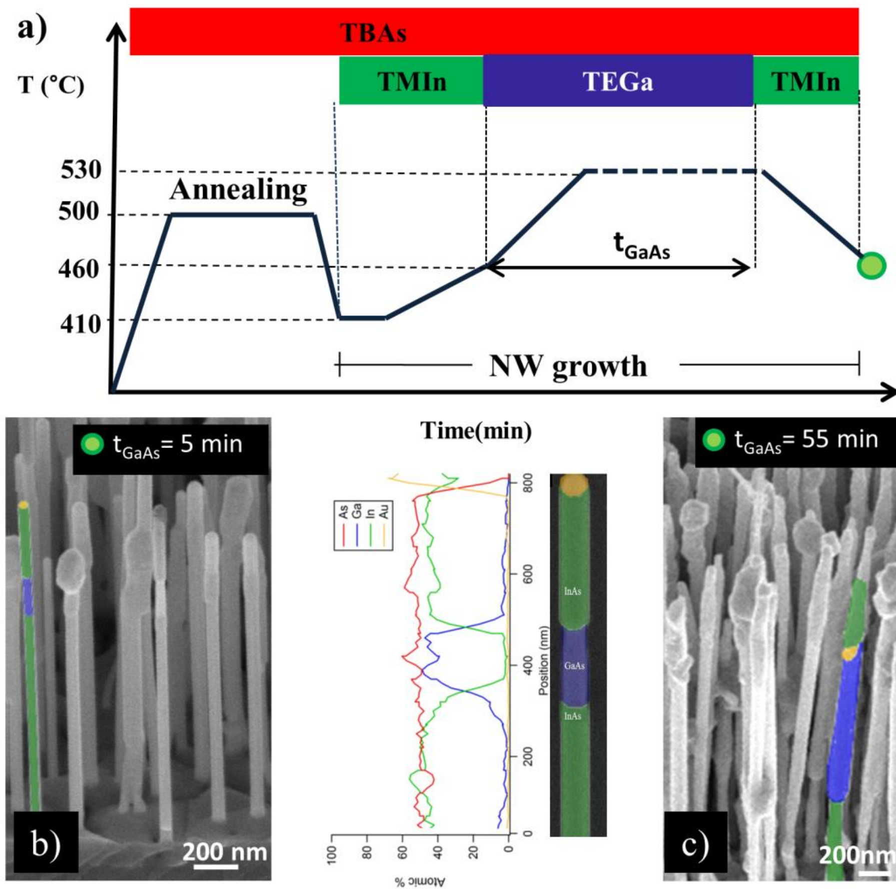

Figure 6.4. (a) Growth protocol for InAs/GaAs/InAs double-heterostructured NWs. (b) 45° tilted SEM image of InAs NWs grown on the GaAs/InAs stems with short GaAs segments (t_{GaAs} = 5 min). (c) EDX line profile of a straight InAs/GaAs/InAs double-heterostructured NW taken from the sample shown in (b). (d) 45° tilted SEM image of InAs NWs grown on the GaAs/InAs stems with longer GaAs segments (t_{GaAs} = 55 min). One representative NW is coloured with InAs shown in green, GaAs in blue and the NP in yellow. Figures are adapted from Ref.[171].

The InAs/GaAs/InAs double heterostructured NWs grew without kinking only on top of the shortest GaAs segments of GaAs/InAs NWs (t_{GaAs} = 5 min, the GaAs length about 140 nm). Figure 6.4(b) shows the SEM image of as-grown sample, where 75% of

InAs/GaAs/InAs double heterostructured NWs are straight. Figure 6.4(c) shows the EDX line profiles for As, In, Ga and Au elements along a single NW, where the two interfaces are easily identified. The InAs/GaAs interface is sharper than the GaAs/InAs one, as evidenced by the slope of the single-element lines and the length of the In/Ga mixed regions (around 100 for GaAs/InAs and less than 50 nm for InAs/GaAs). This result confirms a higher affinity of In for Au with respect to Ga [38,175–178].

For longer GaAs segments, the InAs segments tend to grow downward and produce kinked geometries. Only 15% of the double NW heterostructures obtained with t_{GaAs} = 55 min are straight, as visible in Figure 6.4(d).

The main difference between InAs/GaAs/InAs double heterostructured NWs with short (t_{GaAs} = 5 min) and long (t_{GaAs} = 55 min) GaAs segments is the amount of group III element stored in the NP on top of the GaAs segment. According to Figure 6.3(c), at t_{GaAs} = 5 min, the NP is an In/Au alloy with a high In percentage (In/Au=1.63) and without any Ga. At t_{GaAs} = 55 min, the alloy is ternary In/Ga/Au but the total group III to Au ratio is only 0.61. The InAs segments grow straight on short GaAs segments from NPs with high group III percentage and kink on longer GaAs segments with lower group III percentage. Therefore, higher group III content in the NP seems to favour straight heterostructured geometry. Such behavior is further confirmed by growth interruption (GI) tests.

In order to test if a growth interruption between GaAs and InAs has any effect on kinking, GaAs/InAs heterostructured NWs with t_{GaAs} of 5 min was grown (see Figure 6.3(a)) and then two different GI tests were performed. Figure 6.5 (a) shows the growth protocol and the resulting NWs obtained in the two cases are shown in Figure 6.5(b) and (c).

In the first interruption test (blue dot), we performed the GI keeping the GaAs/InAs NWs under As flux (P_{TBAs}= 3.6 Torr) for 3 min at fixed temperature (the highest GaAs growth temperature: 530 °C). In the second GI test (pink dot), instead, we performed the growth interruption by cooling down (-120 °C) under As flux (P_{TBAs}= 3.6 Torr) before growing the second InAs segment.

The growth interruption at fixed temperature does not affect the NP chemical composition of the GaAs/InAs NWs obtained with and without GI. EDX measurements reveal 63% of In and 37% of Au (In/Au=1.70). The following InAs growth results in straight InAs/GaAs/InAs NW heterostructures (see Figure 6.5(b)), as similar to NWs grown without any GI (see Figure 6.4(b)). Conversely, the GI with As flux and a temperature ramp of -120 °C reduces the group III/Au ratio of the NPs from 1.70 to

0.53. Consequently, the InAs growth on top of GaAs results in kinked NW heterostructures (see Figure 6.5(c)).

These tests further confirm the correlation between NP composition (group III /Au ratio) and InAs growth mode. Indeed, by reducing the group III/Au ratio of the NPs before InAs growth the NWs kink, regardless of any other parameter (growth protocol, GaAs segment length, and temperature).

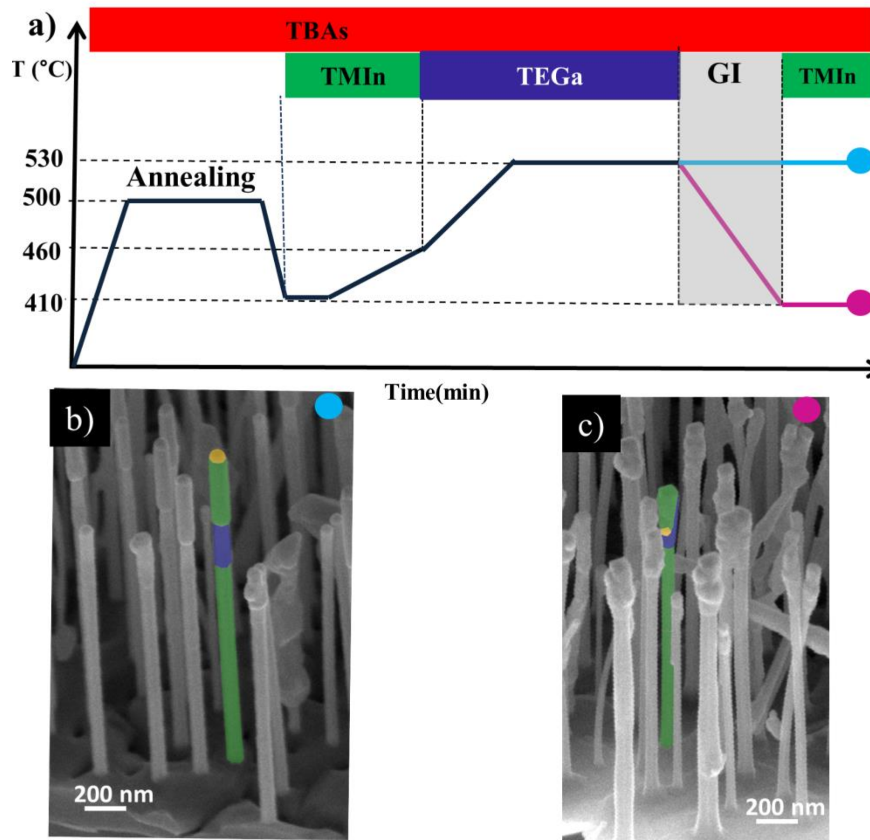

Figure 6.5. (a) Growth process for InAs/GaAs/InAs NWs with growth interruption (GI) between GaAs and InAs. (b and c) SEM images of the InAs/GaAs/InAs NW heterostructures resulting from the two different growth interruption protocols marked with the corresponding coloured dots in (a). Figures are adapted from Ref.[171].

6.3 InAs/GaAs heterostructured NWs

InAs/GaAs heterostructured NWs were grown on GaAs (111)B substrates using the growth protocol shown in Figure 6.6(a) The Au NPs were obtained by thermal annealing of a 0.1 nm Au film at ~ 550 °C for 20 min in As background (P_{TBAs}=1.0 Torr). GaAs NW growth was conducted at ~ 530 °C for 60 min with P_{TBAS}=1.1 Torr and P_{TEGa}=0.7 Torr. InAs NW growth was carried out for 5 min as the temperature was

ramped down to 480 °C with P_{TBAs}=3.6 Torr and P_{TMIn}=1.6 Torr.

Using this growth protocol, the InAs segments tend to grow downward and produce kinked geometries as shown in Figure 6.6(b) and this behaviour was found to be independent of the InAs growth temperature (lower, higher or equal to that of GaAs).

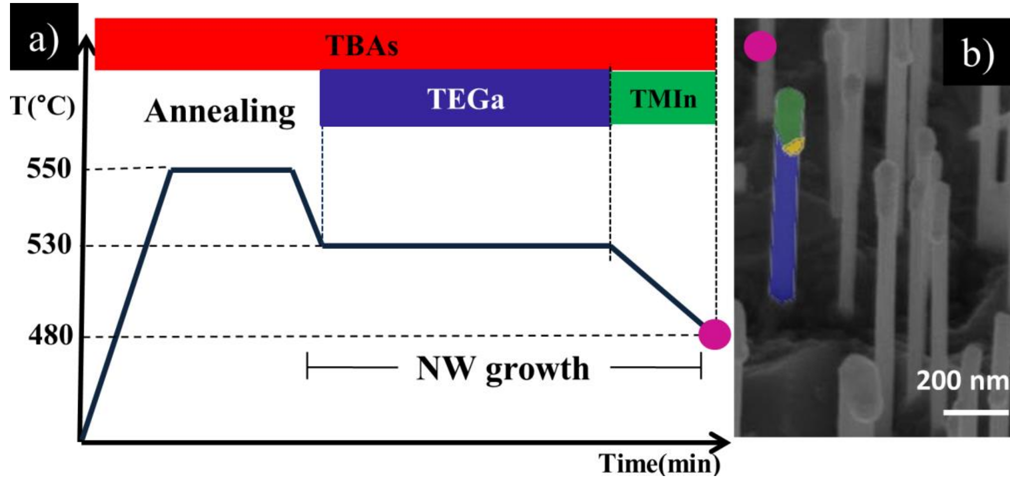

Figure 6.6. (a) Growth protocol for InAs/GaAs NWs on GaAs (111)B substrates. (b) SEM image of InAs/GaAs NWs. One representative NW is coloured with InAs shown in green, GaAs in blue and the NP in yellow. Figures are adapted from Ref.[171].

Since a high percentage of In in the NPs before the InAs growth favours the straight geometry of InAs segments on GaAs, the GaAs NWs were grown from Au/In (or Au/In/Ga) NPs. This was realized by In predeposition (P_{TMIn}=0.3 Torr) immediately after annealing of 0.1 nm Au film on GaAs(111)B substrates. An optimum predeposition time of 10 seconds was enough to form the Au/In alloys but at the same time avoid any pure In droplets nucleation on the surface. Figure 6.7(a) shows the SEM image of the surface after this treatment, along with the typical EDX spectrum acquired from a single NP. Unfortunately, in this case it is not possible to decouple the Ga signals originating from the NP and GaAs substrate and hence the precise composition of the initial NP cannot be determined. However, the presence of In signal in the EDX spectra confirms the In alloying with Au.

After the In predeposition, GaAs NWs were grown following the standard protocol i.e at ~ 530 °C for 60 min with P_{TBAs}=1.1 Torr and P_{TEGa}=0.7 Torr. The resulting NWs shown in Figure 6.7(b) are similar in morphology and crystal structure to the standard GaAs NWs grown without any In predeposition. They are uniformly oriented, slightly tapered, show WZ crystal structure with randomly distributed stacking faults (see Figure 6.7(c)). However, the chemical composition of the NPs on their tips is different. After

60 min of GaAs growth, Ga/Au composition in the NPs was 45/55 (with no In detected), compared to 33/67 Ga/Au composition in the standard case without In predeposition. This suggests that the presence of In in the Au NPs before the GaAs growth has increased the solubility of Ga into Au at a later growth stage.

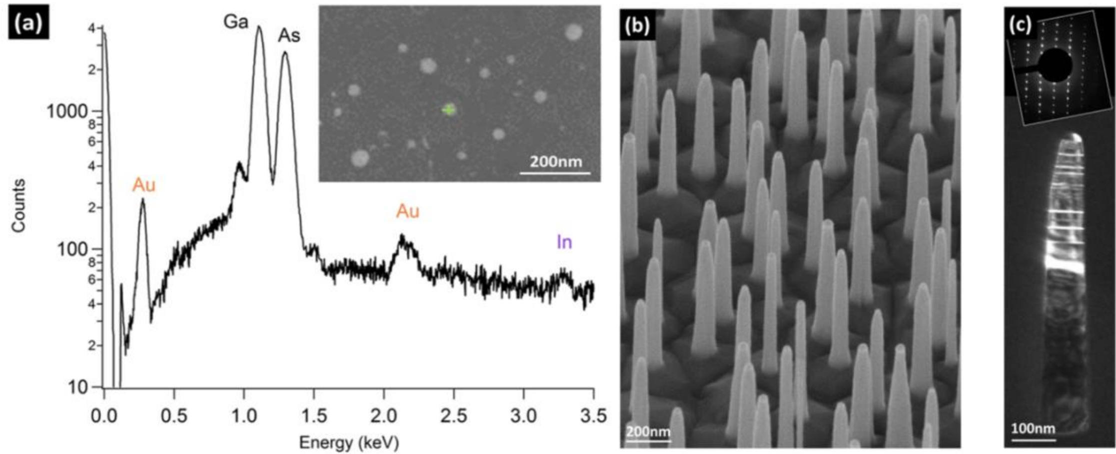

Figure 6.7. (a) Plan-view SEM image of a GaAs (111)B substrate obtained after annealing a 0.1 nm thick Au layer and 10 s of In predeposition. EDX spectrum is taken from the NP marked with green cross. (b) 45°-tilted SEM image of GaAs NWs grown for 60 min. (c) TEM image of a single GaAs NW and the corresponding SAED pattern along [2,-1,-1,0] zone axis. Figures are adapted from Ref.[171].

The growth of InAs segments on top of GaAs NWs obtained with the In predeposition produces straight InAs/GaAs NW heterostructures with a high yield (85%), regardless of the InAs growth temperature as shown in Figure 6.8.

Figure 6.8(a) shows the NWs obtained after 10 min of InAs growth with the temperature ramp-down (ΔT=-50 °C). The InAs and GaAs segments are clearly visible in the SEM image of Figure 6.8(a) and in the EDX profile of Figure 6.8(b). The TEM image in Figure 6.8(c) demonstrates high quality WZ structure of the InAs segment, while the WZ GaAs part contains many stacking faults, as was earlier seen in the reversed GaAs/InAs NW heterostructures. This is not surprising because the structure of III-V NWs depends on the growth parameters that are kept the same for both InAs and GaAs in the two growth sequences and hence the crystal quality should not depend on the growth sequence [3,52].

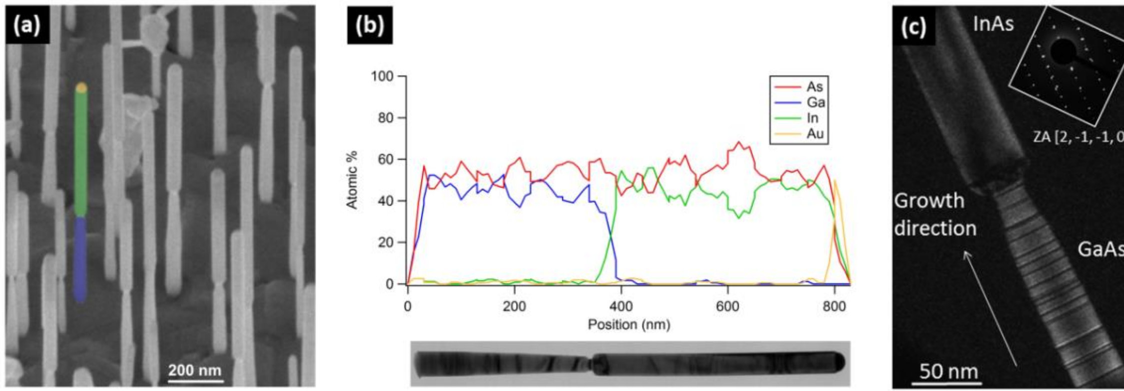

Figure 6.8. (a) 45°-tilted SEM image of as-grown NWs on GaAs(111)B substrates showing straight growth of InAs segments on top of GaAs NWs obtained with the In predeposition. In the coloured NW, the GaAs portion is shown in blue and the InAs portion in green. (b) EDX line profile of the elements along the growth axis of the NW displayed below taken from sample shown in (a). (c) TEM image and the corresponding SAED pattern along [2,-1,-1,0] zone axis of a NW portion close to the InAs/GaAs heterointerface . Figures are adapted from Ref.[171].

6.4 Comparison of growth modes

The growth modes of InAs segments on GaAs NWs obtained with and without the In predeposition can be compared with the results on the InAs/GaAs/InAs double heterostructures as a function of the NP composition. Ga-rich Ga/Au alloy NPs on top of GaAs NWs obtained with the In predeposition (Ga/Au ratio = 0.82) yield straight InAs/GaAs heterostructures. Straight double heterostructured InAs growth is also observed on top of GaAs/InAs NWs with a high initial In content in the In/Au NPs (In/Au ratio = 1.63). Conversely, InAs grows downward on the Au-seeded GaAs NWs with a lower Ga content in their Ga/Au NPs (Ga/Au ratio = 0.49), and on top of GaAs/InAs NW heterostructures with a lower group III content in their NPs [(In+Ga)/Au ratio < 0.79]. A more detailed experimental data on the InAs growth modes on GaAs versus the initial NP composition are given in Table 6.4. There is no problem growing straight GaAs segments on top of InAs, where the initial In content in the In/Au NPs is always very high (average In/Au ratio = 2). Therefore, straight Au-catalyzed VLS growth of InAs/GaAs NW heterostructures systematically requires high group III/Au ratios in the initial NPs (with a minimum of 0.82 according to the data of Table 6.4), and actually regardless of the In to Ga composition inside them. This property is always fulfilled for GaAs on InAs but requires special care for InAs on GaAs. Similar effects have been observed in other systems: prefilling of the Au NP with In prior to growth has been demonstrated very effective to control the growth

direction of InP NWs and prevent kinking [179]. Likewise, an excess of Ga in the Au particle has resulted essential to grow straight GaP on top of Si NWs[180].

Table 6.4. Summary of the experimental data on the InAs growth modes on GaAs at different conditions yielding different NP compositions. [171]

t_{GaAs} (min)	**Initial NP composition**			**Straight InAs growth**
	Ga/Au	In/Au	III/Au	
InAs/GaAs/InAs with direct Ga to In switch				
0	0	2.0	2.0	Yes
5	0	1.63	1.63	Yes
15	0.09	0.70	0.79	No
35	0.15	0.54	0.69	No
55	0.19	0.42	0.61	No
95	0.28	0.47	0.75	No
InAs/GaAs/InAs with GI at fixed temperature				
5	0	1.70	1.70	Yes
InAs/GaAs/InAs with GI lowering temperature				
5	0	0.53	0.53	No
InAs/GaAs single heterostructures with In predeposition				
60	0.82	0	0.82	Yes
InAs/GaAs single heterostructures without In predeposition				
60	0.49	0	0.49	No

To understand why high group III content in the initial NPs promotes straight NW growth, we use the Nebol'sin-Shchetinin model for the NP stability on the NW top [174], which is a simplified version of a more general condition considered later in Refs. [132,181]. The model states that stable VLS growth occurs when

$$\frac{\gamma_{SV}}{\gamma_{LV}} < \sin\beta - \cos\beta \quad . \qquad 6.4.1$$

This inequality connects the solid-vapour surface energy of the NW sidewalls, γ_{SV} and

the liquid-vapor surface energy of the NP, γ_{LV} with the contact angle of the NP, β and is independent of the NW radius. Condition given by Eq. 6.4.1 applies for straight NW sidewalls and planar growth interface, which is indeed the case for WZ III-V NWs [182] without a truncated edge [116]. When the inequality given by Eq. 6.4.1 is inverted, the NP slides downward and produces kinked geometries. Very importantly, in this model the NP stability is not determined by the solid-vapor or liquid-vapor surface energy alone, but rather by their ratio, and does not depend on the solid-liquid surface energy [181].

Neglecting the As concentration, the droplet volume is given by

$$\Omega(N_{Au}+N_3)=(\pi R^3/3)f(\beta) \qquad 6.4.2$$

with $f(\beta)=(1-\cos\beta)(2+\cos\beta)/[1+\cos\beta)\sin\beta]$. Here, the left hand side is the volume of the liquid NP occupied by N_{Au} atoms of Au and $N_3=N_{In}+N_{Ga}$ atoms of the group III elements (N_{In} atoms of In and N_{Ga} atoms of Ga), with Ω as the elementary volume in the liquid phase. The right hand side is the geometrical volume of a spherical cap having the base radius R and contact angle β. The group III/Au ratio equals N_3/N_{Au}.

In our simple model, we consider only axial growth via the VLS mechanism, without subsequent vapor-solid lateral overgrowth of the sidewalls which occurs after the growth direction is decided. We assume that the NP size is pre-determined by its initial group III content (at N_{Au} =constant) and does not change much after switching the group III fluxes to grow a heterostructure. In this case, the NW radius can be treated as time-independent and then any two group III/Au ratios N_3/N_{Au} and N_3^0/N_{Au} are related through the corresponding contact angles of the NPs β and β_0 as

$$\frac{N_3}{N_{Au}}=\left(1+\frac{N_3^0}{N_{Au}}\right)\frac{f(\beta)}{f(\beta_0)}-1. \qquad 6.4.3$$

Measuring the contact angle β_0 for a NP with the known N_3^0/N_{Au} gives the dependence of the group III/Au ratio on the contact angle within the entire range of compositions and with no free parameters. From Eq. 6.4.3, we can then relate ($\sin\beta-\cos\beta$) to the group III/Au ratio. This dependence is shown by line in Figure 6.9(a) for the measured $\beta_0=118^o$ at $N_3^0/N_{Au}=1.63$ [Figure 6.9(b)]. The curve shows how ($\sin\beta-\cos\beta$) increases with the group III/Au ratio, because the contact angle of the NP is larger for higher group III content.

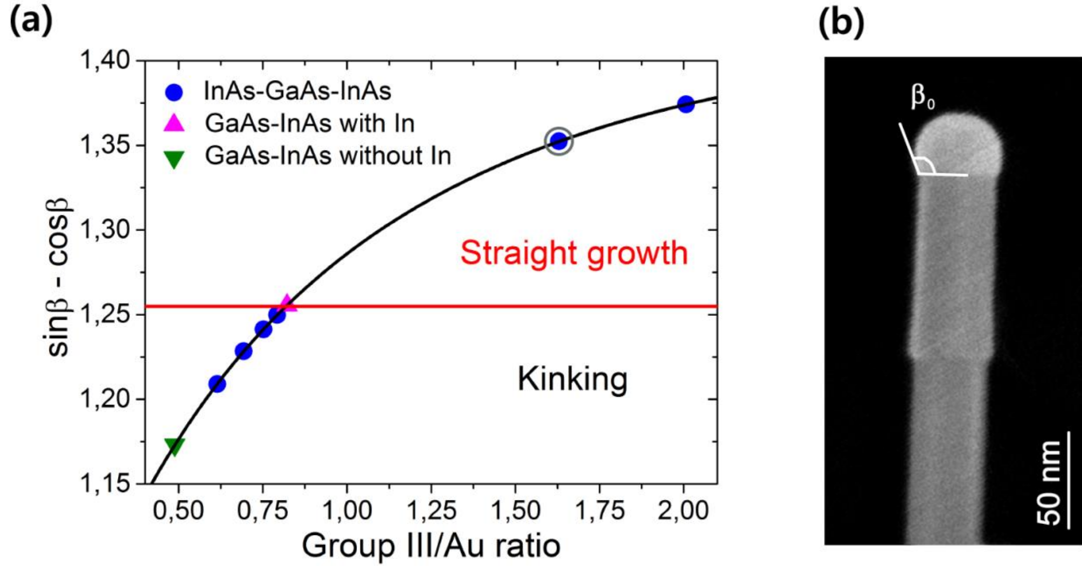

Figure 6.9. (a) Graph of $(\sin\beta - \cos\beta)$ versus the group III/Au ratio obtained from Eqs. 6.4.1 and 6.4.3 for $\beta_0 = 118^{\circ}$ at N_3/N_{Au} = 1.63, as shown in (b). Horizontal line separates the domains of straight growth of InAs on GaAs and kinking. Symbols represent the data given in Table 6.4 and fall exactly within the correct growth domains. Open circle in (a) shows the point corresponding to the measured contact angle and group III/Au ratio of GaAs/InAs NWs (t_{GaAs} = 5 min) as the one depicted in (b). Figures are adapted from Ref.[171].

Now, the NP stability on the NW top is entirely determined by the surface energy ratio γ_{SV}/γ_{LV} (see Eq. 6.4.2). The liquid-vapor energy γ_{LV} generally depends on the NP composition and is often taken as a linear interpolation between the surface energies of pure liquids [183], assuming a spatially homogeneous alloy. In our case, it depends on both N_{In} and N_{Ga}, which vary in opposite directions. However, In is the lowest energy liquid metal [184] and, if present in the NP, should accumulate at the surface to minimize the surface energy. Our data confirm a much higher In affinity for Au compared to Ga, which is why its initial concentration in the NPs even before growing InAs on GaAs/InAs NWs is systematically larger than Ga. Therefore, we additionally can assume that switching on the In flux to grow InAs on GaAs quickly replaces Ga to In inside the NP. Both considerations lead to the assumption of a composition-independent $\gamma_{LV} = \gamma_{In}$ for pure In liquid.

Based on the data of Ref. [184], corrected for the average growth temperature of InAs [87], the γ_{LV} value equals 0.449 J/m^2. If we take the published value for the lowest energy vertical sidewalls of pure WZ InAs NWs, $\gamma_{SV} = \gamma_{InAs}$ = 0.576 J/m^2 (Refs.[185,186]), the horizontal line in Figure 6.9 yields exactly the experimentally

observed domains for straight InAs growth at high group III/Au ratios and kinking at low group III/Au ratios. This picture should not be significantly different for InGaAs or even pure GaAs NWs. Indeed, the solid-vapour surface energy of GaAs is only slightly larger (γ_{GaAs} = 0.693 J/m^2 according to Ref.[187]) and can be compensated by simultaneously increasing γ_{LV} due to the surface accumulation of some Ga when growing GaAs.

Finally, the observed increase of Ga concentration in the NP with In predeposition can be understood from the same model. Alloying In with Au increases the initial group III content in the droplet. In steady state growth with a fixed droplet volume, In will be replaced by Ga at a fixed N_3 in the course of growth and hence the final Ga content will be larger than without In predeposition.

6.5 Chapter summary

In this chapter, the growth of different heterostructures by using a combination of GaAs and InAs semiconductors has been described. In particular, the growth of axial InAs/GaAs, GaAs/InAs and InAs/GaAs/InAs heterostructured NWs is presented. The well-known problem of growing InAs on top of GaAs is solved by choosing the conditions that yield high group III content in the Au NPs. This was achieved by either growing short GaAs segments in InAs/GaAs/InAs double heterostructures or pre-depositing In before growth of GaAs in InAs/GaAs single heterostructures. The observed trend is related to the droplet stability on the NW top, favoured at large contact angles and hence group III concentrations.

7 InAs/GaSb NW heterostructures

InAs and GaSb are approximately lattice matched material systems with lattice parameter of about 6.1 Å and bandgaps of 0.36 eV and 0.73 eV, respectively. This allows the growth of InAs/GaSb heterojunctions without any misfit dislocations and a type II broken band alignment with the bottom of conduction band of InAs lines up below the top of the valence band of GaSb, with a gap of about 150 meV [188]. This band line up gives rise to band-to-band tunneling and spatially separated electrons and holes which makes InAs/GaSb heterojunctions useful for interesting devices like tunnel field effect transistors [189] and investigation of phenomenon like electron–hole interactions [190], and exciton and spin-physics [191]. In this chapter, we report the growth of radial broken-gap InAs/GaSb core-shell heterostructured NWs on silicon substrates using the CF NW growth approach. After optimizing the core-shell morphology, the NWs are used for device fabrication. The creation of a radial broken-gap junction has been demonstrated through the observation of negative differential resistance (NDR) that can be tuned by the changing the backgate voltage. This chapter includes content from: M. Rocci, F. Rossella, U. P. Gomes, V. Zannier, F. Rossi, D. Ercolani, L. Sorba, F. Beltram and S. Roddaro, submitted to Nano Letters, (2016).

7.1 InAs/GaSb heterostructured NW growth protocol

The growth protocol of InAs/GaSb core-shell heterostructured NWs is shown in Figure 7.1. The InAs NWs were grown by using the optimized two-step growth protocol as discussed in chapter 4. After annealing at 790 °C under a TBAs line pressure of 1.00

Torr for 15 min, the temperature was ramped down to 420 °C. Subsequently, InAs NWs were grown using the two-step growth protocol (as described in details in chapter 4). It consists of a 10 min LT nucleation step (P_{TMIn}=0.30 Torr, P_{TBAs}= 3.00 Torr, 420 °C), 10 min ramp (P_{TMIn}=0.30 Torr, P_{TBAs}=3.00 Torr) to the HT growth step (P_{TMIn}=0.20 Torr, P_{TBAs}=3.00 Torr) continuing for a growth time of 90 min at growth temperature of 520 °C. After the growth of CF InAs NW cores, GaSb shell was grown with P_{TMSb}=0.6 Torr and P_{TEGa}=0.70 Torr at the same temperature of InAs core for a growth time of t_{GaSb}. After the NW growth the sample was linearly cooled down in Sb flux from 0.6 Torr to 0 in 3 min.

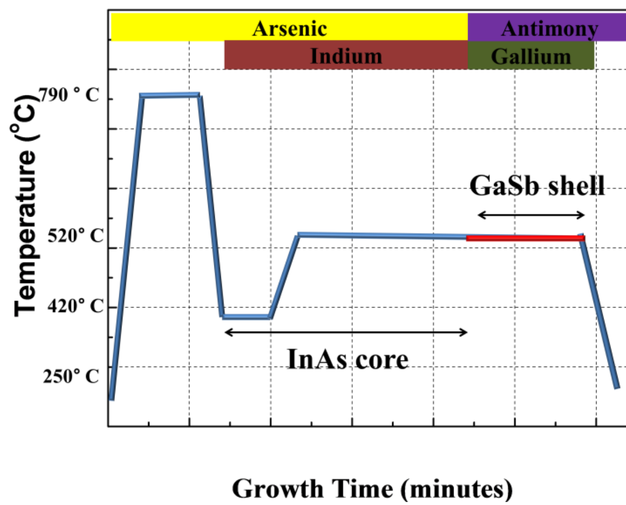

Figure 7.1. (a) Schematic of the growth protocol to grow InAs/GaSb core shell NWs. The InAs core is grown using the two stage growth protocol, and then GaSb shell growth is conducted at the same growth temperature.

7.2 Influence of different precursors on GaSb shell growth

The CBE system is equipped with two different Antimony MO precursors: Tri-methyl Antimony (TMSb) and trisdimethylaminoantimony (TDMASb). The decomposition temperature of TMSb is very high, therefore the precursor is pre-cracked in a HT injector to make elemental Sb available for NW growth. On the other hand, TDMASb is pyrolyzed into elemental Sb on the heated substrate as it decomposes at a much lower temperature [192]. The Gallium MO source used for GaSb growth is TEGa and elemental Ga is obtained by its pyrolysis at the heated substrate.

The atomic flux of Sb ($\O_{Sb}$) is inversely proportional to the square root of molecular masses ($\O_{Sb} \propto P_{MO}/\sqrt{M_{MO}}$). Since, M_{TMSb} (=166.86) is less than M_{TDMASb} (=253.98), TMSb gives higher flux of Sb compared to TDMASb for identical MO line pressures

(provided the injector geometries are identical and 100% pyrolysis of the MOs). Therefore, in order to compare the growth of InAs/GaSb core-shell NWs using these two precursors, the line pressures must be adjusted accordingly. The atomic flux of Sb is similar for the two precursors when P_{TDMASb} =0.74 Torr and P_{TMSb}=0.60 Torr and hence used for GaSb shell growth on InAs cores using the growth protocol depicted in Figure 7.1 with P_{TEGa} kept fixed at 0.70 Torr for t_{GaSb}=30 min at 520 °C.

Figure 7.2(a) shows SEM micrographs of CF InAs NWs and they have an average diameter of ~60 nm and an average length of ~2000 nm. The average diameter of the NWs increased to ~110 nm and the average length was ~2100 nm after 30 min of GaSb growth using TMSb (see Figure 7.2(b)). The measured GaSb shell thickness was therefore ~25 nm.

When GaSb shell was grown with TDMASb, the average diameter and length of the NWs did not increase (see Figure 7.2(c)) suggesting that GaSb shell did not grow by employing TDMASb as precursor. Extensive investigation of GaSb shell grown by varying growth parameters using TDMASb never revealed any change in NW morphology. In particular, no morphological change with respect to InAs cores was observed for different GaSb growth temperatures (ΔT=-70,-20, 0, and +50 °C), GaSb growth times (15-60 min) and line pressure ratios (P_{TDMASb}/ P_{TEGa} =0.74/0.70, 0.37/0.22, and 0.75/0.45).

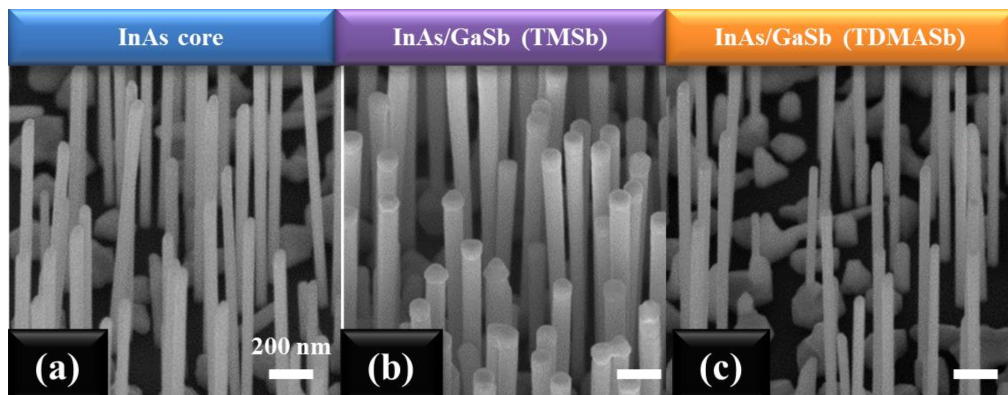

Figure 7.2. 45° tilted SEM micrographs of (a) core InAs NWs, (b) InAs/GaSb core–shell NWs grown using TMSb with P_{TMSb}=0.6 Torr and P_{TEGa}=0.70 Torr (c) InAs/GaSb core–shell NWs grown using TDMASb with P_{TMSb}=0.74 Torr and P_{TEGa}=0.70 Torr. The shell growth time was 30 min at 520 °C (ΔT=0).

No growth of GaSb shell by using TDMASb for all growth conditions is likely due to the pre-reactions between TEGa and TDMASb precursors [193] and/or due to etching effects [194] which prevent GaSb shell growth. On the other hand, these effects are not

reported for GaSb grown with TMSb [193]. The growth of InAs/GaSb core-shell NWs have been previously reported using elemental sources (Sb and Ga) in MBE [58] and MO sources (TMGa and TMSb) in MOCVD [56,57].

7.3 Influence of growth time on GaSb shell growth

Using the optimized precursor combination of TEGa and TMSb, the GaSb shell growth was investigated as a function of shell growth time. Figure 7.3(a) shows SEM micrograph of InAs NWs used as cores. The InAs NWs are non-tapered with an average length ~2000 nm and average diameter ~60 nm. The NW density is around 8 NWs/µm^2. Figure 7.3 (b)-(d) show InAs/GaSb heterostructured NWs grown by varying t_{GaSb} from 15-45 min. Figure 7.3(e) shows the plot of GaSb shell thickness (t) as a function of t_{GaSb}.

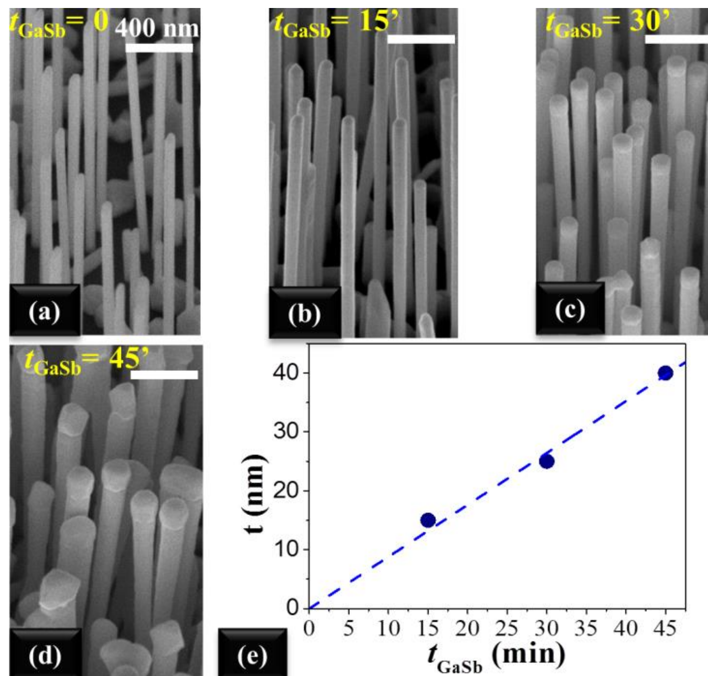

Figure 7.3. 45° tilted SEM micrographs of (a)core InAs NWs, (b)–(d) InAs/GaSb core–shell NWs with shell growth time of 15, 30 and 45 min, respectively. (e) Plot of shell thickness as a function of GaSb growth time.

Various morphological changes in InAs/GaSb NWs with respect to InAs NWs can be observed in Figure 7.3(b-d) when the GaSb shell growth time was varied. First, it can be clearly seen that the diameter of the NWs increases with t_{GaSb}. The shell thickness is plotted in Figure 7.3(e) and varies linearly with the shell growth time. The shell growth rate is ~0.9 nm/min under the given growth conditions.

Second, the tips of the NWs become flat for long shell growth times (30 min and 45 min). The formation of flat NW tips is attributed to the axial growth of GaSb and has been studied in detail in Ref.[58].

Third, it is also evident from the SEM images that GaSb shell does not grow uniformly along the length of the NW. Unlike the InAs cores which show non-tapered morphology (see Figure 7.3(a)), the InAs/GaSb heterostructured NWs with shell grown for 45 min are reverse tapered (see Figure 7.4(b)). The reverse tapering is caused due to shadowing effect which causes low shell growth at the bases and high shell growth near the tips. The reverse tapering can be minimized by growing GaSb shell on low InAs NW density. Figure 7.4(b) shows uniform InAs/GaSb NWs obtained with low NW density (3-4 NWs/μm^2) under identical GaSb shell growth conditions.

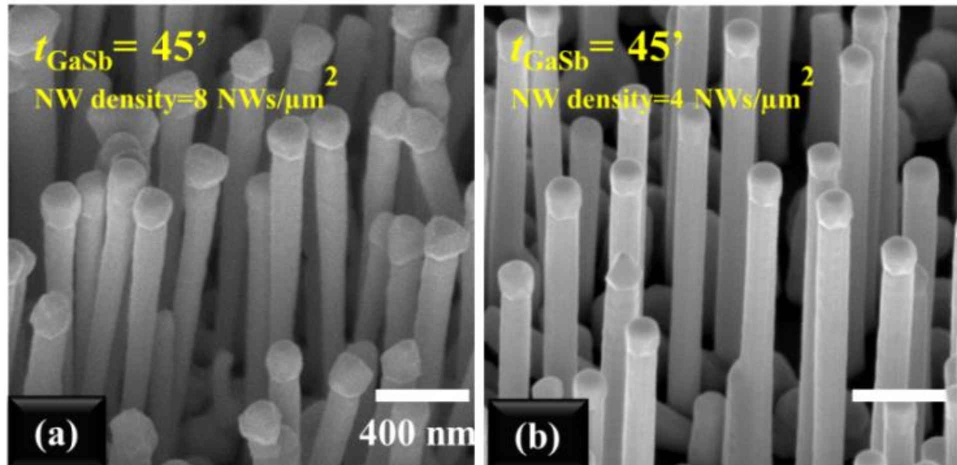

Figure 7.4. 45° tilted SEM micrographs of GaSb shell grown for 45 min on InAs cores with NW density of (a) ~8 NWs/μm^2 and (b) ~4 NWs/μm^2.

7.4 Compositional and structural characterization

To investigate the core-shell structure, InAs/GaSb NWs shown in Figure 7.4(b) were examined by STEM and EDX. The corresponding STEM image and EDX profiles are depicted in Figure 7.5(a-c).

Elemental maps for Ga and In indicate a high homogeneity and sharp interface between the crystalline InAs core and epitaxial GaSb shell. The thickness of the GaSb shell was ~ 30 nm as measured form the EDX profile shown in Figure 7.5(c). Apart from the GaSb shell, axial growth of GaSb on the NW takes place as revealed by EDX maps. The length of the axially grown GaSb segment is ∼100 − 150 nm.

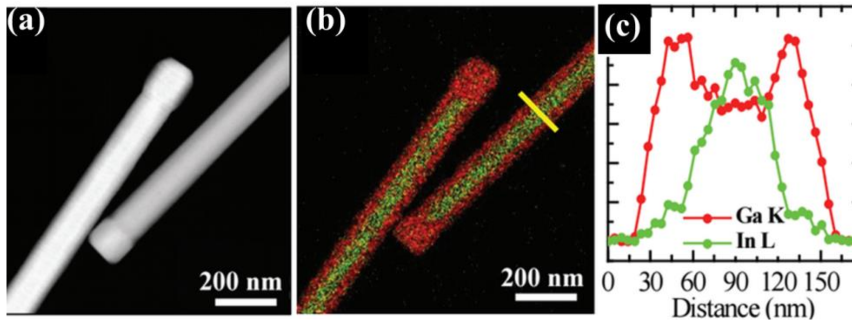

Figure 7.5.(a) STEM image of two InAs/GaSb core-shell NWs transferred onto a standard TEM grid. (b) EDX element map of InAs/GaSb NWs. The presence of the gallium (red-dotted area) is confined on the surface whereas the In (green-dotted area) is present only in correspondence of the core of the NW. (c) Cross-section line profile corresponding to the yellow cut visible in (b) showing clearly the presence of the indium peak only in correspondence of the NW core and the gallium peaks identifying the NW shell. Figures are adapted from Ref.[195].

Figure 7.6 displays a TEM micrograph acquired from the <110> zone axis of an InAs/GaSb core-shell NW. The inset is a selected area electron diffraction pattern of the same NW. A high density of stacking faults can be seen in the InAs core as well as in the GaSb shell. High stacking fault density is usually observed in CF InAs NWs (as discussed in chapter 4 and shown in Figure 4.11) which is also transferred to the GaSb shell. The streaky diffraction pattern shown in the inset of Figure 7.6 also reveals the high density of stacking faults in InAs/GaSb NW.

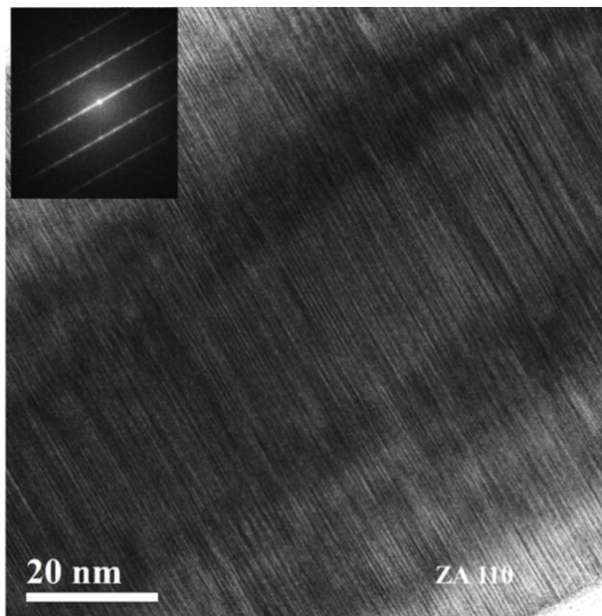

Figure 7.6. TEM image and SAED pattern (inset) of the InAs/GaSb core–shell NW with shell growth time of 45 min viewed along the⟨110⟩ zone axis.

Reasonable information about the facets of InAs/GaSb core-shell NWs can be obtained from high angle annular dark field (HAADF) imaging. Figure 7.7(a) shows HAADF-STEM image of an InAs/GaSb core-shell NW together with a plot of its profile in Figure 7.7(b). The HAADF intensity profile was plotted from the left NW edge to the right NW edge in the radial direction of a NW seen along <110> projection (see Figure 7.7(b)).

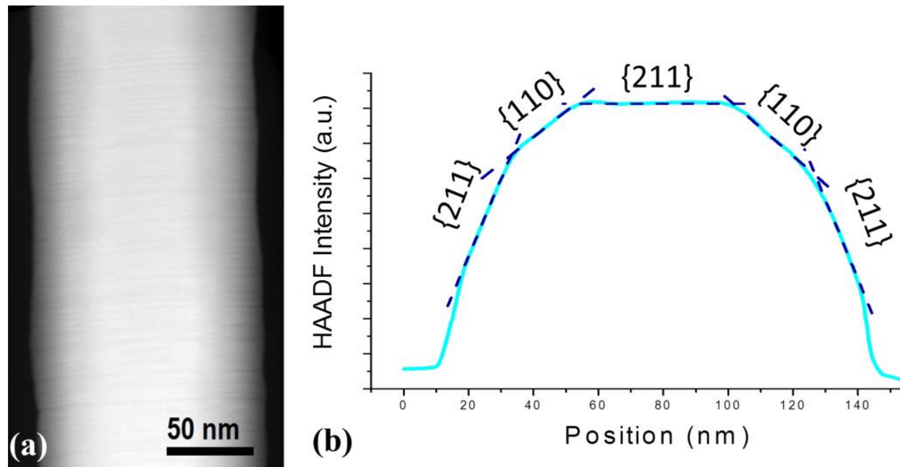

Figure 7.7. (a) HAADF image an InAs/GaSb core–shell NW along with its (b) profile taken from ⟨110⟩ zone axis. The InAs/GaSb core–shell NWs are bound by twelve side facets belonging to the {110} and {211} family. Dashed lines are guides to the eye.

Due to similar lattice constants and atomic numbers of GaSb and InAs, it is difficult to distinguish between the shell and core materials by STEM-HAADF as shown in Figure 7.7(a).The profile in Figure 7.7(b) shows several linear regions indicating a faceted cross-section with {110} and {211} side facets. The shape of the GaSb shell can be reconstructed from the information obtained from the HAADF line profile. Accordingly, the InAs/GaSb core–shell NWs have dodecagonal shape bounded by twelve side facets belonging to the {110} and {211} families. On the other hand the InAs core is hexagonal with six {211} side facets. Reiger et.al [58] also observed a similar dodecagonal shape of the GaSb shell around a hexagonal InAs core when HAADF profile was acquired form a region above the NW base or below the NW tip.

7.5 Performance of InAs/GaSb Esaki diode

InAs/GaSb devices were fabricated starting from CF InAs/GaSb core-shell NWs shown in Figure 7.4(b). InAs/GaSb heterostructured NWs were transferred to a pre-patterned p++Si/SiO_2 substrate by drop casting. In order to selectively contact the InAs and GaSb

regions of the NWs, a highly selective GaSb from InAs wet-etching protocol was optimized. Contacts were realized in two distinct e-beam lithography (EBL) steps.
First EBL process was performed in order to remove the GaSb shell and deposit the contact electrodes on top of the InAs core. Selective GaSb wet-etching process was achieved soaking the sample into an NaOH solution (1 M in water, leading to an etch rate of ~5-10 nm/s) for 10 s to ensure a complete removal of the GaSb shell. Before the first Ni/Au metallization, the InAs cores were passivated using a standard ammonium polysulfide $(NH_4)_2S_x$ solution in order to promote the formation of low-resistance ohmic contacts. The Ni/Au (10/140 nm) electrodes were deposited by thermal evaporation.
The second EBL step allowed the creation of Ni/Au contacts to the GaSb shells. Prior to metal deposition, the contact area was passivated in an HCl: H_2O 1:3 bath for 30 s in order to diminish the impact of native oxide. The Ni/Au (10/140 nm) electrodes were thus evaporated using the same procedure used for the core contacts. The substrate was exploited as the backgate - which is highly asymmetric with respect to the NW center. The resulting device structure is shown in Figure 7.8(a) and (b). Figure 7.8(c) displays a cross-sectional sketch of the NW on top of the device substrate, embedding a radial broken-gap heterojunction.

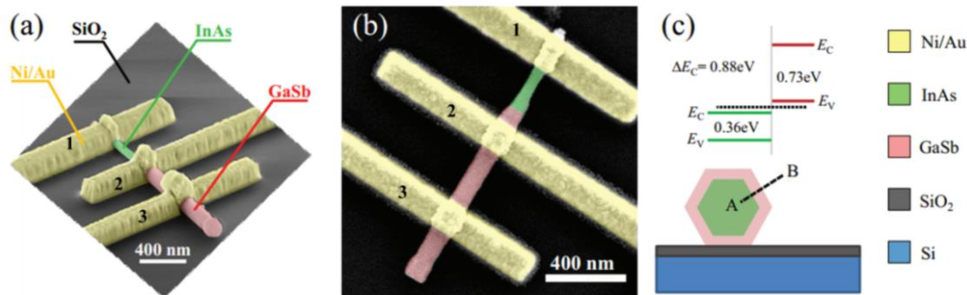

Figure 7.8. (a) False-colored SEM image (60° tilt) of a typical InAs/GaSb device, deposited on a SiO_2/p-Si substrate. (b) Top-view of one of the devices. The transport properties of the core-shell configuration are explored by using electrodes 1-2. (c) Schematic illustration device cross-section embedding a radial broken-gap InAs/GaSb junction. Sketch of the band alignment along the radial direction AB. Figures are adapted from Ref.[195]

Transport measurements were performed at T = 4.2 K, in dark conditions and in the presence of a low-pressure He exchange gas. All the experiments were performed using a two wire core-shell (CS) configuration with contacts 1 and 2, using a DL1211 current pre-amplifier as shown in Figure 7.9(a). The general transport features of the CS configuration are shown in Figure 7.9(b), where I-V semilog curves are plotted. Data

were measured for various values of the backgate voltage V_{BG}.

The CS configuration leads to a strong negative differential resistance (NDR) behavior which is visible in Figure 7.9(b) for $V_{DS} > 0$ due to the overlap of the two bandgaps of InAs and GaSb. For $V_{DS} < 0$, the current increases almost linearly with the applied bias.

The I-V curves are also studied as a function of the backgate voltage V_{BG} in a range going from 30 V up to -2 V. As visible in the plot in Figure 7.9(b), the magnitude of the NDR can be strongly modulated by the field-effect as a consequence of the tuning or detuning of the radial Esaki junction along the azimuthal angle of the NW. In particular, for VBG = -2 V the junction virtually displays no NDR (quenching) while strong NDR is observed for 0 and +30 V.

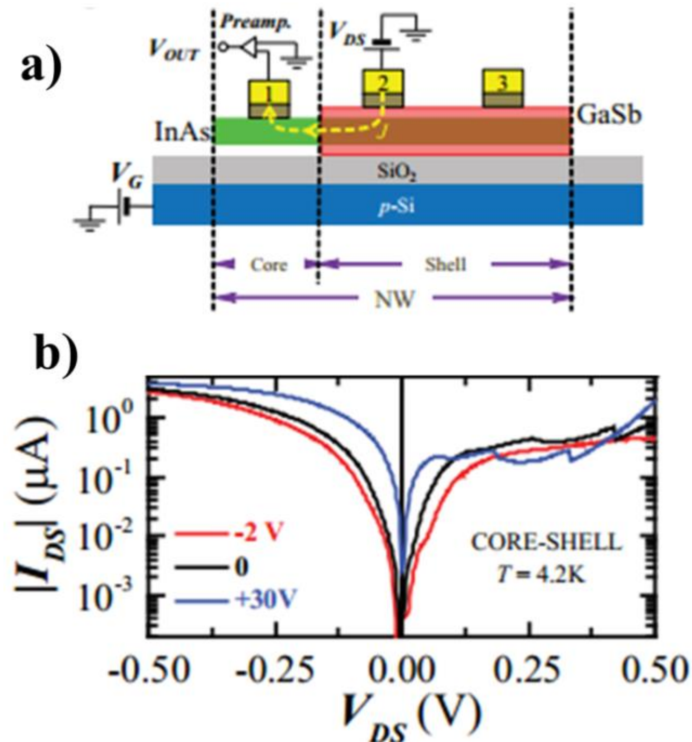

Figure 7.9. (a) Device architecture for two-wire measurement of core-shell (contacts 1-2) transport characteristics, as a function of the backgate voltage V_{BG}. (b) Absolute value of the current (I_{DS}) versus the drain-source voltage (V_{DS}) of InAs-GaSb core-shell at T = 4.2 K. The I_{DS} versus V_{DS} characteristics were measured at different backgate voltages ranging from -2 to +30 V. The explored gating range was chosen so to allow a quenching of the NDR in the device. Figures are adapted from Ref.[195]

7.6 Chapter summary

In this chapter, the growth parameters, morphology and crystal structure of InAs/GaSb

core-shell heterostructured NWs have been investigated. The precursors and NW density were optimized to obtain NWs with uniform GaSb shell. HRTEM of the NWs revealed a defective crystal structure. The facets of the core-shell NWs were determined by STEM-HAADF. It was found that the NWs have dodecagonal shape bounded by twelve side facets belonging to the {110} and {211} families. The InAs/GaSb NWs have been used to fabricate Esaki diodes which display NDR characteristics as a function of the device bias. It was shown that NDR can be tuned, or even quenched, by changing the gate bias.

8 Conclusions and perspectives

In this thesis we have discussed several growth procedures to grow InAs NWs and related axial and radial heterostructures by Au-catalyzed, catalyst-free and self-catalyzed methods. We have discussed different strategies to control NW diameter and length distributions of Au-catalyzed InAs NWs. The Au NPs are obtained either by thermal dewetting of Au film or Au colloidal dispersion. InAs NWs seeded from thermally dewetted Au NPs have broad diameter distributions but have narrow Poissonian length distribution and uniform density. On the other hand, InAs NWs seeded from Au colloidal NPs have a narrow diameter distribution but broad and asymmetric length distributions. Although, the length distributions can be improved by removing the annealing step, they are still non-Poissonian. The NW density is also non-uniform and depends on day to day substrate preparation. Proper choice between these two catalyst preparation methods can allow to obtain InAs NWs with as required morphology and density.

Triggered by the issues of Au contamination in semiconductors and the advantages of integrating III-V semiconductors on silicon substrates, catalyst-free and self-catalyzed growth of InAs NWs on silicon are also investigated. A new approach of silicon substrate preparation has been demonstrated in which surface defects are generated on silicon substrates by sputtering by employing different sputtering techniques. These surface defects serve as preferential nucleation sites and can be controlled to obtain InAs NWs over a wide range of densities. This substrate preparation technique offers a simple, cost-effective, and scalable method to grow Au-free InAs NWs on silicon

substrates.

Catalyst-free InAs NWs is grown using a two-step growth protocol resulting in NWs with non-tapered morphology. InAs NWs with different aspect ratios are obtained by optimizing the precursor fluxes and growth temperature. Furthermore, the catalyst-free growth mechanism is investigated using theoretical model and a general model is deduced that can accurately model all the samples grown in a wide range of experimentally controllable parameter space.

Self-catalyzed InAs NWs are grown with an In droplet at the NW tip throughout NW growth by maintaining In-rich growth conditions. It is found that the NWs continue to nucleate on the silicon substrate widening the NW length and diameter distribution. Further understanding of the nucleation and growth mechanism is obtained by interpreting our experimental data with a theoretical model. Accordingly, we have obtained estimates of important growth parameters like diffusion length, effective flux ratio and flux imbalance parameter.

We have also demonstrated the growth of Au-catalyzed InAs/GaAs, GaAs/InAs and InAs/GaAs/InAs axial heterostructured NWs. According to our study, the growth of GaAs segment on top of InAs is straightforward but the reverse growth of InAs on top of GaAs requires careful attention. We have shown that a group III rich Au alloy NP is a prerequisite to grow straight InAs segments on GaAs NWs.

Aimed at the creation of radial broken-gap heterojunction, the growth of InAs/GaSb core-shell heterostructured NWs is demonstrated using the catalyst-free growth approach on silicon substrate. After optimizing the core-shell morphology, Esaki tunnel diodes are fabricated successfully from InAs/GaSb NWs. Current-voltage characteristics clearly display negative differential resistance, a signature of tunneling transport, which can be tuned or even quenched by field effect.

During the course of this thesis, the research work on catalyst-free and self-catalyzed NW growth mechanisms progressed from being in its infancy to an established method. However, there are many details on the fundamental growth mechanisms that need to be investigated in the future. Unlike Au-catalyzed NWs which have phase-pure wurtzite InAs NWs, the catalyst-free and self-catalyzed grown NWs have a high density of stacking faults. Accordingly, additional work is required to improve the crystal quality of Au-free InAs NWs in order to improve their electronic and optical properties. The other issue that can be addressed in future is to inhibit parasitic island nucleation by optimizing the silicon substrate preparation methods.

The possibility to tune the growth mode (kinked or straight) by changing the Au NP

composition in Au-catalyzed InAs/GaAs heterostructured NWs is an important result achieved in this work. It will be important to check if these results can be extended to other III-V heterostructured NWs. For example, Au-catalyzed III-V NWs grown with high V/III ratios are known to have group III poor NPs with small contact angles and therefore are not suitable for obtaining straight heterostructures. In contrast, low V/III ratios yield group III rich NPs with large contact angles and should be more advantageous for the straight growth.

Finally, the catalyst-free core-shell heterostructured NWs with combinations of InAs, InP and GaSb materials represent promising structures for future device applications and therefore requires detailed study of the growth and interfacial quality. Additionally, the transport properties of these structures have to be investigated.

9 Bibliography

[1] Moore G E 1998 Cramming more components onto integrated circuits (Reprinted from Electronics, pg 114-117, April 19, 1965) *Proc. IEEE* **86** 82–5

[2] Wagner R S and Ellis W C 1964 Vapor-liquid-solid mechanism of single crystal growth *Appl. Phys. Lett.* **4** 89–90

[3] Dick K, Bolinsson J, Messing M E, Lehmann S, Johansson J and Caroff P 2011 Parameter space mapping of InAs nanowire crystal structure *J. Vac. Sci. Technol. B* **29**04D103

[4] Caroff P, Dick K A, Johansson J, Messing M E, Deppert K and Samuelson L 2009 Controlled polytypic and twin-plane superlattices in III-V nanowires. *Nat. Nanotechnol.* **4** 50–5

[5] Dos Santos C L and Piquini P 2010 Diameter dependence of mechanical, electronic, and structural properties of InAs and InP nanowires: A first-principles study *Phys. Rev. B* **81** 75408

[6] Ford A C, Ho J C, Chueh Y-L, Tseng Y-C, Fan Z, Guo J, Bokor J and Javey A 2009 Diameter-dependent electron mobility of InAs nanowires. *Nano Lett.* **9** 360–5

[7] Scheffler M, Nadj-Perge S, Kouwenhoven L P, Borgström M T and Bakkers E P A M 2009 Diameter-dependent conductance of InAs nanowires *J. Appl. Phys.* **106** 124303

[8] Tomioka K, Yoshimura M and Fukui T 2012 A III–V nanowire channel on silicon for high-performance vertical transistors *Nature* **488** 189–92

[9] Johansson S, Ghalamestani S G, Egard M, Borg M, Berg M, Wernersson L E

and Lind E 2012 High frequency vertical InAs nanowire MOSFETs integrated on Si substrates *Phys. Status Solidi Curr. Top. Solid State Phys.* **9** 350–3

[10] Johansson S, Egard M, Ghalamestani S G, Borg B M, Berg M, Wernersson L and Lind E 2011 RF characterization of vertical InAs nanowire wrap-gate transistors integrated on Si substrates *IEEE Trans. Microw. Theory Tech.* **59** 2733–8

[11] Rehnstedt C, Mårtensson T, Thelander C, Samuelson L and Wernersson L E 2008 Vertical InAs nanowire wrap gate transistors on Si substrates *IEEE Trans. Electron Devices* **55** 3037–41

[12] Viti L, Vitiello M S, Ercolani D, Sorba L and Tredicucci A 2012 Se-doping dependence of the transport properties in CBE-grown InAs nanowire field effect transistors *Nanoscale Res. Lett.* **7** 159

[13] Vitiello M S, Viti L, Coquillat D, Knap W, Ercolani D and Sorba L 2015 One dimensional semiconductor nanostructures: An effective active-material for terahertz detection *APL Mater.* **3** 26104

[14] Chuang L C, Sedgwick F G, Chen R, Ko W S, Moewe M, Ng K W, Tran T T D and Chang-Hasnain C 2011 GaAs-based nanoneedle light emitting diode and avalanche photodiode monolithically integrated on a silicon substrate *Nano Lett.* **11** 385–90

[15] Chen R, Tran T-T D, Ng K W, Ko W S, Chuang L C, Sedgwick F G and Chang-Hasnain C 2011 Nanolasers grown on silicon *Nat. Photonics* **5** 170–5

[16] Mallorquí A D, Alarcón-Lladó E, Russo-Averchi E, Tütüncüoglu G, Matteini F, Rüffer D and Morral A F I 2014 Characterization and analysis of InAs / p –Si heterojunction nanowire-based solar cell *J. Phys. D. Appl. Phys.* **47** 394017

[17] Thelander C, Björk M T, Larsson M W, Hansen a. E, Wallenberg L R and Samuelson L 2004 Electron transport in InAs nanowires and heterostructure nanowire devices *Solid State Commun.* **131** 573–9

[18] Rossella F, Bertoni A, Ercolani D, Rontani M, Sorba L, Beltram F and Roddaro S 2014 Nanoscale spin rectifiers controlled by the Stark effect *Nat. Nanotechnol.* **9** 997–1001

[19] Dick K A 2008 A review of nanowire growth promoted by alloys and non-alloying elements with emphasis on Au-assisted III–V nanowires *Prog. Cryst. Growth Charact. Mater.* **54** 138–73

[20] Gudiksen M S and Lieber C M 2000 Diameter-selective synthesis of semiconductor nanowires *J. Am. Chem. Soc.* **122** 8801–2

[21] Gomes U P, Ercolani D, Zannier V, Beltram F and Sorba L 2015 Controlling the diameter distribution and density of InAs nanowires grown by Au-assisted methods *Semicond. Sci. Technol.* **30** 115012

[22] Wu Y and Yang P 2001 Direct Observation of Vapor-Liquid-Solid Nanowire Growth *J. Am. Chem. Soc.* **123** 3165–6

[23] Sutter E and Sutter P 2008 Phase diagram of nanoscale alloy particles used for vapor-liquid-solid growth of semiconductor nanowires *Nano Lett.* **8** 411–4

[24] Sutter E A and Sutter P W 2010 Size-dependent phase diagram of nanoscale alloy drops used in Vapor-Liquid-Solid growth of semiconductor nanowires *ACS Nano* **4** 4943–7

[25] Kodambaka S, Tersoff J, Reuter M C and Ross F M 2007 Germanium nanowire growth below the eutectic temperature. *Science* **316** 729–32

[26] Dick K A, Deppert K, Karlsson L S, Wallenberg L R, Samuelson L and Seifert W 2005 A new understanding of Au-assisted growth of III-V semiconductor nanowires *Adv. Funct. Mater.* **15** 1603–10

[27] Hilner E, Lundgren E and Mikkelsen A 2010 Surface structure and morphology of InAs(111)B with/without gold nanoparticles annealed under arsenic or atomic hydrogen flux *Surf. Sci.* **604** 354–60

[28] Dayeh S A, Yu E T and Wang D 2007 Excess indium and substrate effects on the growth of InAs nanowires *Small* **3** 1683–7

[29] Veresegyházy, R, Pécz, B, Mojzes I 1986 The Influence of a Gold Layer on the Thermal Decomposition of InAs *Phys. status solidi. A,* **94** K11–2

[30] Elliott R and Shunk F 1981 The Au−Ga (Gold-Gallium) system *Bull. Alloy Phase Diagrams* **2** 356–8

[31] Bauer J, Gottschalch V and Wagner G 2008 The influence of the droplet composition on the vapor-liquid-solid growth of InAs nanowires on GaAs (1- 1- 1-) B by metal-organic vapor phase epitaxy *J. Appl. Phys.* **104** 114315

[32] Thelander C, Mårtensson T, Björk M T, Ohlsson B J, Larsson M W, Wallenberg L R and Samuelson L 2003 Single-electron transistors in heterostructure nanowires *Appl. Phys. Lett.* **83** 2052–4

[33] Bjork M T, Ohlsson B J, Thelander C, Persson A I, Deppert K, Wallenberg L R and Samuelson L 2002 Nanowire resonant tunneling diodes *Appl. Phys. Lett.* **81** 4458–60

[34] Anufriev R, Chauvin N, Khmissi H, Naji K, Patriarche G, Gendry M and Bru-Chevallier C 2013 Quantum efficiency of InAs/InP nanowire heterostructures

grown on silicon substrates *Phys. status solidi - Rapid Res. Lett.* **7** 878–81

[35] Dick K A, Bolinsson J, Borg B M and Johansson J 2012 Controlling the abruptness of axial heterojunctions in III-V nanowires: Beyond the reservoir effect *Nano Lett.* **12** 3200–6

[36] Dick K A, Kodambaka S, Reuter M C, Deppert K, Samuelson L, Seifert W, Wallenberg L R and Ross F M 2007 The morphology of axial and branched nanowire heterostructures *Nano Lett.* **7** 1817–22

[37] Paladugu M, Zou J, Guo Y N, Zhang X, Kim Y, Joyce H J, Gao Q, Tan H H and Jagadish C 2008 Nature of heterointerfaces in GaAs/InAs and InAs/GaAs axial nanowire heterostructures *Appl. Phys. Lett.* **93** 101911

[38] Krogstrup P, Yamasaki J, Sorensen C B, Johnson E, Wagner J B, Pennington R, Aagesen M, Tanaka N and Nygard J 2009 Junctions in axial III-V heterostructure nanowires obtained via an interchange of group III elements *Nano Lett.* **9** 3689–93

[39] Johansson J and Dick K A 2011 Recent advances in semiconductor nanowire heterostructures *CrystEngComm* **13** 7175

[40] Ercolani D, Rossi F, Li A, Roddaro S, Grillo V, Salviati G, Beltram F and Sorba L 2009 InAs/InSb nanowire heterostructures grown by chemical beam epitaxy. *Nanotechnology* **20** 505605

[41] Li A, Zou J and Han X 2016 Growth of III-V semiconductor nanowires and their heterostructures *Sci. China Mater.* **59** 51–91

[42] Noor Mohammad S 2011 Why self-catalyzed nanowires are most suitable for large-scale hierarchical integrated designs of nanowire nanoelectronics *J. Appl. Phys.* **110** 84310

[43] Bar-Sadan M, Barthel J, Shtrikman H and Houben L 2012 Direct imaging of single Au atoms within GaAs nanowires *Nano Lett.* **12** 2352–6

[44] Allen J E, Hemesath E R, Perea D E, Lensch-Falk J L, Li Z Y, Yin F, Gass M H, Wang P, Bleloch A L, Palmer R E and Lauhon L J 2008 High-resolution detection of Au catalyst atoms in Si nanowires. *Nat. Nanotechnol.* **3** 168–73

[45] Du Y A, Sakong S and Kratzer P 2013 As vacancies, Ga antisites, and Au impurities in zinc blende and wurtzite GaAs nanowire segments from first principles *Phys. Rev. B* **87** 75308

[46] Sobanska M, Korona K P, Zytkiewicz Z R, Klosek K and Tchutchulashvili G 2015 Kinetics of self-induced nucleation and optical properties of GaN nanowires grown by plasma-assisted molecular beam epitaxy on amorphous AlxOy *J. Appl.*

Phys. **118** 184303

[47] Rudolph D, Hertenberger S, Bolte S, Paosangthong W, Spirkoska D, Döblinger M, Bichler M, Finley J J, Abstreiter G and Koblmüller G 2011 Direct observation of a noncatalytic growth regime for GaAs nanowires *Nano Lett.* **11** 3848–54

[48] Hertenberger S, Rudolph D, Bolte S, Döblinger M, Bichler M, Spirkoska D, Finley J J, Abstreiter G and Koblmüller G 2011 Absence of vapor-liquid-solid growth during molecular beam epitaxy of self-induced InAs nanowires on Si *Appl. Phys. Lett.* **98** 123114

[49] Consonni V, Knelangen M, Geelhaar L, Trampert A and Riechert H 2010 Nucleation mechanisms of epitaxial GaN nanowires: Origin of their self-induced formation and initial radius *Phys. Rev. B* **81** 85310

[50] Spirkoska D, Colombo C and Heiß M 2009 Growth methods and properties of high purity III-V nanowires by molecular beam epitaxy *Advances in Solid State Physics* vol 48pp 13–26

[51] Consonni V, Dubrovskii V G, Trampert A, Geelhaar L and Riechert H 2012 Quantitative description for the growth rate of self-induced GaN nanowires *Phys. Rev. B* **85** 153313

[52] Dubrovskii V G, Sibirev N V., Harmand J C and Glas F 2008 Growth kinetics and crystal structure of semiconductor nanowires *Phys. Rev. B* **78** 235301

[53] Tomioka K and Fukui T 2014 Recent progress in integration of III–V nanowire transistors on Si substrate by selective-area growth *J. Phys. D. Appl. Phys.* **47** 394001

[54] Tomioka K, Mohan P, Noborisaka J, Hara S, Motohisa J and Fukui T 2007 Growth of highly uniform InAs nanowire arrays by selective-area MOVPE *J. Cryst. Growth* **298** 644–7

[55] Ikejiri K, Noborisaka J, Hara S, Motohisa J and Fukui T 2007 Mechanism of catalyst-free growth of GaAs nanowires by selective area MOVPE *J. Cryst. Growth* **298** 616–9

[56] Ji X, Yang X, Du W, Pan H, Luo S and Ji H 2016 InAs/GaSb core-shell nanowires grown on Si substrates by metal-organic chemical vapor deposition *Nanotechnology* **27** 275601

[57] Wang X, Du W, Yang X and Yang T 2015 Self-catalyzed growth mechanism of InAs nanowires and growth of InAs/GaSb heterostructured nanowires on Si substrates *J. Cryst. Growth* **426** 287–92

[58] Rieger T, Grützmacher D and Lepsa M I 2015 Misfit dislocation free InAs/GaSb

core-shell nanowires grown by molecular beam epitaxy. *Nanoscale* **7** 356–64

[59] Rieger T, Grützmacher D and Lepsa M I 2015 InAs nanowires with AlxGa1−xSb shells for band alignment engineering *J. Cryst. Growth* **425** 80–4

[60] Anyebe E A, Zhuang Q, Sanchez A M, Lawson S, Robson A J, Ponomarenko L, Zhukov A and Kolosov O 2014 Self-catalysed growth of InAs nanowires on bare Si substrates by droplet epitaxy *Phys. status solidi - Rapid Res. Lett.* **8** 658–62

[61] Grap T, Rieger T, Blömers C, Schäpers T, Grützmacher D and Lepsa M I 2013 Self-catalyzed VLS grown InAs nanowires with twinning superlattices *Nanotechnology* **24** 335601

[62] Priante G, Ambrosini S, Dubrovskii V G, Franciosi A and Rubini S 2013 Stopping and resuming at will the growth of GaAs nanowires *Cryst. Growth Des.* **13** 3976–84

[63] Scarpellini D, Somaschini C, Fedorov A, Bietti S, Frigeri C, Grillo V, Esposito L, Salvalaglio M, Marzegalli A, Montalenti F, Bonera E, Medaglia P G and Sanguinetti S 2015 InAs/GaAs Sharply Defined Axial Heterostructures in Self-Assisted Nanowires. *Nano Lett.* **15** 3677–83

[64] Priante G, Glas F, Patriarche G, Pantzas K, Oehler F and Harmand J C 2016 Sharpening the Interfaces of Axial Heterostructures in Self-Catalyzed AlGaAs Nanowires: Experiment and Theory *Nano Lett.* **16** 1917–24

[65] Gomes U P, Yadav Y K, Chowdhury S, Ranjan K, Rathi S and Biswas D 2012 Prospects of III-Vs for logic applications *J. Nano- Electron. Phys.* **4** 2009

[66] Chau R, Datta S and Majumdar A 2005 Opportunities and challenges of III-V nanoelectronics for future high-speed, low-power logic applications *Technical Digest - IEEE Compound Semiconductor Integrated Circuit Symposium, CSIC* pp 17–20

[67] Cirlin G E, Dubrovskii V G, Soshnikov I P, Sibirev N V., Samsonenko Y B, Bouravleuv A D, Harmand J C and Glas F 2009 Critical diameters and temperature domains for MBE growth of III-V nanowires on lattice mismatched substrates *Phys. Status Solidi - Rapid Res. Lett.* **3** 112–4

[68] Chuang L C, Moewe M, Chase C, Kobayashi N P, Chang-Hasnain C and Crankshaw S 2007 Critical diameter for III-V nanowires grown on lattice-mismatched substrates *Appl. Phys. Lett.* **90** 43115

[69] Tomioka K, Motohisa J, Hara S and Fukui T 2008 Control of InAs nanowire growth directions on Si *Nano Lett.* **8** 3475–80

[70] Wei W, Bao X Y, Soci C, Ding Y, Wang Z L and Wang D 2009 Direct

heteroepitaxy of vertical InAs nanowires on Si substrates for broad band photovoltaics and photodetection *Nano Lett.* **9** 2926–34

[71] Fortuna S A and Li X 2010 Metal-catalyzed semiconductor nanowires: a review on the control of growth directions *Semicond. Sci. Technol.* **25** 24005

[72] Consonni V, Knelangen M, Trampert A, Geelhaar L and Riechert H 2011 Nucleation and coalescence effects on the density of self-induced GaN nanowires grown by molecular beam epitaxy *Appl. Phys. Lett.* **98** 71913

[73] Gomes U P, Ercolani D, Zannier V, David J, Gemmi M, Beltram F and Sorba L 2016 Nucleation and growth mechanism of self-catalyzed InAs nanowires on silicon *Nanotechnology* **27** 255601

[74] Fernández-Garrido S, Kaganer V M, Hauswald C, Jenichen B, Ramsteiner M, Consonni V, Geelhaar L and Brandt O 2014 Correlation between the structural and optical properties of spontaneously formed GaN nanowires: a quantitative evaluation of the impact of nanowire coalescence. *Nanotechnology* **25** 455702

[75] Kaganer V M, Fernandez-garrido S, Dogan P, Sabelfeld K K and Brandt O 2016 Nucleation , growth and bundling of GaN nanowires in molecular beam epitaxy : Disentangling the origin of nanowire coalescence *Nano Lett.* **16** 3717–25

[76] Brandt O, Fernandez-Garrido S, Zettler J K, Luna E, Jahn U, Cheze C and Kaganer V M 2014 Statistical analysis of the shape of one-dimensional nanostructures: Determining the coalescence degree of spontaneously formed GaN nanowires *Cryst. Growth Des.* **14** 2246–53

[77] Tsang W T 1988 Chemical beam epitaxy *IEEE Circuits Devices Mag.* **4** 18–24

[78] Tsang W T 1984 Chemical beam epitaxy of InP and GaAs *Appl. Phys. Lett.* **45** 1234–6

[79] Chiu T H and Ditzenberger J A 1990 Chemical beam epitaxial growth of InAs using trimethylindium and arsine *Appl. Phys. Lett.* **56** 2219–21

[80] Arthur J R 2002 Molecular beam epitaxy *Surf. Sci.* **500** 189–217

[81] Thompson A G 1997 MOCVD technology for semiconductors *Mater. Lett.* **30** 255–63

[82] Kramer N, Niesten M and Schonenberger C 1995 Resistless High-Resolution Optical Lithography on Silicon *Appl. Phys. Lett.* **67** 2989–91

[83] Kobayashi Y, Shinoda Y and Sugii K 1990 Thermal Desorption from Si(111) Surfaces with Native Oxides Formed During Chemical Treatments *Jpn. J. Appl. Phys.* **29** 1004–8

[84] Gräf D 1989 Reaction of water with hydrofluoric acid treated silicon(111) and

(100) surfaces *J. Vac. Sci. Technol. A* **7** 808

[85] Gomes U P, Ercolani D, Zannier V, Battiato S, Murata Y, Heun S, Beltram F and Sorba L 2016 Heterogeneous nucleation of catalyst-free InAs nanowires on silicon *Nanotechnology* **submitted**

[86] Otsu N 1979 Threshold selection method from grey-level histograms *IEEE Trans Syst., Man, Cybern.* **SMC-9** 62–6

[87] Dubrovskii V G, Sibirev N V., Cirlin G E, Soshnikov I P, Chen W H, Larde R, Cadel E, Pareige P, Xu T, Grandidier B, Nys J P, Stievenard D, Moewe M, Chuang L C and Chang-Hasnain C 2009 Gibbs-Thomson and diffusion-induced contributions to the growth rate of Si, InP, and GaAs nanowires *Phys. Rev. B* **79** 1–7

[88] Fröberg L, Seifert W and Johansson J 2007 Diameter-dependent growth rate of InAs nanowires *Phys. Rev. B* **76** 153401

[89] Messing M E, Hillerich K, Bolinsson J, Storm K, Johansson J, Dick K A and Deppert K 2010 A comparative study of the effect of gold seed particle preparation method on nanowire growth *Nano Res.* **3** 506–19

[90] Xu H, Guo Y, Sun W, Liao Z, Burgess T, Lu H, Gao Q, Tan H H, Jagadish C and Zou J 2012 Quantitative study of GaAs nanowires catalyzed by Au film of different thicknesses *Nanoscale Res. Lett.* **7** 589

[91] Hiruma K, Haraguchi K, Yazawa M, Madokoro Y and Katsuyama T 2006 Nanometre-sized GaAs wires grown by organo-metallic vapour-phase epitaxy *Nanotechnology* **17** S369–75

[92] Guo D L, Huang X, Xing G Z, Zhang Z, Li G P, He M, Zhang H, Chen H and Wu T 2011 Metal-layer-assisted coalescence of Au nanoparticles and its effect on diameter control in vapor-liquid-solid growth of oxide nanowires *Phys. Rev. B* **83** 45403

[93] Voorhees P W 1985 The theory of Ostwald ripening *J. Stat. Phys.* **38** 231–52

[94] Granqvist C G and Buhrman R 1976 Size distributions for supported metal catalysts:Coalescence growth versus ostwald ripening *J. Catal.* **42** 477–9

[95] Senkov O N 2008 Particle size distributions during diffusion controlled growth and coarsening *Scr. Mater.* **59** 171–4

[96] Lotty O, Hobbs R, O'Regan C, Hlina J, Marschner C, O'Dwyer C, Petkov N and Holmes J D 2013 Self-seeded growth of germanium nanowires: Coalescence and ostwald ripening *Chem. Mater.* **25** 215–22

[97] Thanh N T K, Maclean N and Mahiddine S 2014 Mechanisms of nucleation and

growth of nanoparticles in solution. *Chem. Rev.* **114** 7610–30

[98] Kim B J, Tersoff J, Kodambaka S, Jang J S, Stach E A and Ross F M 2014 Au transport in catalyst coarsening and Si nanowire formation *Nano Lett.* **14** 4554–9

[99] Ross F M 2010 Controlling nanowire structures through real time growth studies *Reports Prog. Phys.* **73** 114501

[100] Govatsi K, Chrissanthopoulos A, Dracopoulos V and Yannopoulos S N 2014 The influence of Au film thickness and annealing conditions on the VLS-assisted growth of ZnO nanostructures. *Nanotechnology* **25** 215601

[101] Sui M, Li M-Y, Kim E-S and Lee J 2013 Annealing temperature effect on self-assembled Au droplets on Si (111) *Nanoscale Res. Lett.* **8** 525

[102] Mitchell C E J, Howard A, Carney M and Egdell R G 2001 Direct observation of behaviour of Au nanoclusters on TiO2 (110) at elevated temperatures *Surf. Sci.* **490** 196–210

[103] Howard A, Mitchell C E J and Egdell R G 2002 Real time STM observation of Ostwald ripening of Pd nanoparticles on TiO2 (110) at elevated temperature *Surf. Sci. Lett.* **515** L504–18

[104] Hannon J B, Kodambaka S, Ross F M and Tromp R M 2006 The influence of the surface migration of gold on the growth of silicon nanowires *Nature* **440** 69–71

[105] Mikkelsen A and Lundgren E 2013 Surface science of free standing semiconductor nanowires *Surf. Sci.* **607** 97–105

[106] Gudiksen M S, Wang J and Lieber C M 2001 Synthetic control of the diameter and length of single crystal semiconductor nanowires *J. Phys. Chem. B* **105** 4062–4

[107] Jensen L E, Bjork M T, Jeppesen S, Persson A I, Ohlsson B J and Samuelson L 2004 Role of surface diffusion in chemical beam epitaxy of InAs nanowires *Nano Lett.* **4** 1961–4

[108] Sibirev N V, Tchernycheva M, Timofeeva M A, Harmand J C, Cirlin G E and Dubrovskii V G 2012 Influence of shadow effect on the growth and shape of InAs nanowires *J. Appl. Phys.* **111** 104317

[109] Kim Y, Joyce H J, Gao Q, Tan H H, Jagadish C, Paladugu M, Zou J and Suvorova A 2006 Influence of nanowire density on the shape and optical properties of ternary InGaAs nanowires *Nano Lett.* **6** 599–604

[110] Dubrovskii V G, Sibirev N V, Berdnikov Y, Gomes U P, Ercolani D, Zannier V and Sorba L 2016 Length distributions of Au-catalyzed and In-catalyzed InAs

nanowires *Nanotechnology* **27** 375602

[111] Veresegyhyazy R, Mojzes I and Pecz B 1986 Comparative mass spectrometric study of AIII-BV compounds covered with a gold layer *Vacuum* **36** 547–9

[112] Mikkelsen A and Lundgren E 2013 Surface science of free standing semiconductor nanowires *Surf. Sci.* **607** 97–105

[113] Mikkelsen A, Eriksson J, Lundgren E, Andersen J N, Weissenrieder J and Seifert W 2005 The influence of lysine on InP(001) surface ordering and nanowire growth *Nanotechnology* **16** 2354–9

[114] Dubrovskii V G 2013 Self-regulated pulsed nucleation in catalyzed nanowire growth *Phys. Rev. B* **87** 195426

[115] Glas F, Harmand J C and Patriarche G 2010 Nucleation antibunching in catalyst-assisted nanowire growth *Phys. Rev. Lett.* **104** 135501

[116] Wen C Y, Tersoff J, Hillerich K, Reuter M C, Park J H, Kodambaka S, Stach E A and Ross F M 2011 Periodically changing morphology of the growth interface in Si, Ge, and GaP nanowires *Phys. Rev. Lett.* **107** 25503

[117] Glas F 2014 Statistics of sub-Poissonian nucleation in a nanophase *Phys. Rev. B* **90** 125406

[118] Dubrovskii V G, Cirlin G E, Soshnikov I P, Tonkikh A A, Sibirev N V., Samsonenko Y B and Ustinov V M 2005 Diffusion-induced growth of GaAs nanowhiskers during molecular beam epitaxy: Theory and experiment *Phys. Rev. B* **71** 205325

[119] Zhang Y, Sanchez A M, Sun Y, Wu J, Aagesen M, Huo S, Kim D, Jurczak P, Xu X and Liu H 2016 Influence of Droplet Size on the Growth of Self-Catalyzed Ternary GaAsP Nanowires *Nano Lett.* **16** 1237–43

[120] Dayeh S A and Picraux S T 2010 Direct observation of nanoscale size effects in Ge semiconductor nanowire growth *Nano Lett.* **10** 4032–9

[121] Berdnikov Y, Sibirev N, Schmidtbauer J, Borg M, Johansson J and Dubrovskii V 2016 Broadening of length distributions of Au-catalyzed InAs nanowires *AIP Conf. Proc.* vol 1748p 40001

[122] Dubrovskii V G, Berdnikov Y, Schmidtbauer J, Borg M, Storm K, Deppert K and Johansson J 2016 Length distributions of nanowires growing by surface diffusion *Cryst. Growth Des.* **16** 2167–72

[123] Dubrovskii V G and Sibirev N V. 2014 Size distributions, scaling properties, and Bartelt-Evans singularities in irreversible growth with size-dependent capture coefficients *Phys. Rev. B* **89** 54305

[124] Dubrovskii V G 2009 Fluctuation-induced spreading of size distribution in condensation kinetics *J. Chem. Phys.* **131** 164514

[125] Dubrovskii V G and Hervieu Y Y 2014 Diffusion-induced growth of nanowires: Generalized boundary conditions and self-consistent kinetic equation *J. Cryst. Growth* **401** 431–40

[126] Gomes U P, Ercolani D, Sibirev N V, Gemmi M, Dubrovskii V G, Beltram F and Sorba L 2015 Catalyst-free growth of InAs nanowires on Si (111) by CBE *Nanotechnology* **26** 415604

[127] Bolkhovityanov, Y. Pchelyakov O 2008 GaAs epitaxy on Si substrates: modern status of research and engineering *Phys. -Uspekhi* **178** 437–56

[128] Dubrovskii V G, Consonni V, Trampert A, Geelhaar L and Riechert H 2012 Scaling thermodynamic model for the self-induced nucleation of GaN nanowires *Phys. Rev. B* **85** 165317

[129] Dubrovskii V G, Consonni V, Geelhaar L, Trampert A and Riechert H 2012 Scaling growth kinetics of self-induced GaN nanowires *Appl. Phys. Lett.* **100** 153101

[130] Sasaki M and Yoshida S 1996 Scattering of pulsed trimethylgallium beam from GaAs(100), -(110), and -(111)B surfaces *Surf. Sci.* **356** 233–46

[131] Taguchi a. 2005 First-principles investigations of surface reconstructions of an InAs(1 1 1)B surface *J. Cryst. Growth* **278** 468–72

[132] Glas F, Harmand J C and Patriarche G 2007 Why does wurtzite form in nanowires of III-V zinc blende semiconductors? *Phys. Rev. Lett.* **99** 146101

[133] Gil E, Dubrovskii V G, Avit G, André Y, Leroux C, Lekhal K, Grecenkov J, Trassoudaine A, Castelluci D, Monier G, Ramdani R M, Robert-Goumet C, Bideux L, Harmand J C and Glas F 2014 Record pure zincblende phase in GaAs nanowires down to 5 nm in radius *Nano Lett.* **14** 3938–44

[134] Gao Q, Saxena D, Wang F, Fu L, Mokkapati S, Guo Y, Li L, Wong-Leung J, Caroff P, Tan H H and Jagadish C 2014 Selective-Area epitaxy of pure wurtzite InP nanowires: High quantum efficiency and room-temperature lasing *Nano Lett.* **14** 5206–5211

[135] Dubrovskii V G 2014 *Nucleation Theory and Growth of Nanostructures* (Heidelberg,New York, Dordrecht,London: Springer)

[136] Kelrich A, Dubrovskii V G, Calahorra Y, Cohen S and Ritter D 2015 Control of morphology and crystal purity of InP nanowires by variation of phosphine flux during selective area MOMBE *Nanotechnology* **26** 85303

[137] Mattox D M 1989 Particle bombardment effects on thin-film deposition: A review *J. Vac. Sci. Technol. A* **7** 1105–14

[138] Stoyanov S 1974 Nucleation on point defects *J. Cryst. Growth* **24**–**25** 293–7

[139] Yoneyama K and Ogawa K 1996 Scanning Tunneling Microscope Studies on Recovery Processes of Sputter-Induced Surface Defects on Si(111)-7×7 *Jpn. J. Appl. Phys.* **35** 3719–23

[140] Sobanska M, Klosek K, Borysiuk J, Kret S, Tchutchulasvili G, Gieraltowska S and Zytkiewicz Z R 2014 Enhanced catalyst-free nucleation of GaN nanowires on amorphous Al2O3 by plasma-assisted molecular beam epitaxy *J. Appl. Phys.* **115** 43517

[141] Bangert U, Goodhew P J, Jeynes C and Wilson I H 1986 Low-energy (2-5 keV) argon damage in silicon *J. Phys. D. Appl. Phys.* **19** 589–603

[142] Dunn D N, Xu P and Marks L D 1992 Problems with the use of surface reconstructions as indicators of a well-ordered surface *J. Cryst. Growth* **125** 543–7

[143] Tomioka K and Fukui T 2012 *Semiconductor Nanostructures for Optoelectronic Devices* ed G-C Yi (Heidelberg: Springer)

[144] Ohtake A and Mitsuishi K 2011 Polarity controlled InAs{111} films grown on Si(111) *J. Vac. Sci. Technol. B* **29** 31804

[145] Björk M T, Schmid H, Breslin C M, Gignac L and Riel H 2012 InAs nanowire growth on oxide-masked 〈111〉 silicon *J. Cryst. Growth* **344** 31–7

[146] Oshima M, Watanabe Y, Heun S, Sugiyama M and Kiyokura T 1996 Stages of Nanocrystal Growth of Compound Semiconductors on Si Substrates *J. Electron Spectros. Relat. Phenomena* **80** 129–32

[147] Olmstead M A, Bringans R D, Uhrberg R I G and Bachrach R Z 1986 Arsenic overlayer on Si(111): Removal of surface reconstruction *Phys. Rev. B* **34**6041(R)

[148] Koga H 2009 Effect of as preadsorption on InAs nanowire heteroepitaxy on Si(111): A first-principles study *Phys. Rev. B* **80** 245302

[149] Cantoro M, Wang G, Lin H C, Klekachev A V., Richard O, Bender H, Kim T G, Clemente F, Adelmann C, Van Der Veen M H, Brammertz G, Degroote S, Leys M, Caymax M, Heyns M M and De Gendt S 2011 Large-area, catalyst-free heteroepitaxy of InAs nanowires on Si by MOVPE *Phys. Status Solidi Appl. Mater. Sci.* **208** 129–35

[150] Venables J A 1994 Atomic processes in crystal growth *Surf. Sci.* **299–300** 798–817

[151] Ghosh P, Kumar S, Ramalingam G, Kochat V, Radhakrishnan M, Dhar S, Suwas S, Ghosh A, Ravishankar N and Raghavan S 2015 Insights on Defect-Mediated Heterogeneous Nucleation of Graphene on Copper *J. Phys. Chem. C* **119** 2513–22

[152] Consonni V, Trampert A, Geelhaar L and Riechert H 2011 Physical origin of the incubation time of self-induced GaN nanowires *Appl. Phys. Lett.* **99** 33102

[153] Knelangen M, Consonni V, Trampert a and Riechert H 2010 In situ analysis of strain relaxation during catalyst-free nucleation and growth of GaN nanowires. *Nanotechnology* **21** 245705

[154] Mårtensson T, Wagner J B, Hilner E, Mikkelsen A, Thelander C, Stangl J, Ohlsson B J, Gustafsson A, Lundgren E, Samuelson L and Seifert W 2007 Epitaxial growth of indium arsenide nanowires on silicon using nucleation templates formed by self-assembled organic coatings *Adv. Mater.* **19** 1801–6

[155] Consonni V 2013 Self-induced growth of GaN nanowires by molecular beam epitaxy: A critical review of the formation mechanisms *Phys. status solidi - Rapid Res. Lett.* **7** 699–712

[156] Du W, Yang X, Pan H, Wang X, Ji H, Luo S, Ji X, Wang Z and Yang T 2015 Two Different Growth Mechanisms for Au-Free InAsSb Nanowires Growth on Si Substrate *Cryst. Growth Des.* **15** 2413–8

[157] Glas F, Ramdani M R, Patriarche G and Harmand J C 2013 Predictive modeling of self-catalyzed III-V nanowire growth *Phys. Rev. B* **88** 195304

[158] Matteini F, Dubrovskii V G, Rüffer D, Tütüncüoğlu G, Fontana Y and Morral A F I 2015 Tailoring the diameter and density of self-catalyzed GaAs nanowires on silicon *Nanotechnology* **26** 105603

[159] Ramdani M R, Harmand J C, Glas F, Patriarche G and Travers L 2013 Arsenic pathways in self-catalyzed growth of GaAs nanowires *Cryst. Growth Des.* **13** 91–6

[160] Gibson S J and LaPierre R R 2014 Model of patterned self-assisted nanowire growth. *Nanotechnology* **25** 415304

[161] Glas F 2010 Vapor fluxes on the apical droplet during nanowire growth by molecular beam epitaxy *Phys. Status Solidi B* **247** 254–8

[162] Gibson S J, Boulanger J P and LaPierre R R 2013 Opportunities and pitfalls in patterned self-catalyzed GaAs nanowire growth on silicon *Semicond. Sci. Technol.* **28** 105025

[163] Woo R L, Gao L, Goel N, Hudait M K, Wang K L, Kodambaka S and Hicks R F

2009 Kinetic Control of Self-Catalyzed Indium Phosphide Nanowires, Nanocones, and Nanopillars *Nano Lett.* **9** 2207–11

[164] Plissard S, Dick K A, Larrieu G, Godey S, Addad A, Wallart X and Caroff P 2010 Gold-free growth of GaAs nanowires on silicon: arrays and polytypism. *Nanotechnology* **21** 385602

[165] Zhang G, Sasaki S, Tateno K, Gotoh H and Sogawa T 2013 Au-free InAs nanowires grown in In-particle-assisted vapor-liquid-solid mode: Growth, structure, and electrical property *AIP Adv.* **3** 52107

[166] Wagner R S and Ooherty C J 1968 Mechanism of Branching and Kinking during VLS Crystal Growth *J. Electrochem. Soc.* **115** 93

[167] Yan X, Zhang X, Li J, Wu Y and Ren X 2015 Self-catalyzed growth of pure zinc blende 110 InP nanowires *Appl. Phys. Lett.* **107** 23101

[168] Yu S, Miao G, Jin Y, Zhang T, Song H, Jiang H, Li Z, Li D and Sun X 2009 Investigation on growth related aspects of catalyst-free InP nanowires grown by metal organic chemical vapor deposition *J. Alloys Compd.* **479** 832–4

[169] W Du, X Yang, Huayong Pan, Xianghai Ji, Haiming Ji, Shuai Luo, Xingwang Zhang, Zhanguo Wang T Y 2016 Controlled-direction Growth of Planar InAsSb Nanowires on Si Substrates without Foreign Catalyst *Nano Lett.* **16** 877–82

[170] Gao L, Woo R L, Liang B, Pozuelo M, Prikhodko S, Jackson M, Goel N, Hudait M K, Huffaker D L, Goorsky M S, Kodambaka S and Hicks R F 2009 Self-catalyzed epitaxial growth of vertical indium phosphide nanowires on silicon *Nano Lett.* **9** 2223–8

[171] Zannier V, Ercolani D, Gomes U P, David J, Gemmi M, Dubrovskii V G and Sorba L 2016 Catalyst composition tuning: the key for the growth of straight axial nanowire heterostructures with group III interchange *Nano Lett.* acs.nanolett.6b03524

[172] Borgström M T, Immink G, Ketelaars B, Algra R and Bakkers E P A M 2007 Synergetic nanowire growth. *Nat. Nanotechnol.* **2** 541–4

[173] Bauer J, Gottschalch V, Paetzelt H and Wagner G 2008 VLS growth of GaAs/(InGa)As/GaAs axial double-heterostructure nanowires by MOVPE *J. Cryst. Growth* **310** 5106–10

[174] Nebol'sin V A and Shchetinin A A 2003 Role of Surface Energy in the Vapor – Liquid – Solid Growth of Silicon *Inorg. Mater.* **39** 899–903

[175] Dick K A, Bolinsson J, Borg B M and Johansson J 2012 Controlling the abruptness of axial heterojunctions in III-V nanowires: Beyond the reservoir

effect *Nano Lett.* **12** 3200–6

[176] Ghasemi M, Sundman B, Fries S G and Johansson J 2014 The thermodynamic assessment of the Au-In-Ga system *J. Alloys Compd.* **600** 178–85

[177] Yan X, Zhang X, Li J S, Lu X L, Ren X M and Huang Y Q 2013 Growth and characterization of straight InAs/GaAs nanowire heterostructures on Si substrate *Chinese Phys. B* **22** 76102

[178] Ameruddin A S, Caroff P, Tan H H, Jagadish C and Dubrovskii V G 2015 Understanding the growth and composition evolution of gold-seeded ternary InGaAs nanowires. *Nanoscale* **7** 16266–72

[179] Wang J, Plissard S R, Verheijen M A, Feiner L F, Cavalli A and Bakkers E P A M 2013 Reversible switching of InP nanowire growth direction by catalyst engineering *Nano Lett.* **13** 3802–6

[180] Hocevar M, Immink G, Verheijen M, Akopian N, Zwiller V, Kouwenhoven L and Bakkers E 2012 Growth and optical properties of axial hybrid III-V/silicon nanowires. *Nat. Commun.* **3** 1266

[181] Dubrovskii V G, Cirlin G E, Sibirev N V., Jabeen F, Harmand J C and Werner P 2011 New mode of vapor-liquid-solid nanowire growth *Nano Lett.* **11** 1247–53

[182] Jacobsson D, Panciera F, Tersoff J, Reuter M C, Lehmann S, Hofmann S, Dick K A and Ross F M 2016 Interface dynamics and crystal phase switching in GaAs nanowires *Nature* **531** 317–22

[183] Dubrovskii V G 2015 Mono- and polynucleation, atomistic growth, and crystal phase of III-V nanowires under varying group V flow *J. Chem. Phys.* **142** 204702

[184] Jasper J J 1972 The Surface Tension of Pure Liquid Compounds *J. Phys. Chem. Ref. Data* **1** 841–1010

[185] Hilner E, Håkanson U, Fröberg L E, Karlsson M, Kratzer P, Lundgren E, Samuelson L and Mikkelsen A 2008 Direct atomic scale imaging of III-V nanowire surfaces *Nano Lett.* **8** 3978–82

[186] Joyce H J, Wong-Leung J, Gao Q, Hoe Tan H and Jagadish C 2010 Phase perfection in zinc blende and wurtzite III-V nanowires using basic growth parameters *Nano Lett.* **10** 908–15

[187] Rosini M and Magri R 2010 Surface Effects on the Atomic and Electronic Structure of Unpassivated GaAs Nanowires *ACS Nano* **4** 6021–31

[188] Kroemer H 2004 The 6.1 A family (InAs, GaSb, AlSb) and its heterostructures: A selective review *Phys. E Low-Dimensional Syst. Nanostructures* **20** 196–203

[189] Dey A W, Svensson J, Ek M, Lind E, Thelander C and Wernersson L E 2013

Combining axial and radial nanowire heterostructures: Radial Esaki diodes and tunnel field-effect transistors *Nano Lett.* **13** 5919–24

[190] Ganjipour B, Leijnse M, Samuelson L, Xu H Q and Thelander C 2015 Transport studies of electron-hole and spin-orbit interaction in GaSb/InAsSb core-shell nanowire quantum dots *Phys. Rev. B* **91**161301(R)

[191] Abergel D S L 2015 Excitonic condensation in spatially separated one-dimensional systems *Appl. Phys. Lett.* **106** 213103

[192] Shin J, Verma A, Stringfellow G B and Gedridge R W 1994 Trisdimethylaminoantimony: A new Sb source for low temperature epitaxial growth of InSb *J. Cryst. Growth* **143** 15–21

[193] C.A.Wang, S.Salim, K.F.Jensen A C J 1997 Characteristics of GaSb growth using various gallium and antimony precursors *J. Cryst. Growth* **170** 55–60

[194] Gonda S, Asahi H, Yamamoto K, Hidaka K, Sato J, Tashima T and Asami K 1998 Metalorganic molecular beam epitaxy/etching of III-V semiconductors *Appl. Surf. Sci.* **130–132** 377–81

[195] Mirko Rocci, Francesco Rossela, Umesh Prasad Gomes, Valentina Zannier, Francesca Rossi, Daniele Ercolani, Lucia Sorba, Fabio Beltram S R 2016 Tunable Esaki effect in catalyst-free InAs/GaSb core-shell nanowires *Nano Lett.* **submitted**

LIST OF PUBLICATIONS

The thesis include contents from the following papers

[1] **U. P. Gomes**, D. Ercolani, V. Zannier, F. Beltram and L. Sorba, Controlling the diameter distribution and density of InAs nanowires grown by Au-assisted methods, Semiconductor Science and Technology,30, 115012, (2015)

[2] **U. P. Gomes**, D. Ercolani, N. V. Sibirev, M. Gemmi, V. G. Dubrovskii, F. Beltram and L. Sorba, Catalyst-free growth of InAs nanowires on Si (111) by CBE, Nanotechnology, 26, 415604, (2015)

[3] **U. P. Gomes**, D. Ercolani, V. Zannier, J. David, M. Gemmi, F. Beltram and L. Sorba, Nucleation and growth mechanism of self-catalyzed InAs nanowires on silicon, Nanotechnology, 27, 255601, (2016)

[4] V. G. Dubrovskii, N. V. Sibirev,Y. Berdnikov,**U. P. Gomes**, D. Ercolani, V. Zannier and L. Sorba, Length distributions of Au-catalyzed and In-catalyzed InAs nanowires, Nanotechnology, 27, 375602, (2016)

[5] **U. P. Gomes**, D. Ercolani, V. Zannier, S. Battiato, E. Ubyivovk, V. Mikhailovskii, Y. Murata, S. Heun, F. Beltram and L. Sorba, Heterogeneous nucleation of catalyst-free InAs nanowires on silicon substrate, submitted to Nanotechnology

[6] V. Zannier, D. Ercolani, **U. P. Gomes**, J. David, M. Gemmi, V. G. Dubrovskii and L. Sorba Catalyst composition tuning: the key for the growth of straight axial nanowire heterostructures with group III interchange, Nano Letters, 10.1021/acs.nanolett.6b03524, (2016)

[7] M. Rocci, F. Rossella, **U. P. Gomes**, V. Zannier, F. Rossi, D. Ercolani, L. Sorba, F. Beltram, and S. Roddaro, Tunable Esaki effect in InAs/GaSb core-shell nanowires, submitted to Nano Letters